

University of Nottingham
UK | CHINA | MALAYSIA

Analytical derivation and numerical test of novel scaling laws for air-water flows

Thesis submitted to the University of Nottingham for the degree of **Doctor of Philosophy, May 2023.**

Daniele Catucci

4342386

Supervised by

Dr Riccardo Briganti
Dr Valentin Heller

Signature _____

Date _____ / _____ / _____

Acknowledgement

I would like to express my sincere gratitude to my Supervisors, Professor Riccardo Briganti and Valentin Heller, for their guidance, support, and encouragement throughout my PhD studies. Their expertise and dedication have been invaluable in shaping my research and helping me develop as a scholar.

I also extend my thanks to the members of my dissertation committee, Professor David Hargreaves and Professor Sébastien Erpicum, for their insightful feedback, valuable suggestions, and constructive criticism. Their expertise in their respective fields has enriched my work and provided me with a broader perspective on my research.

I would like to acknowledge the assistance of the staff and faculty at University of Nottingham, who have provided me with a supportive and stimulating environment for my research. Their dedication to excellence in education and research has been a constant source of inspiration for me.

I am grateful to my colleagues in the Department of Civil Engineering and Environmental Fluid Mechanics and Geoprocesses Research Group, who have provided me with intellectual and social support throughout my PhD journey. Their diverse backgrounds and perspectives have enriched my learning and challenged me to think creatively and critically.

I would like to express my deepest appreciation to my family and friends for their unwavering love, encouragement, and support. Their belief in me has been a constant source of motivation and inspiration.

Last but not least, I would like to acknowledge the love and support of my girlfriend Marica. She has been a constant source of strength and inspiration throughout my PhD journey, despite the challenges of a long-distance relationship. Her unwavering belief in me and her encouragement, even during the toughest times, have been instrumental in my success. Her love and companionship have sustained me through this journey, and I look forward to the next chapter of our journey together.

Thank you all for your contributions to my PhD journey.

Abstract

Physical modelling at reduced size is one of the oldest and most important design tools in hydraulic engineering. To predict the behaviour of the prototype, a physical model needs to incorporate all involved forces. The Froude scaling laws are being used to model a wide range of water flows at reduced size for almost a century. They are based on the invariance of the Froude number, i.e. the square root of the ratio between the inertial and gravity force between the model and its prototype. However, scale effects are observed due to forces excluded from the Froude number, for example in air-water flows, such as hydraulic jumps or wave breaking, the viscous, surface tension and air compressibility forces are scaled incorrectly at reduced size.

This study introduces novel scaling laws (NSLs) to exclude scale effects in the modelling of air-water flows. This is achieved by deriving the conditions under which the governing equations are self-similar with respect to the geometric scale, i.e. they are scale-invariant. To this end, the one-parameter Lie group of point-scaling transformations are applied to the governing equations for air-water flows. These scaling laws involve relationships for all the flow parameters, fluid properties and initial and boundary conditions. First, the scaling laws are derived under the assumption of air incompressibility, subsequently, this assumption is removed. For the

former, the Reynolds-averaged Navier–Stokes equations, including surface tension effects, are used. For the case in which the compressibility of air is taken into account, the equations of heat transfer and perfect gas are added to the system of governing equations.

The NSLs are validated by numerically simulating different phenomena at different scales, i.e. i) a plunging water jet for incompressible air-water flows, ii) a Taylor bubble where the air is considered compressible and iii) a dam break flow impacting an obstacle for both cases. To this end, the governing equations are computed by two-phase flows solvers based on the volume of fluid method available in OpenFOAM v.1706, namely *interFoam* and *interIsoFoam* for incompressible air-water flows and *compressibleInterIsoFoam* when air is considered compressible. When the NSLs are used, some restrictions are applied by still maintaining self-similarity. For the incompressible air case, the gravitational acceleration is kept invariant between the model and its prototype, while the temperature is kept invariant through the scales for compressible air. Further, it is shown that the precise Froude scaling laws, i.e. when the properties of fluids are strictly scaled, are a particular configuration of the NSLs.

Results for the void fraction, turbulent kinetic energy, velocity, pressure and temperature are shown to be self-similar at different scales for i) to iii), i.e. they collapse in dimensionless form. These results are compared with those obtained using the traditional Froude scaling laws, i.e. when ordinary water and air are used in the model, which, on the other hand, show significant scale effects. Furthermore, the importance of modelling air compressibility is analysed by comparing the results of the dam break flows in which the pressure on the obstacle shows an oscillation when the compressibility of air is taken into account. Finally, the implications of the NSLs for the laboratory experiments are discussed and an easy-to-use MATLAB app to

obtain suitable scaling configurations satisfying self-similarity is presented. The NSLs are shown to be more universal and flexible than the Froude scaling laws. Their key advantage is that fluids of different densities from water (at 293 K) and with increased gravitational acceleration now also qualify as potential candidates for laboratory experiments.

Contents

Abstract **i**

Chapter 1 Introduction **2**

1.1 Motivation 2

1.2 Problem statement 4

1.3 Aim and objectives 5

1.4 Thesis outline 7

Chapter 2 Literature Review **8**

2.1 Introduction 8

2.2 The dynamics of air bubbles in water 9

2.3 State of the art on scaling laws for air-water flows 13

2.4 Scale effects 16

2.4.1 Scale effects in air-water flows 16

2.4.2 Effects of air compressibility and heat transfer 19

2.5 Self-similarity and the modern scaling method 21

2.5.1 Scaling approach based on Lie group of point scaling transformations 23

2.6 Summary 26

Chapter 3 Derivation of the novel scaling laws **28**

3.1 Introduction 28

3.2 Derivation of the NSLs for incompressible air-water flows . . 29

3.2.1 Governing equations 29

3.2.2 Application of Lie group transformations 30

3.3 Derivation of the NSLs for compressible air-water flows . . . 39

3.3.1 Governing equations 39
3.3.2 Application of Lie group transformations 41
3.4 Numerical solvers used 49
3.5 Summary 51
Chapter 4 Testing the NSLs 53
4.1 Introduction 53
4.2 Incompressible air-water flows test cases 54
4.2.1 Dam break flow 54
4.2.2 Plunging water jet 62
4.3 Compressible air-water flows test cases 70
4.3.1 Dam break flow 70
4.3.2 Taylor bubble 76
4.4 Summary 85
Chapter 5 Discussion of results 86
5.1 Introduction 86
5.2 Discussion on the NSLs 86
5.3 Discussion of numerical test cases 87
5.4 Implications for laboratory experiments 93
5.5 Summary 96
Chapter 6 Conclusions and future work 98
6.1 Conclusions 98
6.2 Outlook 101
Appendix A Influence of the numerical scheme on the test of the NSLs 103
Appendix B MATLAB app user guide 106
References 111

List of Symbols

A: area of the surface curvature (m^2)

C: void fraction (-)

c_v: specific heat capacity ($m^2\ K^{-1}\ s^{-2}$)

$C_{\epsilon 1}$, $C_{\epsilon 2}$, C_μ, C_{σ_k} and C_{σ_ϵ}: standard coefficients used in the k-ϵ model (-)

d: bubble diameter (m)

$E_{U_b'}$: relative differences of U_b' (-)

f_σ: surface tension force (N)

F: Froude number (-)

g: gravitational acceleration ($m\ s^{-2}$)

k: turbulence kinetic energy ($m^2\ s^{-2}$)

k': dimensionless turbulence kinetic energy (-)

L_c: characteristic length (m)

M_c: molar density ($mol\ m^{-3}$)

M_m: molar mass ($kg\ mol^{-1}$)

n: number of moles (mol)

p: Reynolds-averaged pressure (Pa)

p'_{rel}: dimensionless relative pressure (-)

$\overline{p'}$: average of the dimensionless pressure inside the Taylor bubble (-)

p_0: initial pressure inside the Taylor bubble (Pa)

R: Reynolds number (-)

R: specific gas constant (m^2 K^{-1} s^{-2})

R_u: ideal gas constant (J mol^{-1} K^{-1})

r_1 and r_2: mean radii of the surface curvature (m)

r_{in}: inlet radius of the water plunging jet (m)

T: temperature (K)

$\overline{T'}$: average of the dimensionless temperature inside the Taylor bubble (-)

T_0: initial temperature inside the Taylor bubble (-)

t: time (s)

t': dimensionless time (-)

U_c:velocity of the Taylor bubble (m s^{-1})

U_c: characteristic velocity (m s^{-1})

U_i: Reynolds-averaged flow velocity components (m s^{-1})

U_i: dimensionless Reynolds-averaged flow velocity components (-)

U_n: inlet velocity of the water plunging jet (m s^{-1})

u_i: fluctuating velocity components (m s^{-1})

$\overline{u_i u_j}$: Reynolds stress term (m^2 s^{-2})

V: air volume (m^3)

V': dimensionless air volume (-)

W: Weber number (-)

x_i: spatial coordinates (m)

x'_i: dimensionless spatial coordinates (-)

$\alpha_{c,v}$: scaling exponent for the specific heat capacity (-)

α_g: scaling exponent for the gravitational acceleration (-)

α_k: scaling exponent for the turbulence kinetic energy (-)

α_{M_m}: scaling exponent for the molar mass (-)

α_n: scaling exponent for the number of mole (-)

α_p: scaling exponent for the pressure (-)

α_R: scaling exponent for the specific gas constant (-)

α_T: scaling exponent for the temperature (-)

α_t: scaling exponent of the time (-)

α_U: scaling exponent for the velocity (-)

α_u: scaling exponent for the velocity fluctuation (-)

α_x: scaling exponent of the length (-)

α_ϵ: scaling exponent for the dissipation of the turbulent kinetic energy (-)

α_κ: scaling exponent for the curvature of the free surface (-)

α_μ: scaling exponent for the dynamic viscosity (-)

α_ν: scaling exponent for the kinematic viscosity (-)

α_{ν_t}: scaling exponent for the eddy viscosity (-)

α_ρ: scaling exponent for the density (-)

α_σ: scaling exponent for the surface tension (-)

β: scaling parameter (-)

δ_{ij}: Kronecker delta (-)

ϵ: rate of dissipation of the turbulent kinetic energy ($\mathrm{m^2\ s^{-3}}$)

γ: phase fraction (-)

κ: curvature of the free surface ($\mathrm{m^{-1}}$)

λ: geometrical scale factor (-)

λ_U: geometrical scale factor for the velocity (-)

μ: dynamic viscosity ($\mathrm{m^2\ s^{-1}}$)

ν: kinematic viscosity ($\mathrm{kg\ m^{-1}\ s^{-1}}$)

ρ: density ($\mathrm{kg\ m^{-3}}$)

ρ': initial density of air inside the Taylor bubble (-)

$\overline{\rho'}$: average of the dimensionless density inside the Taylor bubble (-)

σ: surface tension (N m^{-1})

Subscripts

a: air

c: characteristic

iso: *isoAdvector*

M: model

MULES: Multidimensional Universal Limiter with Explicit Solution

P: prototype

PFs: precise Froude scaling laws

TFs: traditional Froude scaling laws

U': dimensionless velocity (-)

w: water

Abbreviations

CFD: computational fluid dynamics

CFL: Courant–Friedrichs–Lewy

D1: prototype of dam break flow

D8: model at $\lambda = 8$ of dam break flows

D16: model at $\lambda = 16$ of dam break flows

FVM: finite volume method

DC1: prototype of dam break flow for compressible air

DC8: model at $\lambda = 8$ of dam break flows for compressible air

DC16: model at $\lambda = 8$ of dam break flows for compressible air-water flows

HPC: high performance computing

NSLs: novel scaling laws

P1: prototype of the water plunging jet

P8: model at $\lambda = 8$ of the water plunging jet

P16: model at $\lambda = 16$ of the water plunging jet

PFs: precise Froude scaling laws

RANS: Reynolds-averaged Navier–Stokes

RMSE: Root Mean Square Error

RW: right wall

T1: prototype of the Taylor bubble

T8: model at $\lambda = 8$ of the Taylor bubble

T16: model at $\lambda = 16$ of the Taylor bubble

TFs: traditional Froude scaling laws

VOF: volume of fluid

List of Figures

1.1 Saint Anthony Falls on the Mississippi River showing a pronounced hydraulic jump (flow from left to right). 3

2.1 Sketch of entrained air layers at (a) a vertical circular plunging jet and (b) a plunging breaking wave. 12
2.2 Schematic representation of an OWC converter with bidirectional air turbine. 20
2.3 Examples of self-similarity in nature: (a) Romanesco broccoli (Kieffer et al., 1998) and (b) screenshot from Google Earth of the Amazon river network. 21
2.4 Examples of fractals: (a) Sierpiński triangle, (b) snowflake pattern, (c) the Mandelbrot set and (d) zoom of Mandelbrot set (Mandelbrot and Mandelbrot, 1982). 22

4.1 Initial set-up of the dam break flow prototype and a scaled numerical domain to schematically illustrate the NSLs (Catucci et al., 2021). 56
4.2 Snapshots of the incompressible-air dam break flow at the cross-section $x_2' = 0$ and dimensionless time $t' = 2.7$ of the (a) prototype and scaled with (b,c) the NSLs, (d,e) PFs and (f,g) TFs laws (Catucci et al., 2021). 58
4.3 k' time histories in the dam break flow at point RW for (a) domains D1, D8, D16, $\mathrm{D8_{PFs}}$ and $\mathrm{D16_{PFs}}$ and (b) D1, $\mathrm{D8_{TFs}}$ and $\mathrm{D16_{TFs}}$ (after Catucci et al., 2021). 60

4.4 γ time histories in the dam break flow at point RW for (a) domains D1, D8, D16, $D8_{PFs}$ and $D16_{PFs}$ and (b) D1, $D8_{TFs}$ and $D16_{TFs}$ (after Catucci et al., 2021). 61

4.5 p'_{rel} time histories in the dam break flow at point UO for (a) domains D1, D8, D16, $D8_{PFs}$ and $D16_{PFs}$ and (b) D1, $D8_{TFs}$ and $D16_{TFs}$ (after Catucci et al., 2021). 62

4.6 Snapshots of the incompressible-air dam break flow at the cross-section $x'_2 = 0$ and dimensionless time $t' = 5$ of the (a) prototype and scaled with (b,c) the NSLs, (d,e) PFs and (f,g) TFs. 63

4.7 Schematic illustration of the computational domain and mesh of the plunging water jet (Catucci et al., 2021). 64

4.8 Time-averaged γ along the section A-A' for domains (a) P1, (b) P8, (c) $P8_{PFs}$ and (d) $P8_{TFs}$ (Catucci et al., 2021). . . . 67

4.9 Distributions of the void fraction for the plunging jet for domains (a) P1, P8, P16, $P8_{PFs}$ and $P16_{PFs}$ and (b) P1, $P8_{TFs}$ and $P16_{TFs}$ along section A-A' at $\frac{x_1-l_1}{r_{im}} = 1.60$ (Catucci et al., 2021). 68

4.10 Time-averaged U' for the plunging jet for domains (a) P1, P8, P16, $P8_{PFs}$ and $P16_{PFs}$ and (b) P1, $P8_{TFs}$ and $P16_{TFs}$ along section A-A' at $\frac{x_1-l_1}{r_{im}} = 1.60$ (Catucci et al., 2021). . . 68

4.11 Time-averaged k' for the plunging jet for domains (a) P1, P8, P16, $P8_{PFs}$ and $P16_{PFs}$ and (b) P1, $P8_{TFs}$ and $P16_{TFs}$ along section A-A' at $\frac{x_1-l_1}{r_{im}} = 1.60$ (Catucci et al., 2021). . . 69

4.12 Snapshots of the dam break flow at the cross-section $x'_2 = 0$ and dimensionless time $t' = 2.7$ of the (a) prototype and scaled with (b,c) the NSLs and (d,e) TFs. 73

4.13 k' time histories in the dam break flow at point RW for (a) domains CD1, CD8, CD16 and (b) CD1, $CD8_{TFs}$ and $CD16_{TFs}$. 74

4.14 γ time histories in the dam break flow at point RW for (a) domains CD1, CD8 and CD16 and (b) CD1, $CD8_{TFs}$ and $CD16_{TFs}$. 75

4.15 p'_{rel} time histories in the dam break flow at point P2 for (a) domains CD1, CD8 and CD16 and (b) CD1, $CD8_{TFs}$ and $CD16_{TFs}$. 75

4.16 Snapshots of the dam break flow at the cross-section $x'_2 = 0$ and dimensionless time $t' = 5$ of the (a) prototype and scaled with (b,c) the NSLs and (d,e) the TFs. 76

4.17 Schematic illustration of the computational domain at prototype scale: (a) the longitudinal section of the domain, (b) the Taylor bubble region and (c) a cross-section of the mesh (Catucci et al., 2022b) 78

4.18 Snapshot of the Taylor bubble at the cross-section $x'_2 = 0$ and dimensionless time $t' = 2.90$ of the (a) prototype, (b) T16 and (c) $T16_{TFs}$ (Catucci et al., 2022b). 80

4.19 Snapshot of the Taylor bubble at the cross-section $x'_2 = 0$ and dimensionless time $t' = 14.54$ of the (a) prototype, (b) T16 and (c) $T16_{TFs}$ (Catucci et al., 2022b). 81

4.20 Time history of the bubble nose location on the x'_3 coordinate for the prototype and all the scaled domains. 81

4.21 Time histories of the averages of the (a) $\overline{\rho'}$, (b) $\overline{T'}$ and (c) $\overline{p'}$ inside each modelled Taylor bubble and (d) V' for T1, T4, T8 and T16 (Catucci et al., 2022b). 83

4.22 Time histories of the averages of the (a) dimensionless density $\overline{\rho'}$, (b) dimensionless temperature $\overline{T'}$ and (c) dimensionless pressure $\overline{p'}$ inside the bubbles and (d) the dimensionless volume V' for T1, $T4_{TFs}$, $T8_{TFs}$ and $T16_{TFs}$ (Catucci et al., 2022b). 84

4.23 Time history of the void fraction lost in the wake of the bubble for the prototype and the scaled domains. 84

5.1 p'_{rel} time histories in the dam break flow at point UO for domains D1 and CD1. 92
5.2 p'_{rel} time histories in the dam break flow at point DO for domains D1 and CD1. 92
5.3 GUI of the MATLAB app. The inputs to obtain the scaling configuration based on the properties of the water at 338.15 K are highlighted. 95
5.4 GUI of the MATLAB app. The scaling exponents of the configuration based on the properties of water at 338.15 K are highlighted. 96

A.1 Snapshots of the dam break flow simulated by using *interIsoFoam* at the cross-section $x'_2 = 0$ and dimensionless time $t' = 2.7$ of the (a) domain $\mathrm{D1_{iso}}$ and scaled with the NSLs at the domains (b) $\mathrm{D8_{iso}}$ and (c) $\mathrm{D16_{iso}}$, respectively (Catucci et al., 2022a) 105
A.2 Time histories of (a) k' and (b) γ in the dam break flow at point RW for domains $\mathrm{D1_{iso}}$, $\mathrm{D8_{iso}}$ and $\mathrm{D16_{iso}}$ (Catucci et al., 2022a). 105

B.1 Home window of the MATLAB app. 106
B.2 Window for the scaling laws for incompressible air with the input to obtain the scaling configuration written in terms of α_x, $\alpha_g = 0$ and α_ρ. 107
B.3 GUI for the NSLs for incompressible air with the resulting scaling configuration written in terms of α_x, $\alpha_g = 0$ and α_ρ. . 108

B.4 GUI for the NSLs for compressible air with the input to obtain the scaling configuration written in terms of α_x, $\alpha_T = \alpha_{Mm} = \alpha_R = 0$ and $\alpha_n = 3\alpha_x$ ($\alpha_\rho = 0$). 109
B.5 Window for the scaling laws for compressible air with the resulting scaling configuration written in terms of α_x, $\alpha_T = \alpha_{Mm} = \alpha_R = 0$ and $\alpha_n = 3\alpha_x$ ($\alpha_\rho = 0$). 110
B.6 Error message due to the selection of two or more conditions that cannot both be satisfied simultaneously. 110

List of Tables

2.1 Scaling laws based on the similarity of F, R and W 15

3.1 NSLs and PFs for the parameters of the RANS equations and the k-ϵ turbulence model obtained by applying the Lie group transformations. 38
3.2 NSLs for the parameters of the governing equations for air-water flows including compressibility and heat transfer. . . . 46

4.1 Summary of the simulations carried out to validate NSLs. . . 54
4.2 Numerical schemes for the dam break simulations. 56
4.3 Scaling parameters and exponents used to scale the dam break flow prototype values to the corresponding values in the domains D8 and D16 using the NSLs (Catucci et al., 2021). 57
4.4 Parameters for the dam break flow in the prototype and the scaled domains. 58

4.5 $\mathrm{RMSE}_{U'}$ for the dam break flow for the domains D1 and D8, D16, $\mathrm{D8}_{\mathrm{PFs}}$, $\mathrm{D16}_{\mathrm{PFs}}$, $\mathrm{D8}_{\mathrm{TFs}}$ and $\mathrm{D16}_{\mathrm{TFs}}$, for the snapshots in Figure 4.2 (Catucci et al., 2021). 59
4.6 Numerical schemes for the plunging jet case. 65
4.7 Scaling parameters and used exponents to scale the plunging jet prototype values to the corresponding values in the domains P8 and P16 (Catucci et al., 2021). 66
4.8 Numerical schemes for the dam break simulations. 71
4.9 Scaling parameters and exponents used to scale the dam break flow prototype values to the corresponding values in the domains CD8 and CD16 using the NSLs. 72
4.10 Parameters for the dam break flow in the prototype and the scaled domains. 72
4.11 $\mathrm{RMSE}_{U'}$ computed for domains CD8, CD16, $\mathrm{CD8}_{\mathrm{TFs}}$ and $\mathrm{CD16}_{\mathrm{TFs}}$ with respect to CD1, for the snapshots in Figure 4.12. 73
4.12 Parameters for the Taylor bubble in the prototype and the scaled domains (Catucci et al., 2022b). 79
4.13 U_b' for the prototype and all scaled domains (Catucci et al., 2022b). 82

Chapter 1

Introduction

1.1 Motivation

One of the first scientific accounts of air entrainment into water (herein called air-water flows) was made by Leonardo da Vinci (AD 1452-1519, Chanson, 2004a). He described several flow configurations and commented on air entrapped in waterfalls, mountain torrents and in breaking waves. These are natural phenomena which often interact with human structures such as coastal and river defences. Moreover, hydraulic jumps (Figure 1.1) are used to dissipate energy in turbulent flows downstream of dams, weirs and spillways to prevent or reduce scour further downstream of these structures (Harada and Li, 2018). Air entrainment is also responsible for the bulk of mass transfer that occurs at the free surface of oceans and rivers providing the transport of oxygen and carbon dioxide as well as being involved in important processes related to the global climate evolution (Liu and Duncan, 2003). In addition, air-water flows are important in naval engineering because bubble entrainment into water provides a source of acoustic noise and surfactant scavenging in the boundaries of ships and

thus modifying the hydrodynamic performance (Kiger and Duncan, 2012).



Figure 1.1: Saint Anthony Falls on the Mississippi River showing a pronounced hydraulic jump (flow from left to right).

The amount of air entrained into water is determined by turbulence next to the air-water interface, the gravity acceleration and by the properties of fluids, i.e. density, viscosity and surface tension. Further, air-water flows involve also compressibility effects because the air density is about 830 times smaller than of water at 20 °C (293.15 K), meaning that an air bubble can be compressed by the surrounded water. This can play a central role in rapidly evolving flows, e.g. violent breaking wave impact. Indeed, studies on the temporal and spatial variations of the breaking wave induced pressure and force on a wall led to the conclusion that the highest pressure occurs when a small pocket of air is trapped against the wall (Bredmose et al., 2015). The compressibility of air needs to be taken into account to correctly estimate impact forces (Müller, 2019; Peregrine and Thais, 1996). A further example is air entrainment in pressure conduits in hydropower plants (Vereide et al., 2015; Zhou et al., 2013). The study of air-water flows is often conducted in the laboratory by using physical models to understand the phenomenon at reduced size.

1.2 Problem statement

Physical modelling at reduced size is one of the oldest and most important design tools in hydraulic engineering. A basic requirement of a physical model is to correctly reproduce in the laboratory the behaviour of the phenomena in nature, usually referred to as a prototype. For the processes of engineering interest involving free surface flows, the Froude scaling laws (or Froude similarity) have been used since they were introduced by Moritz Weber in 1930 (Hager and Castro-Orgaz, 2017). They ensure that the square root of the ratio between the inertial and gravity force, namely the Froude number F, is the same in the model and in the prototype. Other forces ratios, such as the Reynolds number R (inertial force to viscous force) and the Weber number W (inertial force to surface tension force), are represented not preserved if the fluid properties are the same in the prototype and in its model (Ali and Dey, 2017; Heller, 2011; Hughes, 1993). Froude scaling laws are particularly useful for laminar ($\mathsf{R} \rightarrow 0$) and fully turbulent free surface flows ($\mathsf{R} \rightarrow \infty$) to investigate R independent fluid parameters (Frisch, 1995; Heller, 2017).

However, the Froude scaling laws are also used for air-water flows. For these, density, viscosity and surface tension between water and air play a central role such that F, R and W are all important (Biń, 1993; Kiger and Duncan, 2012). Indeed, most studies suggest that the amount of air entrainment in air-water flows modelled with the Froude scaling laws, without scaled fluid properties, is underestimated because the effects of viscosity and surface tension are over-represented in the model (Heller et al., 2008; Stagonas et al., 2011).

Furthermore, the Froude scaling laws do not account for the effects of

air compressibility and heat transfer. Hence, additional scale effects are potentially introduced because of the effects of temperature and because the thermophysical properties of air are neglected (Bredmose et al., 2015; Lin et al., 2021).

Even though both the surface tension and compressibility effects can be crucial in air-water flows, they are incorrectly modelled in physical models. Hence, the Froude scaling laws are not suitable for air-water flows because gravity, viscous, surface tension and air compressibility are scaled incorrectly.

1.3 Aim and objectives

This work aims at deriving flexible and universal scaling laws for air-water flows that can be used to improve laboratory modelling of this type of flows. An analytical approach to derive novel scaling laws (NSLs) is based on the self-similarity of the governing equations with respect to the geometrical scale, in contrast to the traditional scaling based on dimensionless parameters. A self-similar process behaves the same way at different scales, such that scale effects are avoided (Polyanin and Manzhirov, 2008). This implies that the dimensionless results are the same at different scales.

This aim will be achieved through the following objectives:

- The first objective is the derivation of the scaling laws by applying the Lie group scaling method to the governing equations of air-water flows. These consist of the Reynolds-averaged Navier-Stokes (RANS) equations where the surface tension is added as a source term. Thereafter, air is considered compressible and the Lie group scaling method

is therefore applied to the RANS, the heat transfer and the perfect gas equations for air.

- The second objective is the testing of the scaling laws by using computational fluid dynamics (CFD) to simulate phenomena involving air entrainment and/or compressibility of air. Prototypes of three air-water flows, i.e. a dam break flow, plunging water jet and Taylor bubble, will be scaled by using the derived NSLs and the dimensionless results will be compared with the prototypes. The first two processes are also simulated with the commonly applied Froude scaling laws using ordinary water and air in the model, as is common in laboratory experiments (herein called traditional Froude scaling laws, TFs), and the Froude scaling laws in which the properties of the fluids are strictly scaled (herein called precise Froude scaling laws, PFs).

This new approach involves the derivation of scaling conditions by applying the one-parameter Lie-group of point scaling transformations (Lie, 1880, hereafter referred to as Lie group transformations) to the governing equations. The Lie group transformations were originally used to reduce the number of independent variables of an initial boundary value problem by transforming it into a new space where the solution of the problem remains the same as the original one. Subsequently, they were applied to derive the conditions under which various hydrological processes are self-similar through the change in size. This method to derive scaling laws (hereafter called the Lie group scaling method) has the advantage of resulting in a complete set of conditions for all the variables in the governing equations that must be satisfied to achieve self-similarity.

Given these objectives, air–water flows are herein simulated by using three solvers available in the OpenFOAM v.1706 CFD package, i.e. *interFoam*

and *interIsoFoam* for incompressible air-water flows, and *compressibleinterIsoFoam* when air is considered compressible. They are two-phase solvers based on the volume of fluid (VOF) method.

1.4 Thesis outline

In Chapter 2, the state of the art of scaling of air-water flows is presented and the Lie group scaling method is introduced. In Chapter 3 the Lie group scaling method is applied to the governing equations and the NSLs are derived, first by considering both fluids as incompressible and, subsequently, by accounting for the compressibility of air. Chapter 4 introduces the numerical model and the CFD case studies. The results of the test of the NSLs are presented. The findings of this research are discussed in Chapter 5 where a MATLAB app to find different configurations of the NSLs is presented. The conclusions and recommendations for future work are given in Chapter 6. Finally, Appendix A includes the influence of the numerical scheme on the test and Appendix B a user guide of the MATLAB app.

Chapter 2

Literature Review

2.1 Introduction

In laboratory experiments of hydraulic phenomena, the dimensionless numbers should be the same to avoid scale effects. Since the laboratory modelling introduces some restrictions, it is difficult to keep all the dimensionless numbers invariant between the model and the prototype (Ettema, 2000). For example, the Froude scaling laws ensure that the square root of the ratio between the inertial and gravity forces, namely the Froude number F, is the same in the model and in nature, i.e. in the prototype. Other force ratios, such as the Reynolds number R (inertial to viscous force) and the Weber number W (inertial to surface tension force), are not invariant if the fluid properties are the same in the prototype and its model. Hence, the laboratory models involve some degree of scale effects, i.e. a difference in the dimensionless results between the model and its prototype due to the inability to keep all the force ratios invariant. However, the Froude scaling laws are also used for flows involving air entrainment. For these, density, viscosity and surface tension between water and air play a

central role such that F, R and W are all important (Kiger and Duncan, 2012). Furthermore, the Froude scaling laws do not account for the effects of air compressibility and heat transfer. Hence, additional scale effects are potentially introduced because of the effects of temperature and because thermophysical properties of air are neglected (Bredmose et al., 2015; Lin et al., 2021).

An analytical approach to derive novel scaling laws (NSLs) can be based upon the self-similarity of the governing equations. A self-similar object is identical to a part of itself. As such, the scaling of an object that follows suitable laws results in a scaled copy of the object itself. This allows deriving scaling laws based on the governing equations and their boundary conditions without any initial assumptions.

In this chapter, after a brief introduction to the dynamics of air-water flows, the most common scaling laws in hydraulics are discussed. Then, the literature about scale effects in air-water flows is reviewed, distinguishing between the compressible and incompressible case. In the last part of this chapter, the self-similarity is introduced and the modern method to derive scaling laws is presented, highlighting its advantages with respect to the traditional method.

2.2 The dynamics of air bubbles in water

In hydraulics, air entrainment is defined as the entrapment of air bubbles and pockets occurring within turbulent flows (Figure 2.1). In most natural cases, air entrainment takes place in a discontinuity of the free surface (Bińi, 1993; Chanson, 2004b). For example, in an open channel, the increase of the velocity leads to an increase in turbulence and the free surface exhibits

undulations with large underlying eddies. Air entrainment starts when turbulent eddies break up the water surface because the turbulent shear stress becomes larger than the capillary force due to the surface tension. This concept is mathematically expressed by

$$|\rho u_{\mathrm{i}} u_{\mathrm{j}}| = \sigma \frac{\pi(r_1 + r_2)}{A}, \tag{2.1}$$

where i is the free index, j the dummy index, following Einstein's notation, u_{i} and u_{j} are the fluctuating velocity components resulting from a Reynolds average, r_1 and r_2 the main radii of the surface curvature due to the turbulent eddies, A is the area of the deformed free surface, ρ the density of and σ the surface tension between water and air. Once entrapped, air bubbles are transported by turbulent flows creating a region of a high density of bubbles, often called *white water*. This region is characterised by a strong momentum mixing and the bubbles break. Experiments conducted in water plunging jets and hydraulic jumps show that the bubbles can have a size smaller than the Kolmogorov micro-scale and larger than the turbulent macro-scale (Chanson et al., 2004; Wang and Chanson, 2015). Hence, the bubble breakup occurs when the eddy size is similar to the bubble size. Indeed the small eddies do not have enough energy to break the bubbles and the larger eddies advect them (Biń, 1993; Duncan et al., 1994). The bubble breakup limit condition is expressed as

$$|\rho u_{\mathrm{i}} u_{\mathrm{j}}| = \frac{\sigma}{\pi d}, \tag{2.2}$$

where d is the diameter of the bubble, which is supposed to be spherical. This approach can be extended to non-spherical bubbles occurring for flows characterised by anisotropic turbulence (Chanson, 2004b).

Hence, the governing parameters of air-water flows are the velocity of the

flow, the gravitational acceleration, the length of the interaction line at which air is entrapped, the properties of water and air and the surface tension (Kiger and Duncan, 2012; Kobus and Koschitzky, 1991). In addition, there are also compressibility effects. The difference in density between water and air and the increase of water pressure compress the bubbles. In many cases, the compressibility effects of air are negligible. For example, in hydraulic jumps part of the air is entrapped in the surface of the flow where the water pressure is low. However, for fast evolving flows, air compressibility is not negligible (Müller, 2019). For example, in coastal vertical breakwaters, pockets of air are entrapped between the overturning breaker and structure and they are compressed by the flow. It has been shown that the presence of air pockets increases the pressure peak and it can result in the structure failure (Bagnold, 1939; Bredmose et al., 2015; Hattori et al., 1994; Peregrine and Thais, 1996).

Dimensional analysis for a plunging water jet

In this section, Buckingham's Π theorem is applied to a vertical circular plunging water jet on quiescent water characterised by significant air entrainment. This flow has been widely studied as a benchmark for air-water flows (Biń, 1993; Chanson et al., 2002; Kiger and Duncan, 2012). For example, in plunging breakers, the entrainment of air bubbles is caused by the crest of the wave forming a water jet that impacts the free surface of the water in front of the wave (Figure 2.1).

Considering air bubbles entrainment in plunging jets, the governing parameters are the characteristic length L_c that can be the nozzle radius r_{in} or the chute height, the characteristic velocity U_c, e.g., the inlet velocity of the jet U_{in}, the density of water ρ_w and air ρ_a, the kinematic viscosity of water

ν_w and air ν_a, the surface tension σ between water and air and the gravitational acceleration g (Biń, 1993; Kiger and Duncan, 2012). The amount of air in water is expressed by the void fraction C that is the percentage of the air volume with respect to the total volume and it is a dimensionless parameter. Both fluids are considered incompressible. Therefore, compressibility and heat transfer effects are neglected, following most studies (Biń, 1993; Chanson et al., 2004; Müller, 2019; Kiger and Duncan, 2012). C is related to the other governing parameters by a physical function.

$$F(C, r_{in}, U_{in}, g, \rho_w, \nu_w, \rho_a, \rho_a, \sigma) = 0. \tag{2.3}$$

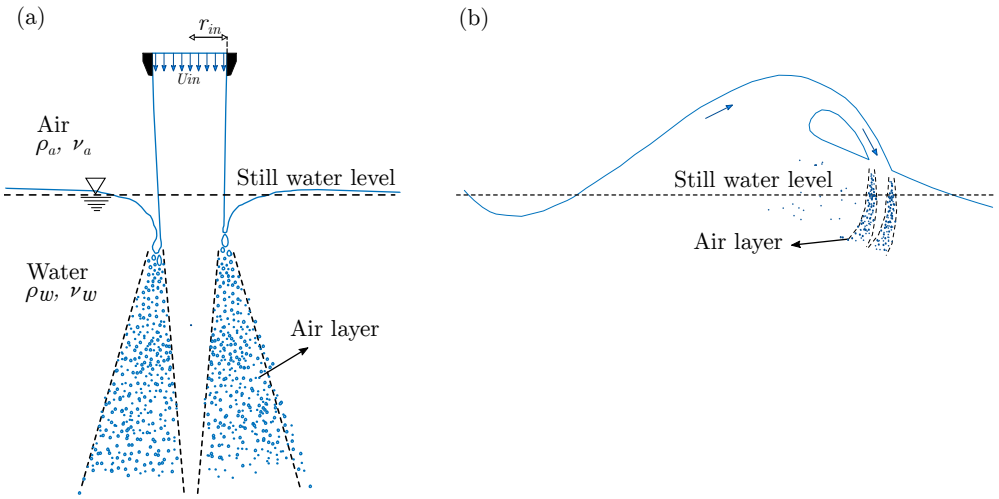


Figure 2.1: Sketch of entrained air layers at (a) a vertical circular plunging jet and (b) a plunging breaking wave.

Hence, a plunging water jet is described by 9 governing parameters in which 3 are independent, e.g. r_{in}, U_{in} and ρ_w. Buckingham's Π theorem implies that the quantities can be grouped into 6 dimensionless parameters:

$$\Phi\left(C, \mathsf{F}, \mathsf{R}, \mathsf{W}, \frac{\rho_a}{\rho_w}, \frac{\nu_a}{\nu_w}\right) = 0, \tag{2.4}$$

where $\mathsf{F} = \frac{U_c}{\sqrt{L_c g}}$ is the Froude number, $\mathsf{R} = \frac{L_c U_c}{\nu_w}$ the Reynolds number and $\mathsf{W} = \frac{\rho_w L_c U_c^2}{\sigma}$ is the Weber number. C is already dimensionless and remains unchanged when the Buckingham's Π theorem is applied. Note that a different combination of dimensionless parameters can be used (Kiger and Duncan, 2012). Alternatively, the density and viscosity ratios between air and water can be replaced by R and W calculated with ν_a and ρ_a. Hence, C is mainly described by F, R and W (Biń, 1993; Khan and Hoque, 2010; Pfister and Chanson, 2014).

2.3 State of the art on scaling laws for air-water flows

Scaling laws are relationships between geometrical and physical parameters in the prototype and in laboratory models, hence, they are used to design models and test them in the laboratory. In this section, the traditional method to derive scaling laws in fluid mechanics is analysed. This method is based on the similarity between the model and its prototype. In physics, two phenomena are similar if they involve three levels of similarity: geometric, kinematic and dynamic similarity (Barenblatt, 1996; Heller, 2011; Hughes, 1993; Kline, 1965; Zohuri, 2015).

Geometric similarity requires similarity in shape. Hence, the geometry of a model is designed by using a uniform scale factor $\lambda = (L_c)_P/(L_c)_M$, where $(L_c)_P$ is the characteristic length in the prototype (subscript P) and $(L_c)_M$ is the corresponding one in the model (subscript M). All lengths, areas and volumes should be scaled by λ, λ^2 and λ^3, respectively. Kinematic similarity requires geometric similarity and motion similarity, meaning invariant ratios of time, velocity and acceleration in the model and its prototype.

Dynamic similarity requires kinematic similarity and the invariance of ratios between various types of forces, such as F, R and W (Section 2.2). This means that the dynamic similarity in air-water flows is reached when F, R and W are the same between the model and its prototype. However, the correct similarity of only two dimensionless parameters, such as F and R, is already challenging (Heller, 2011, 2017; Hughes, 1993; Pfister and Chanson, 2014). Indeed, laboratory modelling introduces some constrains in the fluid properties or in the boundary conditions such that the dimensionless numbers are not all invariant. Hence, one strategy is to select the most relevant force ratio and neglect the effects of the others. Traditional scaling laws are thus derived by keeping invariant the force ratio individually.

Froude scaling laws (or Froude similarity) are based on the equivalence of F between the prototype and its model and they are used when g is dominant. Hence, g is kept invariant in models ($g_M = g_P$), resulting in specific scaling properties (Table 2.1). For example, the scaling factor for velocities is $\lambda_U = \lambda^{1/2}$, meaning that velocities need to be reduced in the model. Froude scaling laws are particularly useful where friction effects are negligible and also for fully turbulent flows ($\mathsf{R} \to \infty$) to investigate R invariant fluid parameters (Heller, 2017).

However, in some phenomena involving air flows, laminar boundary layer problems, the viscous forces are significant and scaling laws based on R are more suitable (Heller, 2011). Reynolds scaling laws are based on the equivalence of R between the model and its prototype. This similarity is used when the viscous effects are not negligible. If ν is kept invariant between the model and its prototype ($\nu_M = \nu_P$), $\lambda_U = \lambda^{-1}$, meaning that the velocity in the model needs to increase, creating a practical issue in the application of these scaling laws (Chanson and Felder, 2007; Heller, 2011; Hughes, 1993).

When σ is significant, the seeking similarity of W is more suitable. The Weber scaling laws are useful in modelling and analysing the interface between two fluids and thus when the surface tension effects are not negligible. The Weber scaling laws are based on the equivalence of W between the model and its prototype ($\sigma_M = \sigma_P$), leading to $\lambda_U = \lambda^{-1/2}$. Although the surface tension effects are negligible in most of engineering applications, they play a central role in all the phenomena characterised by a high amount of air entrainment into water (Hubbard et al., 1987; Kiger and Duncan, 2012; Pfister and Chanson, 2014).

Table 2.1: Scaling laws based on the similarity of F, R and W

Parameters	Froude scaling laws	Reynolds scaling laws	Weber scaling laws
Geometric similarity			
Length (m)	λ	λ	λ
Area (m^2)	λ^2	λ^2	λ^2
Volume (m^3)	λ^3	λ^3	λ^3
Kinematic similarity			
Time (s)	$\lambda^{1/2}$	λ^2	$\lambda^{3/2}$
Velocity (m s^{-1})	$\lambda^{1/2}$	λ^{-1}	$\lambda^{-1/2}$
Acceleration (m s^{-2})	1	λ^{-3}	λ^{-2}
Dynamic similarity			
Mass (kg)	λ^3	λ^3	λ^3
Force (m s^{-2} kg)	λ^3	1	λ
Pressure (m^{-1} s^{-2} kg)	λ	λ^{-2}	λ^{-1}

Hence, scaling laws based on the similarity of one force ratio are based on initial assumptions. This is a disadvantage, because it results in specific scaling laws that take into account some effects and neglect others. Thus, they do not give a complete picture of the conditions that must be satisfied to avoid scale effects between a model and its prototype.

Since changing g in laboratory models is challenging, the Froude scaling laws are most common in hydrodynamics, resulting in some accurate pre-

dictions (Novak et al., 2010; Hughes, 1993). However, in most cases, ordinary water and air are used in laboratory and thus scale effects arise because R and W are represented incorrectly.

2.4 Scale effects

Scale effects are due to the inability to keep all the dimensionless parameters invariant between a scaled model and its prototype. Even if the magnitude of scale effects depends on the investigated phenomenon, all hydraulic model tests involve some degree of scale effects when $\lambda \neq 1$. Further, the model force ratios deviate more from the prototype with increasing λ, the larger are scale effects. Nevertheless, the importance of each force ratio depends on the specific phenomenon. For example, in air-water flows, the surface tension force plays a central role in determining the amount of air entrainment. On the other hand, the velocity field is less affected by scale effects if the surface tension is not correctly scaled in the model (Ettema and Muste, 2004; Heller, 2011; Pfister and Chanson, 2014; Ettema, 2000).

2.4.1 Scale effects in air-water flows

Scale effects in air entrainment are reported extensively in plunging water jets (Biń, 1993; Chanson et al., 2004; Cummings and Chanson, 1997). The time-averaged distribution of the void fraction is usually measured in a local section at at a certain distance from the jet impact point by using a conductivity probe. This results in a characteristic Gaussian air distribution across the air layer (Chanson et al., 2004). By using Froude scaling laws with ordinary water and air in the model (TFs), the void fraction distribution decreases with increasing λ because viscous and surface

tension effects become more dominant at small scales (Chanson, 2009b; Heller et al., 2008; Pfister and Chanson, 2014). This phenomenon can be explained by using the mathematical model presented in Section 2.2. Since ordinary water and air are predominantly used in scaled models, ν and σ remain invariant and they are over-represented in the model with respect to the prototype. Hence, the right terms in Eqs. (2.1) and (2.2) become more dominant with increasing λ and the break up of the free surface and bubbles are less severe.

In hydraulic jumps, air entrainment occurs at the toe of the jump, developing an air entrainment layer similar to a water plunging jet. Further, air is also entrapped at the free surface between air and water (Chanson and Chachereau, 2013; Chanson, 2009a; Wang and Chanson, 2015). Hence, the void fraction distribution shows a second peak near the free surface of a hydraulic jump. When R is an order of magnitude smaller, the maximum bubble count rate is reduced by almost an order of magnitude. The differences are limited in the second peak of the bubble count rate mostly because of the transportation of the bubbles upward to the free surface (Chanson and Chachereau, 2013; Wang and Chanson, 2016).

TFs are also used to design laboratory models of chute spillway flows (Hager et al., 2020; Ruff and Frizell, 1994). They consist of sloped open channel flows which could be stepped or smooth. The results of the scale series designed by using TFs have shown a smaller number of bubbles by about 30–60% and bigger dimensionless bubble sizes in the models (Pfister and Hager, 2010). In the same way, lower turbulence levels and larger turbulent dimensionless length and time scales have been observed at lower R and W and the same F. This has a direct consequence on the design of stepped spillways. Indeed, an underestimation of the amount of air and turbulence levels implies an underestimation of the energy dissipation on the prototype

(Felder and Chanson, 2009; Pfister and Hager, 2010).

In most experiments, air-entrainment parameters are measured with an intrusive probe having the same size in all experiments, i.e. the probe sensor size is not scaled down in the models. This introduces measurement effects next to scale effects (Carosi and Chanson, 2006). The characteristic parameters for the design of the tip conductivity probes are the air bubble sizes and their velocity which both change with λ by using TFs. Measurement of the same air entrainment properties has shown that a smaller probe size detects larger bubble count rates and a broader range of bubble sizes (Hohermuth et al., 2021; Leandro et al., 2014; Nina et al., 2022). For example, Carosi and Chanson (2006) shows that the bubble size in a stepped spillway with a probe size of 0.35 mm of diameter is from 18 to 50 % larger than the chord lengths measured in the same conditions but with with a sensor of 0.25 mm.

Nevertheless, the use of non-intrusive measurement techniques shows clearly that models based on the TFs underestimate the amount of air entrainment. Images of air-water flows models based on the TFs visually demonstrate that the amount of air bubbles decreases with λ (Heller et al., 2008; Wang and Chanson, 2016).

There are mainly two approaches to deal with scale effects in laboratory tests design, namely (i) limit the model scale to a maximum of $\lambda = 10$ and (ii) limit the variation of W and R between the model and prototype (Hughes, 1993; Pfister and Chanson, 2014). In any case, all laboratory models are affected by a certain degree of scale effects and a compromise between the limitation of scale effects and a low-cost laboratory model should be found.

2.4.2 Effects of air compressibility and heat transfer

Besides the fact that the TFs underestimate the air entrainment, they do not account for the effects of air compressibility and heat transfer. Hence, additional scale effects are potentially introduced because of the effects of temperature and because the thermophysical properties of air are neglected. When a wave impact coastal structures, pockets of air can be entrapped between the overturning breaker and the structure. Bagnold (1939) was one of the first to conduct laboratory experiments into breaking waves impacts on a vertical wall and found that the highest pressures occur when a pocket of air is entrapped against the wall. He proposed a theoretical model based on the one-dimensional flow of a "piston" of water compressing an air cushion the compression of which is adiabatic. Subsequently, Mitsuyasu (1967) expanded the theory by adding the case with air leakage and demonstrated the reduction of the impact pressure. Several experimental, analytical and numerical studies of the shock pressure due to breaking waves were conducted, highlighting the role of compressibility of air in the pressure peak (Bredmose et al., 2015; Peregrine and Thais, 1996; Lugni et al., 2010; Hattori et al., 1994).

The design of coastal structures is often based on a small-scale model designed by using TFs. In those scaling laws, the pressure scales with λ. Since the pressure peak is associated with the quantities of air entrainment, the TFs lead to scale effects because air is underestimated and its compressibility is not taken into account (Bredmose et al., 2015). The use of TFs in a scale series of violent breaking wave impact characterised by a high-aeration shows that the dimensionless pressure peak is about double at $\lambda = 16$ (Bredmose et al., 2015). Nevertheless, the TFs are still used to design laboratory models, although it does not account for the compress-

ibility effects (Cuomo et al., 2010; Bullock et al., 2001).

Air compressibility effects play also an fundamental role in oscillating water column (OWC) wave energy converters. In such schemes, there is a fixed or floating hollow structure, open to the sea at its submerged part, that traps air in a chamber above the inner free surface (Figure 2.2). Wave action alternately compresses and decompresses the trapped air which is forced to flow through a turbine coupled to an electrical generator (Falcão and Henriques, 2014). The air compression/decompression process in the chamber involves changes in air density that should not be neglected. When a model is tested in a laboratory the compressibility of air and its thermophysical properties should be taken into account (Falcão and Henriques, 2019). To reproduce correctly this effects in the scaled model, the ratio between the air chamber volume of model and prototype has to be equal to λ^2 instead of λ^3 (Falcão and Henriques, 2019). This strategy reduces scale effects related to air-water interaction inside the chamber but the forces at the device are not scaled correctly (Viviano et al., 2018).

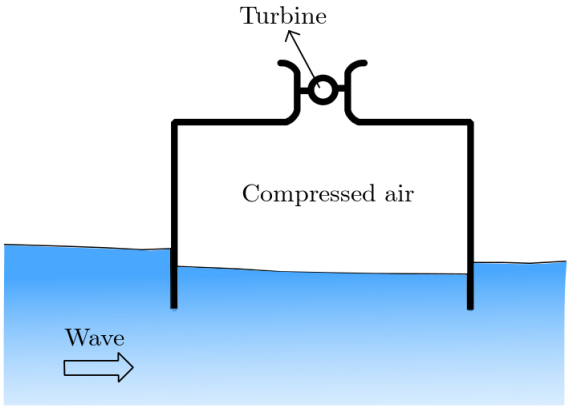


Figure 2.2: Schematic representation of an OWC converter with bidirectional air turbine.

The compressibility of air plays a central role in pipe systems, especially in hydropower plants. Sometimes, air pockets can be entrapped at high

points of the water system in the rest phase. Once restarted, the entrapped air pockets cause an abnormal pressure surge, which can break the pipe (Vereide et al., 2015; Zhou et al., 2013).

Even though air compressibility is crucial in many phenomena, in most scaled models, it is neglected. Further, there is no set of scaling laws that are suitable for compressible air-water flows. Hence, TFs are not suitable for air-water flows because viscous, surface tension and air compressibility effects are scaled incorrectly.

2.5 Self-similarity and the modern scaling method

An analytical approach to derive scaling laws is based on self-similarity. The most general definition of self-similarity is an object that is identical to a part of itself. As such, the scaling of a self-similar object results in a self-similar copy of the object itself (Barenblatt, 2003; Henriksen, 2015; Zohuri, 2015).

(a) (b)

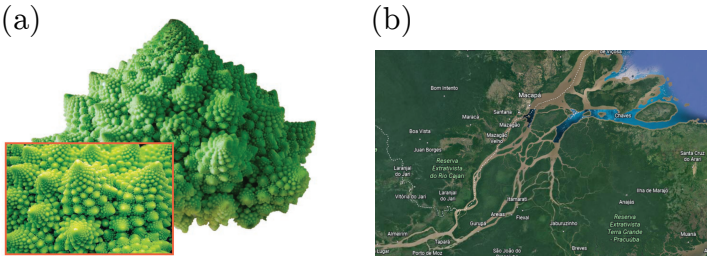


Figure 2.3: Examples of self-similarity in nature: (a) Romanesco broccoli (Kieffer et al., 1998) and (b) screenshot from Google Earth of the Amazon river network.

Self-similarity, fractals (Figure 2.4), power laws and scale-invariance are inter-related concepts that are applied in many fields such as mathematics,

geometry and geophysical sciences. In nature, there are many examples of fractals such as the Romanesco broccoli, river networks (Figure 2.3), geometry of the coastline (Mandelbrot, 1967) and some hydraulics phenomena (Heller, 2017). Richardson (1922) showed that in developed turbulent flows, the energy passes from large to small scale eddies via self-similar cascades. Kolmogorov (1991) investigated the energy distribution through the eddies and showed that the energy spectrum follows a power law with an exponent $-5/3$.

Note that a self-similar object can be described by a power law (Heller, 2017; Henriksen, 2015; Zohuri, 2015). This important property of self-similarity leads to the concept of scale-invariance. As such, the scaling of an object that follows suitable laws results in a self-similar scaled copy of the object itself and a self-similar process behaves the same way at different scales, such that scale effects are avoided.

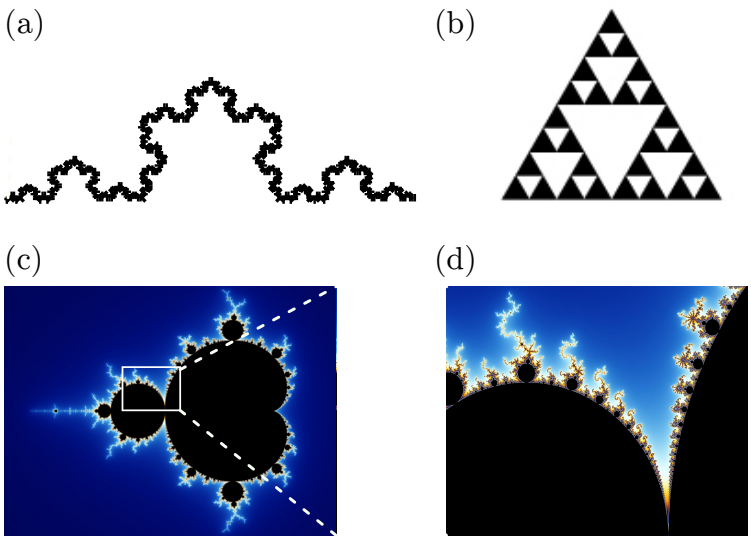


Figure 2.4: Examples of fractals: (a) Sierpiński triangle, (b) snowflake pattern, (c) the Mandelbrot set and (d) zoom of Mandelbrot set (Mandelbrot and Mandelbrot, 1982).

Here, these concepts are used to guarantee self-similarity through scales. In this way, the conditions under which two or more systems are scale-

invariant are found. As such, the model scaled under these conditions does not involve scale effects with respect to its prototype.

2.5.1 Scaling approach based on Lie group of point scaling transformations

In the last decade, a novel method to derive scaling laws has been applied to hydrology and hydraulics phenomena. This is based on a mathematical technique developed by mathematicians for symmetry analysis of differential equations. A group of continuous transformation, known as the Lie group of point scaling transformations, are used to find self-similarity in differential equations (Lie, 1880). Informally, a Lie group of point scaling transformations is a group of continuous symmetries. For example, a circle has a continuous group of symmetry such that any amount of rotation keeps the circle invariant. In contrast, a hexagon remains the same if the rotation is a multiple of one-sixth and the transformation is not continuous.

Lie group of point scaling transformations were originally used to reduce the number of independent parameters of an initial boundary value problem by transforming it in a new space where the solution of the problem is the same as the original. Subsequently, a subgroup of a Lie group of point scaling transformations called Lie group transformations herein has been used to derive the conditions under which the governing equations of hydrodynamics and sediment transport are self-similar (Carr et al., 2015; Ercan et al., 2014; Ercan and Kavvas, 2015a, 2017).

One of the most important advantages of this Lie group scaling method is that it does not introduce any limitations, meaning that the solutions are expected to be self-similar under the application of the Lie group transfor-

mation if the governing equations and the boundary conditions correctly capture the physics of the phenomenon (Kline, 1965; Zohuri, 2015).

By applying the scaling method to the 2D and 3D Reynolds-averaged Navier-Stokes (RANS), equations it is found that an important condition of self-similarity is the selection of a unique scaling exponent for length α_x and velocity α_U (Ercan and Kavvas, 2015a, 2017). This intuitive condition is present also in the traditional scaling method by imposing the geometric and kinematic similarity. Nevertheless, in the Lie group scaling method the selection of a unique scaling exponent for the length is not an assumption but is a necessity for the self-similarity of governing equations (Ercan and Kavvas, 2015a).

The scaling laws are always derived from the governing equations, such that the number of the scaling factors is the same as the number of the variables and physical parameters. In depth-averaged 2D flows the roughness of the bottom surface plays a central role. The flow is described by the continuity and momentum equations for nearly straight channels including an expression for the Coriolis parameters and the bed shear stresses (Wu, 2008). Hence, the Lie group scaling method results in scaling exponents for all the variables and physical parameters of the equations such as velocity, density, the shear stresses and the Manning roughness coefficient (Ercan and Kavvas, 2015a).

Another key advantage of the Lie group scaling method is that it is applied also to the boundary and initial conditions. In contrast, the classic scaling method is applied to the interior of the domain and not to the boundary conditions (Polsinelli and Kavvas, 2016). In this way, it can also capture the self-similar conditions of the boundary and initial conditions (Haltas and Kavvas, 2011; Ercan and Kavvas, 2015b).

It is worth mentioning that the Lie group scaling method does not resolve the laboratory limitations. The application of this method leads to a list of scaling exponents written in terms of independent parameters such as length, time and density. In a second stage, some restrictions can be used to adapt the derived scaling laws to the laboratory conditions (Ercan and Kavvas, 2017; Polsinelli and Kavvas, 2016). For example, the laboratory modelling of sediment transport requires a geometric similarity in relation to the sediment, that is difficult to achieve because the sediment grain size scaling introduces challenges including possible cohesion. Hence, not scaling the sediment size provides a practical advantage. After the derivation of general self-similar conditions for sediment transport, a new configuration of the derived scaling laws can be found by fixing the same grain size between models and the prototypes (Carr et al., 2015).

The only limitation of the Lie group scaling method in finding self-similar conditions are those of the governing equations to which the Lie group transformations are applied (Carr et al., 2015; Heller, 2017; Kline, 1965; Polsinelli and Kavvas, 2016; Zohuri, 2015). Hence, if the governing equations do not include surface tension effects, the derived scaling laws are not suitable for self-similarity in air-water flows. For air-water flow in which compressibility is important, further limitations are involved in the governing equations that do not include the the gas phase state equation and heat transfer equations. To the knowledge of the author, there are no studies addressing the analytical conditions for which the governing equations involving gravity, inertial, viscous, surface tension, compressible and heat transfer effects are simultaneously self-similar when scaled in size.

2.6 Summary

Laboratory models of air-water flows are usually designed with Froude scaling laws based on the similarity of the Froude number F, even if the Reynolds number R and Weber number W also play important roles in determining the amount of air entrainment. This is a limitation for two reasons: (i) scale effects arise because R and W are not correctly scaled and (ii) the Froude scaling laws do not give a complete picture of the conditions to avoid scale effects. Indeed, the traditional method to derive scaling laws is based on the initial assumption that an effect is dominant over the others. Hence, Froude scaling laws imply that the gravity forces are significant, the Reynolds scaling laws that the viscous forces are significant and the Weber scaling laws that the surface tension force is significant. However, some phenomena such as violent breaking wave impacts or wave energy converters involving oscillating water columns are influenced by the compressibility of air, which is not taken into account by the Froude scaling laws. Additional scale effects are potentially introduced because of the effects of temperature and because the thermophysical properties of air are neglected. There is no set of scaling laws that give the conditions under which a laboratory model of compressible air-water flow is free of scale effects.

A modern approach to derive scaling laws is based on the application of the one-parameter Lie group transformations (Lie group transformations) to the governing equations. In this way, the conditions under which systems at different scales are self-similar can be found. The scaling of a physical process that follows suitable laws results in a self-similar scaled copy of the process itself. This means that a self-similar process behaves the same way at different scales, such that scale effects are avoided. An advantage

of this novel scaling method is that it is applied to the governing equations and their boundary conditions, therefore it provides a complete picture of the conditions that all the parameters must satisfy to obtain self-similarity. In this study, the Lie group transformations are applied to the governing equations of incompressible and compressible air-water flows in order to find the conditions under which these phenomena involving inertial, gravity, surface tension and compressibility effects are self-similar when scaled in size.

Chapter 3

Derivation of the novel scaling laws

3.1 Introduction

In this section, NSLs are derived by applying the Lie group transformations to the governing equations of air-water flows, first retaining the assumption of incompressibility of water and air and including the surface tension, then by considering the compressibility of air. The derivation of the incompressible scaling laws essentially follows Catucci et al. (2021) and the ones considering the compressibility of air Catucci et al. (2022b). After the derivation, different configurations of the NSLs can be obtained by introducing some restrictions.

3.2 Derivation of the NSLs for incompressible air-water flows

3.2.1 Governing equations

Air-water flows are here described by the RANS equations for incompressible fluids:

$$\frac{\partial U_{\mathrm{j}}}{\partial x_{\mathrm{j}}} = 0 \tag{3.1}$$

and

$$\frac{\partial U_{\mathrm{i}}}{\partial t} + U_{\mathrm{j}}\frac{\partial U_{\mathrm{i}}}{\partial x_{\mathrm{j}}} = \frac{\partial}{\partial x_{\mathrm{j}}}\left(\nu\frac{\partial U_{\mathrm{i}}}{\partial x_{\mathrm{j}}} - \overline{u_{\mathrm{i}}u_{\mathrm{j}}}\right) - \frac{1}{\rho}\frac{\partial p}{\partial x_{\mathrm{i}}} + g_{\mathrm{i}} + \frac{1}{\rho}f_{\sigma}, \tag{3.2}$$

where i is the free index, j the dummy index, following Einstein's notation, t is time, x_{i} and x_{j} are the spatial coordinates, U_{i} and U_{j} the Reynolds-averaged flow velocity components, u_{i} and u_{j} the fluctuating velocity components, $\overline{u_{\mathrm{i}}u_{\mathrm{j}}}$ is the Reynolds stress term, p the Reynolds-averaged pressure, ν the kinematic viscosity, ρ the density of the fluid, $g_{\mathrm{i}} = (g_1, g_2, g_3)$ the gravitational acceleration vector and f_{σ} the surface tension force per unit volume defined as

$$f_{\sigma} = \sigma\kappa\frac{\partial\gamma}{\partial x_{\mathrm{i}}}. \tag{3.3}$$

In Eq. (3.3) σ is the surface tension constant, κ the curvature of the free surface and γ the phase fraction. This is a dimensionless parameter with values between 0 and 1 that is used to identify any air-water interface (see Section 3.4). The k-ϵ model is here applied for the Reynolds stresses in Eq.

(3.2) (see Pope, 2000 for more details), for which

$$-\overline{u_{\mathrm{i}}u_{\mathrm{j}}} = \nu_t\left(\frac{\partial U_{\mathrm{i}}}{\partial x_{\mathrm{j}}} + \frac{\partial U_{\mathrm{j}}}{\partial x_{\mathrm{i}}}\right) - \frac{2}{3}k\delta_{\mathrm{ij}}, \tag{3.4}$$

where k is the turbulent kinetic energy, δ_{ij} the Kronecker delta and ν_t the eddy viscosity

$$\nu_t = C_\mu k^2/\epsilon. \tag{3.5}$$

k, and its rate of dissipation ϵ, are calculated from

$$\frac{\partial k}{\partial t} + U_{\mathrm{j}}\frac{\partial k}{\partial x_{\mathrm{j}}} = P_k - \epsilon + \frac{\partial}{\partial x_{\mathrm{j}}}\left[(\nu + \nu_t/C_{\sigma_k})\frac{\partial k}{\partial x_{\mathrm{j}}}\right] \tag{3.6}$$

and

$$\frac{\partial \epsilon}{\partial t} + U_{\mathrm{j}}\frac{\partial \epsilon}{\partial x_{\mathrm{j}}} = C_{\epsilon 1}\frac{\epsilon}{k}P_k - C_{\epsilon 2}\frac{\epsilon^2}{k} + \frac{\partial}{\partial x_{\mathrm{j}}}\left[(\nu + \nu_t/C_{\sigma_\epsilon})\frac{\partial \epsilon}{\partial x_{\mathrm{j}}}\right]. \tag{3.7}$$

$P_k = u_t\frac{\partial U_{\mathrm{i}}}{\partial x_{\mathrm{j}}}\left(\frac{\partial U_{\mathrm{i}}}{\partial x_{\mathrm{j}}} + \frac{\partial U_{\mathrm{j}}}{\partial x_{\mathrm{i}}}\right)$ and $C_{\epsilon 1} = 1.44$, $C_{\epsilon 2} = 1.92$, $C_\mu = 0.09$, $C_{\sigma_k} = 1.0$ and $C_{\sigma_\epsilon} = 1.3$ are the standard model coefficients used in the k-ϵ turbulence model (Launder and Spalding, 1974).

3.2.2 Application of Lie group transformations

The Lie group transformations are defined as

$$\phi = \beta^{\alpha_\phi}\phi^*. \tag{3.8}$$

Eq. (3.8) transforms the parameter ϕ in the original space into the parameter ϕ^* in the transformed space (*), β is the scaling parameter and α_ϕ the scaling exponent of the parameter ϕ. Hence, the scaling ratio of the

parameter ϕ is $r_\phi = \phi/\phi^* = \beta^{\alpha_\phi}$. For example, the geometrical scale factor is $\lambda = \beta^{\alpha_x}$ and the scaling factor for the velocity is β^{α_U}. All the parameters of Eqs. (3.1) to (3.7) in the original domain are written in the transformed domain by using the Lie group transformations, as:

$$\begin{gathered}
x_1 = \beta^{\alpha_{x_1}} x_1^*, \quad x_2 = \beta^{\alpha_{x_2}} x_2^*, \quad x_3 = \beta^{\alpha_{x_3}} x_3^*, \quad t = \beta^{\alpha_t} t^*, \\
U_1 = \beta^{\alpha_{U_1}} U_1^*, \quad U_2 = \beta^{\alpha_{U_2}} U_2^*, \quad U_3 = \beta^{\alpha_{U_3}} U_3^*, \quad p = \beta^{\alpha_p} p^*, \\
g_{\mathrm{i}} = \beta^{\alpha_g} g_{\mathrm{i}}^*, \quad \rho = \beta^{\alpha_\rho} \rho^*, \quad \nu = \beta^{\alpha_\nu} \nu^*, \quad \sigma = \beta^{\alpha_\sigma} \sigma^*, \quad \kappa = \beta^{\alpha_\kappa} \kappa^*, \\
u_1 = \beta^{\alpha_{u_1}} u_1^*, \quad u_2 = \beta^{\alpha_{u_2}} u_2^*, \quad u_3 = \beta^{\alpha_{u_3}} u_3^*, \\
k = \beta^{\alpha_k} k^*, \quad \epsilon = \beta^{\alpha_\epsilon} \epsilon^*, \quad \nu_t = \beta^{\alpha_{\nu_t}} \nu_t^*, \quad P_k = \beta^{\alpha_{P_k}} P_k^*.
\end{gathered} \tag{3.9}$$

Self-similar conditions are obtained when the governing equations in the original domain, subjected to the Lie group transformations, remain invariant. The Lie group transformations for Eq. (3.1) yield the following equation in the transformed domain

$$\frac{\partial \beta^{\alpha_{U_1}} U_1^*}{\partial \beta^{\alpha_{x_1}} x_1^*} + \frac{\partial \beta^{\alpha_{U_2}} U_2^*}{\partial \beta^{\alpha_{x_2}} x_2^*} + \frac{\partial \beta^{\alpha_{U_3}} U_3^*}{\partial \beta^{\alpha_{x_3}} x_3^*} = 0, \tag{3.10}$$

which, with β being a constant parameter, is rearranged as

$$\beta^{\alpha_{U_1} - \alpha_{x_1}} \frac{\partial U_1^*}{\partial x_1^*} + \beta^{\alpha_{U_2} - \alpha_{x_2}} \frac{\partial U_2^*}{\partial x_2^*} + \beta^{\alpha_{U_3} - \alpha_{x_3}} \frac{\partial U_3^*}{\partial x_3^*} = 0. \tag{3.11}$$

Self-similarity is achieved if Eq. (3.11) can be obtained from Eq. (3.1) by means of a simple scaling process. Therefore, all terms of Eq. (3.11) must be transformed by using the same scaling ratios:

$$\beta^{\alpha_{U_1} - \alpha_{x_1}} = \beta^{\alpha_{U_2} - \alpha_{x_2}} = \beta^{\alpha_{U_3} - \alpha_{x_3}}, \tag{3.12}$$

which implies

$$\alpha_{U_1} - \alpha_{x_1} = \alpha_{U_2} - \alpha_{x_2} = \alpha_{U_3} - \alpha_{x_3}. \tag{3.13}$$

The Lie group transformations for Eq. (3.2) yield the following equations in the transformed domain:

$$\begin{aligned} \beta^{\alpha_{U_\mathrm{i}} - \alpha_t} \frac{\partial U_\mathrm{i}^*}{\partial t^*} + \beta^{\alpha_{U_\mathrm{j}} + \alpha_{U_\mathrm{i}} - \alpha_{x_\mathrm{j}}} U_\mathrm{j}^* \frac{\partial U_\mathrm{i}^*}{\partial x_\mathrm{j}^*} = \\ \beta^{\alpha_{U_\mathrm{i}} + \alpha_\nu - 2\alpha_{x_\mathrm{j}}} \frac{\partial}{\partial x_\mathrm{j}^*} \left(\nu^* \frac{\partial U_\mathrm{i}^*}{\partial x_\mathrm{j}^*} \right) - \beta^{\alpha_{\overline{u_\mathrm{i} u_\mathrm{j}}} - \alpha_{x_\mathrm{j}}} \frac{\partial \overline{u_\mathrm{i}^* u_\mathrm{j}^*}}{\partial x_\mathrm{j}^*} \\ - \beta^{\alpha_p - \alpha_\rho - \alpha_{x_\mathrm{i}}} \frac{1}{\rho^*} \frac{\partial p^*}{\partial x_\mathrm{i}^*} + \beta^{\alpha_g} g_\mathrm{i}^* + \beta^{\alpha_{f_\sigma} - \alpha_\rho} \frac{f_\sigma^*}{\rho}. \end{aligned} \tag{3.14}$$

Self-similarity is guaranteed if the scaling ratios of all terms in Eq. (3.14) are the same, implying that the exponents of all terms must be the same:

$$\begin{aligned} \alpha_{U_1} - \alpha_t &= \alpha_{U_1} + \alpha_{U_1} - \alpha_{x_1} = \alpha_{U_2} + \alpha_{U_1} - \alpha_{x_2} = \alpha_{U_3} + \alpha_{U_1} - \alpha_{x_3} \\ &= \alpha_{U_1} + \alpha_\nu - 2\alpha_{x_1} = \alpha_{U_1} + \alpha_\nu - 2\alpha_{x_2} = \alpha_{U_1} + \alpha_\nu - 2\alpha_{x_3} \\ &= \alpha_{\overline{u_1 u_1}} - \alpha_{x_1} = \alpha_{\overline{u_1 u_2}} - \alpha_{x_2} = \alpha_{\overline{u_1 u_3}} - \alpha_{x_3} \\ &= \alpha_p - \alpha_\rho - \alpha_{x_1} \\ &= \alpha_g \\ &= \alpha_{f_\sigma} - \alpha_\rho. \end{aligned} \tag{3.15}$$

$$\begin{aligned}
\alpha_{U_2} - \alpha_t &= \alpha_{U_1} + \alpha_{U_2} - \alpha_{x_1} = \alpha_{U_2} + \alpha_{U_2} - \alpha_{x_2} = \alpha_{U_3} + \alpha_{U_2} - \alpha_{x_3} \\
&= \alpha_{U_2} + \alpha_\nu - 2\alpha_{x_1} = \alpha_{U_2} + \alpha_\nu - 2\alpha_{x_2} = \alpha_{U_2} + \alpha_\nu - 2\alpha_{x_3} \\
&= \alpha_{\overline{u_2 u_1}} - \alpha_{x_1} = \alpha_{\overline{u_2 u_2}} - \alpha_{x_2} = \alpha_{\overline{u_2 u_3}} - \alpha_{x_3} \\
&= \alpha_p - \alpha_\rho - \alpha_{x_2} \\
&= \alpha_g \\
&= \alpha_{f_\sigma} - \alpha_\rho.
\end{aligned} \tag{3.16}$$

$$\begin{aligned}
\alpha_{U_3} - \alpha_t &= \alpha_{U_1} + \alpha_{U_3} - \alpha_{x_1} = \alpha_{U_2} + \alpha_{U_3} - \alpha_{x_2} = \alpha_{U_3} + \alpha_{U_3} - \alpha_{x_3} \\
&= \alpha_{U_3} + \alpha_\nu - 2\alpha_{x_1} = \alpha_{U_3} + \alpha_\nu - 2\alpha_{x_2} = \alpha_{U_3} + \alpha_\nu - 2\alpha_{x_3} \\
&= \alpha_{\overline{u_3 u_1}} - \alpha_{x_1} = \alpha_{\overline{u_3 u_2}} - \alpha_{x_2} = \alpha_{\overline{u_3 u_3}} - \alpha_{x_3} \\
&= \alpha_p - \alpha_\rho - \alpha_{x_3} \\
&= \alpha_g \\
&= \alpha_{f_\sigma} - \alpha_\rho.
\end{aligned} \tag{3.17}$$

The Lie group transformations for Eq. (3.3) result in

$$\beta^{\alpha_{f_\sigma}} f_\sigma^* = \beta^{\alpha_\sigma + \alpha_\kappa + \alpha_\gamma - \alpha_{x_\mathrm{i}}} \sigma^* \kappa^* \frac{\partial \gamma^*}{\partial x_\mathrm{i}^*}. \tag{3.18}$$

The dimension of κ is the inverse of a length, such that $\alpha_\kappa = -\alpha_{x_\mathrm{i}}$. Further, $\alpha_\gamma = 0$ because γ is dimensionless. Hence, Eq. (3.18) reduces to

$$\alpha_{f_\sigma} = \alpha_\sigma - 2\alpha_{x_\mathrm{i}}. \tag{3.19}$$

From Eqs. (3.15) to (3.17) the scaling exponents of the length dimensions

along the i$^{\text{th}}$ axis are obtained as

$$\alpha_{U_1} - \alpha_t = \alpha_{U_1} + \alpha_\nu - 2\alpha_{x_1} \quad \Rightarrow \quad \alpha_{x_1} = \frac{\alpha_t + \alpha_\nu}{2}, \tag{3.20}$$

$$\alpha_{U_2} - \alpha_t = \alpha_{U_2} + \alpha_\nu - 2\alpha_{x_2} \quad \Rightarrow \quad \alpha_{x_2} = \frac{\alpha_t + \alpha_\nu}{2}, \tag{3.21}$$

$$\alpha_{U_3} - \alpha_t = \alpha_{U_3} + \alpha_\nu - 2\alpha_{x_3} \quad \Rightarrow \quad \alpha_{x_3} = \frac{\alpha_t + \alpha_\nu}{2}. \tag{3.22}$$

In other words, the scaling exponents of the length scale must be identical for i $= 1, 2, 3$ because the fluids are considered isotropic, therefore

$$\alpha_{x_1} = \alpha_{x_2} = \alpha_{x_3} = \alpha_x. \tag{3.23}$$

Similarly, α_{U_1}, α_{U_2} and α_{U_3} are obtained from Eqs. (3.15) to (3.17) as follows:

$$\alpha_{U_1} - \alpha_t = \alpha_{U_1} + \alpha_{U_1} - \alpha_x \quad \Rightarrow \quad \alpha_{U_1} = \alpha_x - \alpha_t, \tag{3.24}$$

$$\alpha_{U_2} - \alpha_t = \alpha_{U_2} + \alpha_{U_2} - \alpha_x \quad \Rightarrow \quad \alpha_{U_2} = \alpha_x - \alpha_t, \tag{3.25}$$

$$\alpha_{U_3} - \alpha_t = \alpha_{U_3} + \alpha_{U_3} - \alpha_x \quad \Rightarrow \quad \alpha_{U_3} = \alpha_x - \alpha_t. \tag{3.26}$$

Hence, α_{U_1}, α_{U_2} and α_{U_3} are also equal;

$$\alpha_{U_1} = \alpha_{U_2} = \alpha_{U_3} = \alpha_U = \alpha_x - \alpha_t. \tag{3.27}$$

Consequently, u_1, u_2 and u_3 have the same exponents in all directions as well because they are transformed by using the velocity ratio

$$\alpha_{u_1} = \alpha_{u_2} = \alpha_{u_3} = \alpha_u. \tag{3.28}$$

The results in Eqs. (3.23) to (3.28) are important because the selection of unique scaling exponents for length and velocity across the three axes is necessary to achieve self-similarity of air-water flows. Hereafter, α_x, α_U and

α_u are used to indicate the scaling exponents of length, Reynolds-averaged velocity and fluctuating velocity components on the i$^{\text{th}}$ axis.

α_g, α_p and α_ν are obtained from Eqs. (3.15) to (3.17) and they can be written in terms of α_x, α_t and α_ρ as

$$\alpha_U - \alpha_t = \alpha_g \quad \Rightarrow \quad \alpha_g = \alpha_x - 2\alpha_t, \tag{3.29}$$

$$\alpha_U - \alpha_t = \alpha_p - \alpha_\rho - \alpha_x \quad \Rightarrow \quad \alpha_p = 2\alpha_x - 2\alpha_t + \alpha_\rho, \tag{3.30}$$

$$\alpha_U - \alpha_t = \alpha_U + \alpha_\nu - 2\alpha_x \quad \Rightarrow \quad \alpha_\nu = 2\alpha_x - \alpha_t. \tag{3.31}$$

By using Eqs. (3.15) and (3.19)

$$\alpha_U - \alpha_t = \alpha_{f_\sigma} - \alpha_\rho \quad \Rightarrow \quad \alpha_x - 2\alpha_t = \alpha_\sigma - 2\alpha_x - \alpha_\rho, \tag{3.32}$$

from which

$$\alpha_\sigma = 3\alpha_x - 2\alpha_t + \alpha_\rho. \tag{3.33}$$

Similarly, Eqs. (3.4) to (3.7) are transformed by keeping $C_{\epsilon 1}$, $C_{\epsilon 2}$, C_μ, C_{σ_k} and C_{σ_ϵ} as dimensionless coefficients

$$-\beta^{\alpha_{\overline{uu}}}\overline{u_{\mathrm{i}}^* u_{\mathrm{j}}^*} = \beta^{\alpha_{\nu_t}+\alpha_U-\alpha_x}\nu_t^*\frac{\partial U_{\mathrm{i}}^*}{\partial x_{\mathrm{j}}^*} + \beta^{\alpha_{\nu_t}+\alpha_U-\alpha_x}\nu_t^*\frac{\partial U_{\mathrm{j}}^*}{\partial x_{\mathrm{i}}^*} - \frac{2}{3}\beta^{\alpha_k}k^*\delta_{\mathrm{ij}}, \tag{3.34}$$

$$\beta^{\alpha_{\nu_t}}\nu_t^* = \beta^{2\alpha_k-\alpha_\epsilon}C_\mu\frac{k^{*2}}{\epsilon^*}, \tag{3.35}$$

$$\begin{aligned}
&\beta^{\alpha_k-\alpha_t}\frac{\partial k^*}{\partial t^*}+\beta^{\alpha_U+\alpha_k-\alpha_x}U_{\mathrm{j}}^*\frac{\partial k^*}{\partial x_{\mathrm{j}}^*}= \\
&\beta^{\alpha_{P_k}}P_k^*-\beta^{\alpha_\epsilon}\epsilon^*+\beta^{\alpha_\nu+\alpha_k-2\alpha_x}\frac{\partial}{\partial x_{\mathrm{j}}^*}\left(\nu^*\frac{\partial k^*}{\partial x_{\mathrm{j}}^*}\right) \\
&+\beta^{\alpha_{\nu_t}+\alpha_k-2\alpha_x}\frac{\partial}{\partial x_{\mathrm{j}}^*}\left(\nu_t^*/C_{\sigma_k}\frac{\partial k^*}{\partial x_{\mathrm{j}}^*}\right)
\end{aligned} \tag{3.36}$$

and

$$\begin{aligned}
&\beta^{\alpha_\epsilon-\alpha_t}\frac{\partial \epsilon^*}{\partial t^*}+\beta^{\alpha_U+\alpha_\epsilon-\alpha_x}U_{\mathrm{j}}^*\frac{\partial \epsilon^*}{\partial x_{\mathrm{j}}^*} \\
&=\beta^{\alpha_\epsilon+\alpha_{P_k}-\alpha_k}C_{\epsilon 1}\frac{\epsilon^*}{k^*}P_k^*-\beta^{2\alpha_\epsilon-\alpha_k}C_{\epsilon 2}\frac{\epsilon^{*2}}{k^*} \\
&+\beta^{\alpha_\nu+\alpha_\epsilon-2\alpha_x}\frac{\partial \nu^*}{\partial x_{\mathrm{j}}^*}\left(\frac{\partial \epsilon^*}{\partial x_{\mathrm{j}}^*}\right)+\beta^{\alpha_{\nu_t}+\alpha_\epsilon-2\alpha_x}\frac{\partial}{\partial x_{\mathrm{j}}^*}\left[\left(\frac{\nu_t^*}{C_{\sigma_\epsilon}}\right)\frac{\partial \epsilon^*}{\partial x_{\mathrm{j}}^*}\right].
\end{aligned} \tag{3.37}$$

For Eqs. (3.34) to (3.37) to be self-similar, the following conditions must hold:

$$\begin{aligned}
\alpha_{\overline{uu}} &= \alpha_{\nu_t}+\alpha_U-\alpha_x \\
&= \alpha_{\nu_t}+\alpha_U-\alpha_x \\
&= \alpha_k,
\end{aligned} \tag{3.38}$$

$$\alpha_{\nu_t} = 2\alpha_k-\alpha_\epsilon, \tag{3.39}$$

$$\begin{aligned}
\alpha_k-\alpha_t &= \alpha_U+\alpha_k-\alpha_x \\
&= \alpha_{P_k} \\
&= \alpha_\epsilon \\
&= \alpha_\nu+\alpha_k-2\alpha_x \\
&= \alpha_{\nu_t}+\alpha_k-2\alpha_x
\end{aligned} \tag{3.40}$$

and

$$\begin{aligned}\alpha_\epsilon - \alpha_t &= \alpha_U + \alpha_\epsilon - \alpha_x \\ &= \alpha_\epsilon + \alpha_{P_k} - \alpha_k \\ &= 2\alpha_\epsilon - \alpha_k \\ &= \alpha_\nu + \alpha_\epsilon - 2\alpha_x \\ &= \alpha_{\nu_t} + \alpha_\epsilon - 2\alpha_x.\end{aligned} \tag{3.41}$$

From Eq. (3.40)

$$\alpha_k - \alpha_t = \alpha_{\nu_t} + \alpha_k - 2\alpha_x \quad \Rightarrow \quad \alpha_{\nu_t} = 2\alpha_x - \alpha_t. \tag{3.42}$$

$\alpha_{\overline{uu}}$ is the same in all directions and it is calculated from Eqs. (3.38) and (3.42) as

$$\alpha_{\overline{uu}} = \alpha_{\nu_t} + \alpha_U - \alpha_x \quad \Rightarrow \quad \alpha_{\overline{uu}} = 2\alpha_x - 2\alpha_t. \tag{3.43}$$

From Eq. (3.38) α_k is obtained ($\alpha_k = 2\alpha_x - 2\alpha_t$). Finally, α_ϵ and α_{P_k} are obtained from Eqs. (3.39) and (3.40) as

$$\alpha_\epsilon = 2\alpha_k - \alpha_{\nu_t} \quad \Rightarrow \quad \alpha_\epsilon = 2\alpha_x - 3\alpha_t, \tag{3.44}$$

$$\alpha_{P_k} = \alpha_k - \alpha_t \quad \Rightarrow \quad \alpha_{P_k} = 2\alpha_x - 3\alpha_t. \tag{3.45}$$

The scaling conditions derived above are summarised in the second column of Table 3.1. They are consistent with those reported in Tables 1 and 2 in Ercan and Kavvas (2017) with addition of the surface tension and the curvature of the free surface. All the exponents are written in terms of three independent scaling exponents, namely α_x, α_t and α_ρ, meaning that they are user-defined (their choice is flexible). In fact, the solution of air-water

flow equations can be mapped to solutions in other transformed domains with different $\lambda = \beta^{\alpha_x}$ by selecting the scaling parameter β and changing α of three independent parameters.

Table 3.1: NSLs and PFs for the parameters of the RANS equations and the k-ϵ turbulence model obtained by applying the Lie group transformations.

Parameters	**Written in terms of α_x, α_t and α_ρ (NSLs)**		**Written in terms of α_x, α_ρ and $\alpha_g = 0$**		**Written in terms of α_x, $\alpha_\rho = \alpha_g = 0$ (PFs)**	
	Exponents	**Scaling ratios**	**Exponents**	**Scaling ratios**	**Exponents**	**Scaling ratios**
x_i (m)	α_x	β^{α_x}	α_x	β^{α_x}	α_x	$\beta^{\alpha_x} = \lambda$
t (s)	α_t	β^{α_t}	$\alpha_t = 0.5\alpha_x$	$\beta^{0.5\alpha_x}$	$\alpha_t = 0.5\alpha_x$	$\beta^{0.5\alpha_x} = \lambda^{0.5}$
ρ (kg m^{-3})	α_ρ	β^{α_ρ}	α_ρ	β^{α_ρ}	$\alpha_\rho = 0$	$\beta^0 = 1$
U_i (m s^{-1})	$\alpha_U = \alpha_x - \alpha_t$	$\beta^{\alpha_x - \alpha_t}$	$\alpha_U = 0.5\alpha_x$	$\beta^{0.5\alpha_x}$	$\alpha_U = 0.5\alpha_x$	$\beta^{0.5\alpha_x} = \lambda^{0.5}$
p (Pa)	$\alpha_p = 2\alpha_x - 2\alpha_t + \alpha_\rho$	$\beta^{2\alpha_x - 2\alpha_t + \alpha_\rho}$	$\alpha_p = \alpha_x + \alpha_\rho$	$\beta^{\alpha_x + \alpha_\rho}$	$\alpha_p = \alpha_x$	$\beta^{\alpha_x} = \lambda$
g_i (m s^{-2})	$\alpha_g = \alpha_x - 2\alpha_t$	$\beta^{\alpha_x - 2\alpha_t}$	$\alpha_g = 0$	$\beta^0 = 1$	$\alpha_g = 0$	$\beta^0 = 1$
ν (m^2 s^{-1})	$\alpha_\nu = 2\alpha_x - \alpha_t$	$\beta^{2\alpha_x - \alpha_t}$	$\alpha_\nu = 1.5\alpha_x$	$\beta^{1.5\alpha_x}$	$\alpha_\nu = 1.5\alpha_x$	$\beta^{1.5\alpha_x} = \lambda^{1.5}$
σ (N m^{-1})	$\alpha_\sigma = 3\alpha_x - 2\alpha_t + \alpha_\rho$	$\beta^{3\alpha_x - 2\alpha_t + \alpha_\rho}$	$\alpha_\sigma = 2\alpha_x + \alpha_\rho$	$\beta^{2\alpha_x + \alpha_\rho}$	$\alpha_\sigma = 2\alpha_x$	$\beta^{2\alpha_x} = \lambda^2$
κ (1 m^{-1})	$\alpha_\kappa = \alpha_x^{-1}$	$\beta^{\alpha_x^{-1}}$	$\alpha_\kappa = \alpha_x^{-1}$	$\beta^{\alpha_x^{-1}}$	$\alpha_\kappa = \alpha_x^{-1}$	$\beta^{\alpha^{-1}} = \lambda^{-1}$
ν_t (m^2 s^{-1})	$\alpha_{\nu_t} = 2\alpha_x - \alpha_t$	$\beta^{2\alpha_x - \alpha_t}$	$\alpha_{\nu_t} = 1.5\alpha_x$	$\beta^{1.5\alpha_x}$	$\alpha_{\nu_t} = 1.5\alpha_x$	$\beta^{1.5\alpha_x} = \lambda^{1.5}$
$\overline{u_\mathrm{i}u_\mathrm{j}}$ (m^2 s^{-2})	$\alpha_{\overline{u_\mathrm{i}u_\mathrm{j}}} = 2\alpha_x - 2\alpha_t$	$\beta^{2\alpha_x - 2\alpha_t}$	$\alpha_{\overline{u_\mathrm{i}u_\mathrm{j}}} = \alpha_x$	β^{α_x}	$\alpha_{\overline{u_\mathrm{i}u_\mathrm{j}}} = \alpha_x$	$\beta^{\alpha_x} = \lambda$
k (m^2 s^{-2})	$\alpha_k = 2\alpha_x - 2\alpha_t$	$\beta^{2\alpha_x - 2\alpha_t}$	$\alpha_k = \alpha_x$	β^{α_x}	$\alpha_k = \alpha_x$	$\beta^{\alpha_x} = \lambda$
ϵ (m^2 s^{-3})	$\alpha_\epsilon = 2\alpha_x - 3\alpha_t$	$\beta^{2\alpha_x - 3\alpha_t}$	$\alpha_\epsilon = 0.5\alpha_x$	$\beta^{0.5\alpha_x}$	$\alpha_\epsilon = 0.5\alpha_x$	$\beta^{0.5\alpha_x} = \lambda^{0.5}$
P_k (m^2 s^{-3})	$\alpha_{P_k} = 2\alpha_x - 3\alpha_t$	$\beta^{2\alpha_x - 3\alpha_t}$	$\alpha_{P_k} = 0.5\alpha_x$	$\beta^{0.5\alpha_x}$	$\alpha_{P_k} = 0.5\alpha_x$	$\beta^{0.5\alpha_x} = \lambda^{0.5}$

It is possible to fix the value of some parameters in the model and assign the value of the corresponding α while still preserving self-similarity. For example, in Table 3.1 it is shown that choosing $\alpha_g = 0$ implies that $\alpha_g = \alpha_x - 2\alpha_t = 0$. Therefore, the unscaled g requires that $\alpha_t = 0.5\alpha_x$, i.e. the time is not anymore an independent parameter. In this configuration, the remaining scaling exponents are written in terms of the exponents for x_i and ρ as independent parameters and g as a fixed parameter, i.e. α_x, α_ρ and $\alpha_g = 0$ (fourth and fifth columns of Table 3.1). Hence, keeping g invariant in a scaled model requires to scale time and flow velocities and to change the properties of the fluids to obtain a self-similar behaviour. Usually, the Froude scaling laws are used by imposing the same density of fluids between the prototype and its model. Indeed this restriction in the NSL ($\alpha_\rho = 0$) leads to the precise Froude scaling laws, in which the properties of the fluids are strictly scaled, i.e. the PFs, as a particular case of the NSLs, where g is constant and ν and σ are scaled by keeping R and

W invariant.

3.3 Derivation of the NSLs for compressible air-water flows

3.3.1 Governing equations

The governing equations for compressible air-water flows are described by the conservation laws of mass (continuity), momentum and energy. The continuity and momentum equations are

$$\frac{\partial \rho}{\partial t} + \frac{\partial \rho U_\mathrm{j}}{\partial x_\mathrm{j}} = 0, \tag{3.46}$$

$$\frac{\partial \rho U_\mathrm{i}}{\partial t} + U_\mathrm{j}\frac{\partial \rho U_\mathrm{i}}{\partial x_\mathrm{j}} = \frac{\partial}{\partial x_\mathrm{j}}\left(\mu\frac{\partial U_\mathrm{i}}{\partial x_\mathrm{j}} - \rho\overline{u_\mathrm{i}u_\mathrm{j}}\right) - \frac{\partial p}{\partial x_\mathrm{i}} + \rho g_\mathrm{i} + f_\sigma, \tag{3.47}$$

where f_σ is defined by Eq. (3.3). The energy conservation equation is

$$\frac{\partial \rho T}{\partial t} + U_\mathrm{j}\frac{\partial T}{\partial x_\mathrm{j}} = \tag{3.48}$$
$$\frac{\partial}{\partial x_\mathrm{j}}\left(\mu\frac{\partial T}{\partial x_\mathrm{j}}\right) + \left(\frac{\gamma}{c_{v,w}} + \frac{1-\gamma}{c_{v,a}}\right)\left(-\frac{\partial \rho k}{\partial t} - U_\mathrm{j}\frac{\partial \rho k}{\partial x_\mathrm{j}} - U_\mathrm{j}\frac{\partial p}{\partial x_\mathrm{j}}\right),$$

where T is the temperature (K), $c_{v,w}$ and $c_{v,a}$ ($\mathrm{m^2\ K^{-1}\ s^{-2}}$) are the specific heat capacities at constant volume for water and air, respectively (Van Wylen and Sonntag, 1985). The density of air ρ_a is expressed as a function of p and T by the ideal gas law:

$$\rho_a = \frac{p}{RT}, \tag{3.49}$$

in which

$$R = \frac{R_u}{M_m} = 287\,\mathrm{m^2\,K^{-1}\,s^{-2}} \tag{3.50}$$

is the specific gas constant. $R_u = 8.314$ J mol^{-1}K^{-1} is the ideal gas constant and $M_m = 0.289$ kg mol^{-1} the molar mass of air. Eq. (3.50) is written in terms of the volume V and the number of moles n as

$$nT = \frac{pV}{R_u}. \tag{3.51}$$

The unit of n is mol, i.e. the amount of substance ($n = N/N_A$ with N_A as the Avogadro number and n the number of specific elementary entity (AMCAN86, 2019). In this section, the water phase is assumed to be incompressible with the density ρ_w constant and energy transformations are assumed to be isothermal. The equations of the k-ϵ turbulence model is unchanged with respect to the incompressible case (Eqs. (3.4) to (3.7) in Section 3.2.1).

3.3.2 Application of Lie group transformations

All the parameters of Eqs. (3.46) to (3.51) and of the k-ϵ turbulence model in the original domain are written in the transformed domain as:

$$\begin{gathered}
x_1 = \beta^{\alpha_{x_1}} x_1^*, \quad x_2 = \beta^{\alpha_{x_2}} x_2^*, \quad x_3 = \beta^{\alpha_{x_3}} x_3^*, \quad t = \beta^{\alpha_t} t^*, \\
U_1 = \beta^{\alpha_{U_1}} U_1^*, \quad U_2 = \beta^{\alpha_{U_2}} U_2^*, \quad U_3 = \beta^{\alpha_{U_3}} U_3^*, \quad p = \beta^{\alpha_p} p^*, \\
g_{\mathrm{i}} = \beta^{\alpha_g} g_{\mathrm{i}}^*, \quad \rho = \beta^{\alpha_\rho} \rho^*, \quad \nu = \beta^{\alpha_\nu} \nu^*, \quad \sigma = \beta^{\alpha_\sigma} \sigma^*, \quad \kappa = \beta^{\alpha_\kappa} \kappa^*, \\
u_1 = \beta^{\alpha_{u_1}} u_1^*, \quad u_2 = \beta^{\alpha_{u_2}} u_2^*, \quad u_3 = \beta^{\alpha_{u_3}} u_3^*, \\
T = \beta^{\alpha_T} T^*, \quad R = \beta^{\alpha_R} R^*, \quad c_{v,w} = \beta^{\alpha_{c_{v,w}}} c_{v,w}^*, \quad c_{v,a} = \beta^{\alpha_{c_{v,a}}} c_{v,a}^*, \\
\alpha_{M_m} = \beta^{\alpha_{M_m}} M_m^* \quad \text{and} \quad \alpha_n = \beta^{\alpha_n} n^*.
\end{gathered} \tag{3.52}$$

In Section 3.2.2, it is demonstrated that each of the parameters x_{i}, U_{i} and u_{i} need to have the same scaling factor in order to achieve self-similarity. Hence, α_x is the unique exponent for length, α_U for velocity and $\alpha_{\overline{uu}}$ for the Reynolds stress term. The Lie group transformations for Eq. (3.46) yield the following equations in the transformed domain

$$\beta^{\alpha_\rho - \alpha_t} \frac{\partial \rho^*}{\partial t^*} + \beta^{\alpha_\rho + \alpha_U - \alpha_x} \frac{\partial \rho^* U_{\mathrm{j}}^*}{\partial x_{\mathrm{j}}^*} = 0. \tag{3.53}$$

Self-similarity is guaranteed if the scaling ratios of all terms in Eq. (3.53) are the same, implying that the exponents of all terms must also be the same

$$\alpha_\rho - \alpha_t = \alpha_\rho + \alpha_U - \alpha_x \Rightarrow \alpha_U = \alpha_x - \alpha_t. \tag{3.54}$$

This confirms that the scaling condition for the velocity is the same as for incompressible flows (Section 3.2.2). The Lie group transformations for Eq.

(3.47) yield the following equation in the transformed domain:

$$\begin{aligned}\beta^{\alpha_\rho+\alpha_U-\alpha_t}\frac{\partial\rho^*U_{\mathrm{i}}^*}{\partial t^*}+\beta^{2\alpha_U+\alpha_\rho-\alpha_x}U_{\mathrm{j}}^*\frac{\partial\rho^*U_{\mathrm{i}}^*}{\partial x_{\mathrm{j}}^*}=\\ \beta^{\alpha_\mu+\alpha_U-2\alpha_x}\frac{\partial}{\partial x_{\mathrm{j}}^*}\left(\mu^*\frac{\partial U_{\mathrm{i}}^*}{\partial x_{\mathrm{j}}^*}\right)-\beta^{\alpha_\rho+\alpha_{\overline{uu}}-\alpha_x}\frac{\partial}{\partial x_{\mathrm{j}}^*}(\rho^*\overline{u_{\mathrm{i}}^*u_{\mathrm{j}}^*})-\\ \beta^{\alpha_p-\alpha_x}\frac{\partial p^*}{\partial x_{\mathrm{j}}^*}+\beta^{\alpha_\rho+\alpha_g}\rho^*g_{\mathrm{i}}^*+\beta^{\alpha_{f_\sigma}}f_\sigma^*.\end{aligned}\tag{3.55}$$

Eq. (3.55) is self-similar if

$$\begin{aligned}\alpha_\rho+\alpha_U-\alpha_t&=2\alpha_U+\alpha_\rho-\alpha_x\\ &=\alpha_\mu+\alpha_U-2\alpha_x\\ &=\alpha_\rho+\alpha_{\overline{uu}}-\alpha_x\\ &=\alpha_p-\alpha_x\\ &=\alpha_\rho+\alpha_g\\ &=\alpha_{f_\sigma}.\end{aligned}\tag{3.56}$$

α_g, α_p and α_μ are obtained from Eq. (3.56) and they can be written in terms of α_x, α_t and α_ρ as

$$\alpha_\rho+\alpha_U-\alpha_t=\alpha_\rho+\alpha_g\quad\Rightarrow\quad\alpha_g=\alpha_x-2\alpha_t,\tag{3.57}$$

$$\alpha_\rho+\alpha_U-\alpha_t=\alpha_p-\alpha_x\quad\Rightarrow\quad\alpha_p=2\alpha_x-2\alpha_t+\alpha_\rho.\tag{3.58}$$

$$\alpha_\rho+\alpha_U-\alpha_t=\alpha_\mu+\alpha_U-2\alpha_x\quad\Rightarrow\quad\alpha_\mu=\alpha_\rho+2\alpha_x-\alpha_t.\tag{3.59}$$

By using Eqs. (3.56) and (3.19)

$$\alpha_U-\alpha_t=\alpha_{f_\sigma}-\alpha_\rho\quad\Rightarrow\quad\alpha_x-2\alpha_t=\alpha_\sigma-2\alpha_x-\alpha_\rho,\tag{3.60}$$

from which

$$\alpha_\sigma = 3\alpha_x - 2\alpha_t + \alpha_\rho. \tag{3.61}$$

Therefore, α_g, α_p and α_ρ are also the same as the in incompressible case.

Eq. (3.48) is rearranged as follows, before the Lie group transformations are applied:

$$\begin{aligned}\frac{\partial \rho T}{\partial t} + U_{\mathrm{j}}\frac{\partial \rho T}{\partial x_{\mathrm{j}}} = \frac{\partial}{\partial x_{\mathrm{j}}}\left(\mu\frac{\partial T}{\partial x_{\mathrm{j}}}\right) - \frac{\gamma}{c_{v,w}}\frac{\partial \rho k}{\partial t} \\ -\frac{\gamma}{c_{v,w}}U_{\mathrm{j}}\frac{\partial \rho k}{\partial x_{\mathrm{j}}} - \frac{\gamma}{c_{v,w}}U_{\mathrm{j}}\frac{\partial p}{\partial x_{\mathrm{j}}} \\ -\frac{1-\gamma}{c_{v,a}}\frac{\partial \rho k}{\partial t} - \frac{1-\gamma}{c_{v,a}}U_{\mathrm{j}}\frac{\partial \rho k}{\partial x_{\mathrm{j}}} - \frac{1-\gamma}{c_{v,a}}U_{\mathrm{j}}\frac{\partial p}{\partial x_{\mathrm{j}}}.\end{aligned} \tag{3.62}$$

Eq. (3.62) in the transformed domain is

$$\begin{aligned}\beta^{\alpha_\rho+\alpha_T-\alpha_t}\frac{\partial \rho^* T^*}{\partial t^*} + \beta^{\alpha_U+\alpha_\rho+\alpha_T-\alpha_x}U_{\mathrm{j}}^*\frac{\partial \rho^* T^*}{\partial x_{\mathrm{j}}^*} = \\ \beta^{\alpha_\mu+\alpha_T-2\alpha_x}\frac{\partial}{\partial x_{\mathrm{j}}^*}\left(\mu^*\frac{\partial T^*}{\partial x_{\mathrm{j}}^*}\right) - \beta^{\alpha_\gamma+\alpha_\rho+\alpha_k-\alpha_{c_{v,w}}-\alpha_t}\frac{\gamma^*}{c_{v,w}^*}\frac{\partial \rho^* k^*}{\partial t^*} \\ -\beta^{\alpha_\gamma+\alpha_U+\alpha_\rho+\alpha_k-\alpha_{c_{v,w}}-\alpha_x}\frac{\gamma^*}{c_{v,w}^*}U_{\mathrm{j}}^*\frac{\partial \rho^* k^*}{\partial x_{\mathrm{j}}^*} - \beta^{\alpha_\gamma+\alpha_U+\alpha_p-\alpha_{c_{v,w}}-\alpha_x}\frac{\gamma^*}{c_{v,w}^*}U_{\mathrm{j}}^*\frac{\partial p^*}{\partial x_{\mathrm{j}}^*}\end{aligned} \tag{3.63}$$

$$\begin{aligned}-\beta^{\alpha_\rho+\alpha_k-\alpha_{c_{v,a}}-\alpha_t}\frac{1}{c_{v,a}^*}\frac{\partial \rho^* k^*}{\partial t^*} + \beta^{\alpha_\gamma+\alpha_\rho+\alpha_k-\alpha_{c_{v,a}}-\alpha_t}\frac{\gamma^*}{c_{v,a}^*}\frac{\partial \rho^* k^*}{\partial t^*} \\ -\beta^{\alpha_U+\alpha_\rho+\alpha_k-\alpha_{c_{v,a}}-\alpha_x}\frac{1}{c_{v,a}^*}U_{\mathrm{j}}^*\frac{\partial \rho^* k^*}{\partial x_{\mathrm{j}}^*} + \beta^{\alpha_\gamma+\alpha_U+\alpha_\rho+\alpha_k-\alpha_{c_{v,a}}-\alpha_x}\frac{\gamma^*}{c_{v,a}^*}U_{\mathrm{j}}^*\frac{\partial \rho^* k^*}{\partial x_{\mathrm{j}}^*} \\ -\beta^{\alpha_U+\alpha_p-\alpha_{c_{v,a}}-\alpha_x}\frac{1}{c_{v,a}^*}U_{\mathrm{j}}^*\frac{\partial p^*}{\partial x_{\mathrm{j}}^*} + \beta^{\alpha_\gamma+\alpha_U+\alpha_p-\alpha_{c_{v,a}}-\alpha_x}\frac{\gamma^*}{c_{v,a}^*}U_{\mathrm{j}}^*\frac{\partial p^*}{\partial x_{\mathrm{j}}^*}.\end{aligned}$$

Eq. (3.63) is self-similar if

$$\begin{aligned}
\alpha_\rho + \alpha_T - \alpha_t &= \alpha_U + \alpha_\rho + \alpha_T - \alpha_x \\
&= \alpha_\mu + \alpha_T - 2\alpha_x \\
&= \alpha_\gamma + \alpha_\rho + \alpha_k - \alpha_{c_{v,w}} - \alpha_t \\
&= \alpha_\gamma + \alpha_U + \alpha_\rho + \alpha_k - \alpha_{c_{v,w}} - \alpha_x \\
&= \alpha_\gamma + \alpha_U + \alpha_p - \alpha_{c_{v,w}} - \alpha_x \qquad (3.64) \\
&= \alpha_\rho + \alpha_k - \alpha_{c_{v,a}} - \alpha_t = \alpha_\gamma + \alpha_\rho + \alpha_k - \alpha_{c_{v,a}} - \alpha_t \\
&= \alpha_U + \alpha_\rho + \alpha_k - \alpha_{c_{v,a}} - \alpha_x = \alpha_\gamma + \alpha_U + \alpha_\rho + \alpha_k - \alpha_{c_{v,a}} - \alpha_x \\
&= \alpha_U + \alpha_p - \alpha_{c_{v,a}} - \alpha_x = \alpha_\gamma + \alpha_U + \alpha_p - \alpha_{c_{v,a}} - \alpha_x.
\end{aligned}$$

T is an independent parameter meaning that α_T is user defined (its choice is flexible). Since $\alpha_k = 2\alpha_x - 2\alpha_t$ (Section 3.2.2) and $\alpha_\gamma = 0$, as γ is a dimensionless parameter, $\alpha_{c_{v,w}}$ and $\alpha_{c_{v,a}}$ can be written in terms of α_x, α_t and α_T:

$$\begin{aligned}
\alpha_\rho + \alpha_T - \alpha_t &= \alpha_\gamma + \alpha_\rho + \alpha_k - \alpha_{c_{v,w}} - \alpha_t \qquad (3.65) \\
\Rightarrow \alpha_{c_{v,w}} &= \alpha_k - \alpha_T \Rightarrow \alpha_{c_{v,w}} = 2\alpha_x - 2\alpha_t - \alpha_T
\end{aligned}$$

and

$$\begin{aligned}
\alpha_\rho + \alpha_T - \alpha_t &= \alpha_\gamma + \alpha_\rho + \alpha_k - \alpha_{c_{v,a}} - \alpha_t \qquad (3.66) \\
\Rightarrow \alpha_{c_{v,a}} &= \alpha_k - \alpha_T \Rightarrow \alpha_{c_{v,a}} = 2\alpha_x - 2\alpha_t - \alpha_T.
\end{aligned}$$

Hence, $\alpha_{c_{v,w}} = \alpha_{c_{v,a}} = \alpha_{c_v}$. Herein, α_{c_v} is the unique exponent for both α_{c_w} and α_{c_a}. Eq. (3.49) is transformed as follows:

$$\beta^{\alpha_\rho} \rho_a^* = \beta^{\alpha_p - \alpha_R - \alpha_T} \frac{p^*}{R^* T^*}, \qquad (3.67)$$

leading to

$$\alpha_\rho = \alpha_p - \alpha_R - \alpha_T. \tag{3.68}$$

As $\alpha_p = 2\alpha_x - 2\alpha_t + \alpha_\rho$ (Eq. 3.58) the scaling exponent of R is obtained from Eq. (3.68) as

$$\alpha_R = 2\alpha_x - 2\alpha_t - \alpha_T. \tag{3.69}$$

The Lie group transformations of Eq. (3.50) yield

$$\alpha_R = \alpha_{R_u} - \alpha_{M_m}, \tag{3.70}$$

where α_{R_u} (the scaling exponent of R_u) is also derived from Eq. (3.51) written as

$$R_u = \frac{pV}{nT}. \tag{3.71}$$

The Lie group transformations of Eq. (3.71) yield the following equation in the transformed domain:

$$\beta^{\alpha_{R_u}} R_u = \beta^{\alpha_p + \alpha_V - \alpha_n - \alpha_T} \frac{pV}{nT}, \tag{3.72}$$

leading to

$$\alpha_{R_u} = \alpha_p + \alpha_V - \alpha_n - \alpha_T. \tag{3.73}$$

α_{M_m} is obtained by combining Eq. (3.70) with Eqs. (3.73) and (3.58) and

considering the dimension of V such that $\alpha_V = 3\alpha_x$:

$$\alpha_{M_m} = 2\alpha_x - 2\alpha_t + \alpha_\rho + 3\alpha_x - \alpha_n - \alpha_T - 2\alpha_x + 2\alpha_t + \alpha_T \qquad (3.74)$$
$$\Rightarrow \quad \alpha_{M_m} = 3\alpha_x + \alpha_\rho - \alpha_n,$$

where α_n is user defined because n is an independent parameter.

The scaling conditions for compressible flows are summarised in the second column of Table 3.2. They are consistent with those reported in Table 3.1, with additional restrictions for T, R, $c_{v,w}$, $c_{v,a}$ and M_m. All the exponents are written in terms of the five independent scaling exponents α_x, α_t, α_ρ, α_T and α_n. It is possible to assign the value of one of the independent scaling exponents and still preserve self-similarity. For example, in the fourth column of Table 3.1, the scaling conditions in terms of α_x, α_ρ, $\alpha_g = \alpha_R = 0$ and α_n are presented, where $\alpha_t = 0.5\alpha_x$.

Table 3.2: NSLs for the parameters of the governing equations for air-water flows including compressibility and heat transfer.

Parameters	**Written in terms of** α_x, α_t, α_ρ, α_T **and** α_n		**Written in terms of** α_x, α_ρ, $\alpha_g = \alpha_R = 0$ **and** α_n		**Written in terms of** α_x, $\alpha_R = \alpha_T = \alpha_{M_m} = 0$ **and** $\alpha_n = 3\alpha_x$	
	Exponents	**Scaling ratios**	**Exponents**	**Scaling ratios**	**Exponents**	**Scaling ratios**
x_i (m)	α_x	β^{α_x}	α_x	β^{α_x}	α_x	β^{α_x}
t (s)	α_t	β^{α_t}	$\alpha_t = 0.5\alpha_x$	$\beta^{0.5\alpha_x}$	$\alpha_t = \alpha_x$	β^{α_x}
ρ (kg m^{-3})	α_ρ	β^{α_ρ}	α_ρ	β^{α_ρ}	$\alpha_\rho = 0$	$\beta^0 = 1$
T (K)	α_T	β^{α_T}	$\alpha_T = \alpha_x$	β^{α_x}	$\alpha_T = 0$	$\beta^0 = 1$
n (mol)	α_n	β^{α_n}	α_n	β^{α_n}	$\alpha_n = 3\alpha_x$	$\beta^{3\alpha_x}$
U_i (m s^{-1})	$\alpha_U = \alpha_x - \alpha_t$	$\beta^{\alpha_x - \alpha_t}$	$\alpha_U = 0.5\alpha_x$	$\beta^{0.5\alpha_x}$	$\alpha_U = 0$	$\beta^0 = 1$
p (Pa)	$\alpha_p = 2\alpha_x - 2\alpha_t + \alpha_\rho$	$\beta^{2\alpha_x - 2\alpha_t + \alpha_\rho}$	$\alpha_p = \alpha_x + \alpha_\rho$	$\beta^{\alpha_x + \alpha_\rho}$	$\alpha_p = 0$	$\beta^0 = 1$
g_i (m s^{-2})	$\alpha_g = \alpha_x - 2\alpha_t$	$\beta^{\alpha_x - 2\alpha_t}$	$\alpha_g = 0$	$\beta^0 = 1$	$\alpha_g = -\alpha_x$	$\beta^{-\alpha_x}$
ν (m^2 s^{-1})	$\alpha_\nu = 2\alpha_x - \alpha_t$	$\beta^{2\alpha_x - \alpha_t}$	$\alpha_\nu = 1.5\alpha_x$	$\beta^{1.5\alpha_x}$	$\alpha_\nu = \alpha_x$	β^{α_x}
μ (kg m^{-1} s^{-1})	$\alpha_\mu = 2\alpha_x + \alpha_\rho - \alpha_t$	$\beta^{2\alpha_x + \alpha_\rho - \alpha_t}$	$\alpha_\mu = 1.5\alpha_x + \alpha_\rho$	$\beta^{1.5\alpha_x + \alpha_\rho}$	$\alpha_\mu = \alpha_x$	β^{α_x}
σ (N m^{-1})	$\alpha_\sigma = 3\alpha_x - 2\alpha_t + \alpha_\rho$	$\beta^{3\alpha_x - 2\alpha_t + \alpha_\rho}$	$\alpha_\sigma = 2\alpha_x + \alpha_\rho$	$\beta^{2\alpha_x + \alpha_\rho}$	$\alpha_\sigma = \alpha_x$	β^{α_x}
κ (m^{-1})	$\alpha_\kappa = \alpha_x^{-1}$	$\beta^{\alpha_x^{-1}}$	$\alpha_\kappa = \alpha_x^{-1}$	$\beta^{\alpha_x^{-1}}$	$\alpha_\kappa = \alpha_x^{-1}$	$\beta^{\alpha_x^{-1}}$
ν_t (m^2 s^{-1})	$\alpha_{\nu_t} = 2\alpha_x - \alpha_t$	$\beta^{2\alpha_x - \alpha_t}$	$\alpha_{\nu_t} = 1.5\alpha_x$	$\beta^{1.5\alpha_x}$	$\alpha_{\nu_t} = \alpha_x$	β^{α_x}
$\overline{u_\mathrm{i}u_\mathrm{i}}$ (m^2 s^{-2})	$\alpha_{\overline{uu}} = 2\alpha_x - 2\alpha_t$	$\beta^{2\alpha_x - 2\alpha_t}$	$\alpha_{\overline{uu}} = \alpha_x$	β^{α_x}	$\alpha_{\overline{uu}} = 0$	$\beta^0 = 1$
k (m^2 s^{-2})	$\alpha_k = 2\alpha_x - 2\alpha_t$	$\beta^{2\alpha_x - 2\alpha_t}$	$\alpha_k = \alpha_x$	β^{α_x}	$\alpha_k = 0$	$\beta^0 = 1$
ϵ (m^2 s^{-3})	$\alpha_\epsilon = 2\alpha_x - 3\alpha_t$	$\beta^{2\alpha_x - 3\alpha_t}$	$\alpha_\epsilon = 0.5\alpha_x$	$\beta^{0.5\alpha_x}$	$\alpha_\epsilon = -\alpha_x$	$\beta^{-\alpha_x}$
P_k (m^2 s^{-3})	$\alpha_{P_k} = 2\alpha_x - 3\alpha_t$	$\beta^{2\alpha_x - 3\alpha_t}$	$\alpha_{P_k} = 0.5\alpha_x$	$\beta^{0.5\alpha_x}$	$\alpha_{P_k} = -\alpha_x$	$\beta^{-\alpha_x}$
R (m^2 K^{-1} s^{-2})	$\alpha_R = 2\alpha_x - 2\alpha_t - \alpha_T$	$\beta^{2\alpha_x - 2\alpha_t - \alpha_T}$	$\alpha_R = 0$	$\beta^0 = 1$	$\alpha_R = 0$	$\beta^0 = 1$
c_v (m^2 K^{-1} s^{-2})	$\alpha_{c_v} = 2\alpha_x - 2\alpha_t - \alpha_T$	$\beta^{2\alpha_x - 2\alpha_t - \alpha_T}$	$\alpha_{c_v} = 0$	$\beta^0 = 1$	$\alpha_{c_v} = 0$	$\beta^0 = 1$
M_m (kg mol^{-1})	$\alpha_{M_m} = 3\alpha_x + \alpha_\rho - \alpha_n$	$\beta^{3\alpha_x + \alpha_\rho - \alpha_n}$	$\alpha_{M_m} = 3\alpha_x + \alpha_\rho - \alpha_n$	$\beta^{3\alpha_x + \alpha_\rho - \alpha_n}$	$\alpha_{M_m} = 0$	$\beta^0 = 1$

Some restrictions have to be introduced to avoid some inconsistencies, when

the ideal gas is intended to be used also in the scaled model. First, R must be invariant between the model and its prototype to preserve the ideal gas behaviour. This leads to the assumption $\alpha_R = 0$ and from Eq. (3.69), which implies

$$\alpha_T = 2\alpha_x - 2\alpha_t. \tag{3.75}$$

Combining this condition with Eqs. (3.65) and (3.66) leads to $\alpha_{c_v} = 0$ and $c_{v,a}$ and $c_{v,w}$ being invariant between the prototype and its model.

Since R_u is the universal gas constant, it is invariant between the model and its prototype and its scaling exponent is $\alpha_{Ru} = 0$. Since $\alpha_R = 0$, Eq. (3.70) yields

$$\alpha_{M_m} = 0. \tag{3.76}$$

Furthermore, the molar density M_c, representing the number of moles of a molecule present in a unit volume, is defined as:

$$M_c = n/V. \tag{3.77}$$

The application of the Lie group transformations to Eq. (3.77) leads to $\alpha_{M_c} = \alpha_n - \alpha_V$. In order to preserve the perfect gas hypothesis both in the model and its prototype, M_c must be invariant. Indeed, if M_c increases, also the interaction among the molecules increases and the perfect gas hypothesis might not hold. Hence, by keeping M_c invariant

$$\alpha_{M_c} = \alpha_n - \alpha_V = 0 \quad \Rightarrow \quad \alpha_n = \alpha_V \quad \Rightarrow \quad \alpha_n = 3\alpha_x. \tag{3.78}$$

The combination of Eq. (3.78) with Eqs. (3.74) and (3.76) leads to $\alpha_\rho = 0$.

Therefore, Eqs. (3.59), (3.58) and (3.61) reduce to

$$\alpha_\mu = 2\alpha_x - \alpha_t, \tag{3.79}$$

$$\alpha_p = 2\alpha_x - 2\alpha_t \tag{3.80}$$

and

$$\alpha_\sigma = 3\alpha_x - 2\alpha_t. \tag{3.81}$$

Hence, to preserve the perfect gas behaviour in the model, ρ, M_w and R must be kept invariant.

Another restriction is related to passages of states. If g_i is kept invariant, $\alpha_t = 0.5\alpha_x$ and, from Eq. (3.75), $\alpha_T = \alpha_x$. For example, if $\lambda = 2$ and $\beta = 1$, $\beta^{\alpha_x} = 2$ and $\beta^{\alpha_T} = \beta^{\alpha_x} = 2$ (third column of Table 3.1). Hence, assuming that the initial temperature T_0 of the prototype is at room temperature (293 K), the corresponding temperature of the model should be 146.5 K, which is below the freezing point. This drastic change of the initial temperature between the model and prototype suggests that it is convenient to keep T invariant. From Eq. (3.75), it follows:

$$\alpha_T = 2\alpha_x - 2\alpha_t = 0 \quad \Rightarrow \quad \alpha_t = \alpha_x. \tag{3.82}$$

However, this condition is inconsistent with $\alpha_g = 0$ that imposes $\alpha_t = 0.5\alpha_x$ (fourth column of Table 3.2). Hence, it is impossible to keep g_i, R and T invariant under the same scaling conditions. The solution is to apply Eq. (3.82) to $\alpha_g = \alpha_x - 2\alpha_t$ (second column of Table 3.2),

$$\alpha_g = -\alpha_x. \tag{3.83}$$

In other words, by keeping R and T invariant, g must be increased in the model with respect to the prototype. The scaling configuration that preserves the ideal gas behaviour and avoids a reduction of T in the scaled model is written in terms of α_x, $\alpha_R = \alpha_T = \alpha_{M_m} = 0$ and $\alpha_n = 3\alpha_x$ in the sixth column of Table 3.2. This means that length is an independent parameters and R, T, M_m and n are fixed.

3.4 Numerical solvers used

In this work, the NSLs are tested by using CFD simulations of three test cases run on the University of Nottingham high performance computing (HPC). The discretisation of the governing equations is done with the finite volume method (FVM). This is a numerical technique used to solve partial differential equations, particularly those arising in fluid mechanics and heat transfer (Ashgriz and Mostaghimi, 2002; Chung, 2002). The method divides the domain into a finite number of control volumes called cells, each of which is treated as a discrete system. The equations governing the behavior of the system are integrated over each cell, resulting in a set of algebraic equations that can be solved numerically.

The FVM is a conservative method, meaning that it conserves mass, momentum and energy within each control volume. It is also flexible, as it can handle irregular geometries and non-uniform grid spacing. The FVM is an approximation because it involves discretising the domain into a finite number of control volumes and approximating the values of the variables within each control volume using numerical methods. This means that the FVM produces an approximate solution to the continuum problem being studied, rather than an exact solution (Ashgriz and Mostaghimi, 2002;

Chung, 2002).

In order to model air-water flows, *interFoam* solves the system of governing equations presented in Section 3.2.1, while *compressibleInterIsoFoam* the ones in Section 3.3.1. Both solvers are based on the volume of fluid (VOF) method, meaning that they solve the governing equations with the pressure and velocity fields shared among two phases, e.g. air and water. The interface between water and air is identified by a value of the phase fraction γ between $\gamma = 1$ (water) and $\gamma = 0$ (air). The fluid properties used in the equations are mapped in all domains as a weighted average using γ as weight, e.g. for ρ and ν:

$$\rho = \gamma\rho_w + (1-\gamma)\rho_a \tag{3.84}$$

and

$$\nu = \gamma\nu_w + (1-\gamma)\nu_a. \tag{3.85}$$

σ appears in Eq. (3.3) to model the surface tension force per unit volume, as stated in the Continuum Surface Force method proposed by Brackbill et al. (1992). The curvature of the interface between two fluids κ is defined as

$$\kappa = -\frac{\partial}{\partial x_{\mathrm{i}}}\left(\frac{\partial\gamma/\partial x_{\mathrm{i}}}{\mid \partial\gamma/\partial x_{\mathrm{i}} \mid}\right). \tag{3.86}$$

γ is transported as a scalar by the flow field and the interface location (e.g. the free surface) is updated by solving the volume fraction equation

$$\frac{\partial\gamma}{\partial t} + \frac{\partial(\gamma U_{\mathrm{j}})}{\partial x_{\mathrm{j}}} = 0. \tag{3.87}$$

After identifying the cells containing the free surface, the challenge lies in computing how those cells are cut by the free surface, thus an interface reconstruction technique, usually called interface scheme, is needed. The interface scheme used by *interFoam* is the Multidimensional Universal Limited Explicit Solver (MULES). The advection term of Eq. (3.3) is modified to reduce the smearing of the free surface (Deshpande et al., 2012). Instead, *compressibleInterIsoFoam* uses a numerical scheme called *isoAdvector* based on iso-surfaces, a set of points having the same value of γ and cutting the cells with the free surface (Roenby et al., 2016). The cells containing the free-surface are divided in two sub-cells of the volumetric proportions dictated by γ. Roenby et al. (2016) showed that *isoAdvector* reduces the limitation of MULES, which introduces some spurious velocities to keep the interface sharp. In Appendix A, *isoAdvector* is used to simulate the dam break case in the same conditions used with MULES and it is shown that the test of the derived scaling laws does not depend on the interface scheme, because this does not introduce additional parameters in the process, in addition to the ones appearing in the governing equations, leaving scaling relationships unaffected.

3.5 Summary

Lie group transformations were applied to the Reynolds-averaged Navier–Stokes equations where surface tension effects were included as a source term. This allows the modelling of hydrodynamic phenomena at small scale taking into account the viscous and surface tension effects. These NSLs are more universal and flexible than the Froude scaling laws because different scaling configurations can be obtained, e.g. by also scaling the density of the fluid. Further, the Froude scaling laws are a particular configuration of the NSLs

written in terms of the scaling exponent of the length α_x, the density $\alpha_\rho = 0$ and the gravitational acceleration $\alpha_g = 0$.

Lie group transformations were also applied to the system of governing equations of compressible air-water flows to derive NSLs, allowing the modelling of hydrodynamic phenomena at small scales without viscous, surface tension, compressibility and heat exchange scale effects. Since the temperature cannot be reduced below the freezing point and the molar mass, as well as the molar density, need to be the same, some restrictions on the scaling exponents are taken into account. Hence, the scaling configuration used in this work is expressed as a function of the scaling exponents of the length α_x, the specific gas constant α_R, the temperature α_T, the molar mass α_M and the number of moles α_n.

The compressible scaling laws are as the same as the incompressible ones with additional terms such as T, R, M_m and c_v included. These terms are those from the self similarity of Eqs. (3.63) and (3.49). The main difference arises when restrictions need to be applied. Indeed, the fact that R and T need to be invariant implies that $\alpha_g = -\alpha_x$ and therefore the configurations are completely different with respect to the one used in the incompressible case where $\alpha_g = 0$. Nevertheless, it is possible to derive a configuration for the incompressible case in terms of α_x, $\alpha_g = -\alpha_x$ and $\alpha_\rho = 1$. This is the same configuration as reported in the sixth and seventh columns in Table 3.2 but without the thermophysical parameters. This Chapter 3 concludes with some descriptions of the used numerical solvers in OpenFOAM.

Chapter 4

Testing the NSLs

4.1 Introduction

In this section, the novel scaling laws are tested by using numerical simulations. The scaling laws for incompressible air-water flows are tested by using *interFoam*. Two test cases are simulated, namely (a) a dam break flow interacting with an obstacle and (b) a vertical circular plunging water jet impinging on quiescent water (Catucci et al., 2021). The dam break simulations are labelled with D1 (the prototype), D8 ($\lambda = 8$) and D16 ($\lambda = 16$) while the plunging water jet P1 (the prototype), P8 ($\lambda = 8$) and P16 ($\lambda = 16$). The prototypes of both phenomena are also scaled by using the TFs, creating $D8_{TFs}$ and $D16_{TFs}$ (for the dam break flow) and $P8_{TFs}$ and $P16_{TFs}$ (for the plunging water jet). By applying the PFs, $D8_{PFs}$ and $D16_{PFs}$ (for the dam break flow) and $P8_{PFs}$ and $P16_{PFs}$ (for the plunging water jet) are created.

The NSLs where the air is considered compressible are validated by using *compressibleInterIsoFoam*. The test cases are (i) the same dam break flow

used for the incompressible case and (ii) a Taylor bubble. In this case the simulation of the dam break flows are CD1 (prototype), CD8 ($\lambda = 8$) and CD16 ($\lambda = 16$), while for the Taylor bubble T1 (prototype) T4 ($\lambda = 4$), T8 ($\lambda = 8$) and T16 ($\lambda = 16$). The application of the TFs leads to $CD8_{TFs}$ and $CD16_{TFs}$ (for the dam break flow) and $T4_{TFs}$, $T8_{TFs}$ and $T16_{TFs}$ (for the Taylor bubble). For compressible air-water flows, the PFs were not applied because there is no indication on how to scale the thermophysical properties.

Table 4.1: Summary of the simulations carried out to validate NSLs.

		Dam break flow	**Water plunging jet**	**Taylor bubble**
Incompressible air-water flows (*interFoam*)	Prototype	D1	P1	-
	NSLs	D8 ($\lambda = 8$) and D16 ($\lambda = 16$)	P8 ($\lambda = 8$) and P16 ($\lambda = 16$)	-
	TFs	$D8_{TFs}$ ($\lambda = 8$) and $D16_{TFs}$ ($\lambda = 16$)	$P8_{TFs}$ ($\lambda = 8$) and $P16_{TFs}$ ($\lambda = 16$)	-
	PFs	$D8_{PFs}$ ($\lambda = 8$) and $D16_{PFs}$ ($\lambda = 16$)	$P8_{PFs}$ ($\lambda = 8$) and $P16_{PFs}$ ($\lambda = 16$)	-
Compressible air-water flows (*compressibleInterIsoFoam*)	Prototype	DC1	-	T1
	NSLs	DC8 ($\lambda = 8$) and DC16 ($\lambda = 16$)	-	T4 ($\lambda = 4$), T8 ($\lambda = 8$) and T16 ($\lambda = 16$)
	TFs	$DC8_{TFs}$ ($\lambda = 8$) and $DC16_{TFs}$ ($\lambda = 16$)	-	$T4_{TFs}$ ($\lambda = 4$), $T8_{TFs}$ ($\lambda = 8$) and $T16_{TFs}$ ($\lambda = 16$)

4.2 Incompressible air-water flows test cases

Most of the results presenting in this Section 4.2 have previously been published in Catucci et al. (2021).

4.2.1 Dam break flow

Dam break flows have been widely investigated numerically and the specific case addressed herein is chosen because it is a well-known test to validate the modelling of large deformations of free surfaces (Issakhov et al., 2018;

Kleefsman et al., 2005; Zhainakov and Kurbanaliev, 2013). In this work, $\gamma = 0.1$ is selected to identify the air-water interface in the VOF method. This value is obtained by considering the value between 0 and 1 providing the best fit with the experimental void fraction distribution.

Numerical set-up for the dam break flow

The setup and the mesh described in this section are also used for testing the NSLs where the air is considered compressible (Section 4.3.1). aThe initial condition at $t = 0$ consisted of a quiescent water column of volume 1.228 (length) $\times$ 0.550 (width) $\times$ 1.000 (height) m^3, located at the left side of a 3.220 m $\times$ 1.000 m $\times$ 1.000 m tank (Figure 4.1). A prismatic fixed obstacle with a volume of $0.160 \times 0.160 \times 0.403$ m^3 was located at $x_1 = 2.395$ m. The water column was released instantaneously at $t = 0$ s. Subsequently, the flow impacted the obstacle and created a complex two-phase flow. The top wall of the domain was modelled as an open, fully transmissive boundary at atmospheric pressure and all the remaining walls as no-slip boundary conditions. The water density was $\rho_w = 1000$ kg m^{-3}, its kinematic viscosity $\nu_w = 1 \times 10^{-6}$ m^2 s^{-1} and the surface tension constant $\sigma = 0.07$ N m^{-1}.

A 180 (length) $\times$ 60 (width) $\times$ 80 (height) Cartesian computational grid was used, apart from the obstacle, following Zhainakov and Kurbanaliev (2013). Note that, due to the orientation of the reference frame, for this case $g_\mathrm{i} = (0, 0, -g)$ in Eq. (3.2). The time step Δt was set equal to 0.001 s at the start of the simulation and it was varied subsequently by respecting the CFL condition

$$\frac{U_\mathrm{j} \Delta t}{\Delta x_\mathrm{j}} < C_{max}, \tag{4.1}$$

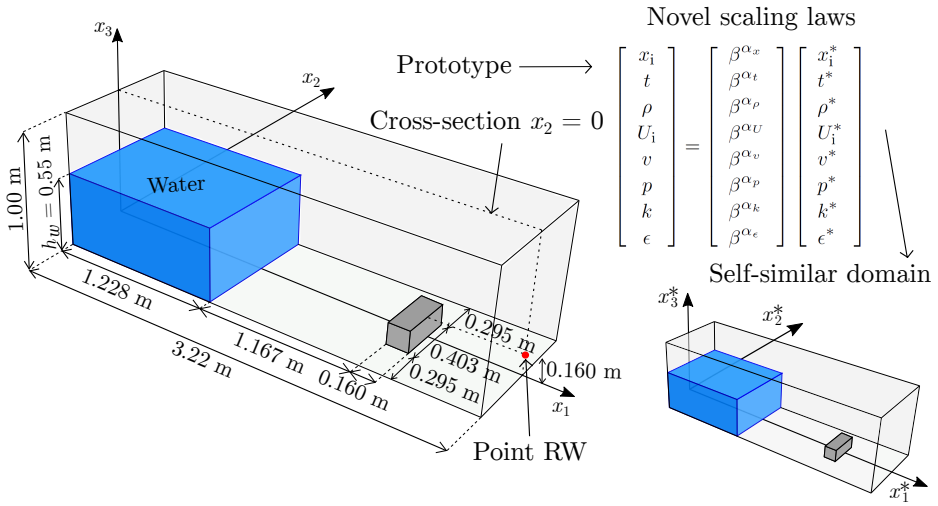


Figure 4.1: Initial set-up of the dam break flow prototype and a scaled numerical domain to schematically illustrate the NSLs (Catucci et al., 2021).

where Δx_i is the mesh size in the Cartesian coordinate system and $C_{max} = 0.8$ the maximum Courant number following Courant et al. (1967).

The number of cells in the computational domain was 861075 and the used cores and memory were 4 and 36 GB, respectively. It required 2 h to simulate the real time of $t_f = 6$ s (also for the corresponding times at reduced scales). In this test case, as well as for the jet, all the dimensional parameters, including the mesh sizes and time steps, were scaled to the smaller domains according to the selected scaling laws. The schemes used for each variables are summarised in Table 4.2 and they are invariant trough the scales.

Table 4.2: Numerical schemes for the dam break simulations.

ddtSchemes	Euler
gradSchemes	Gauss linear
divSchemes	
div(rhoPhi,U)	Gauss upwind
div(phi,alpha)	Gauss vanLeer
div(phi,p)	Gauss upwind
div(phi,k)	Gauss upwind
div(phi,epsilon)	Gauss upwind
laplacianSchemes	Gauss linear corrected

Application of the NSLs for incompressible air-water flows

Two self-similar domains, namely D8 and D16, were created with factors of $\lambda = \beta^{\alpha_x} = 8$ and 16, respectively. To achieve this, it was assumed that $\alpha_x = 1$ such that $\beta = 8$ (D8) and 16 (D16), respectively. All variables and parameters were transformed with the scaling exponents in the fourth and fifth columns of Table 3.1 (NSLs written in terms of α_x, α_t and $\alpha_g = 0$). Their specific values for the prototype and the scaled models, obtained by applying the conditions in Table 4.3, are presented in Table 4.4. The prototype was also scaled by using PFs ($D8_{\text{PFs}}$ and $D16_{\text{PFs}}$) and TFs ($D8_{\text{TFs}}$ and $D16_{\text{TFs}}$) using the same λ as in the self-similar domains. It is worth noting that by following the scaling conditions in Table 4.3, F, R and W remain invariant.

Table 4.3: Scaling parameters and exponents used to scale the dam break flow prototype values to the corresponding values in the domains D8 and D16 using the NSLs (Catucci et al., 2021).

	Domain D8	**Domain D16**
Scaling parameter β	8	16
Scaling exponents		
Length (m) α_x	1	1
Time (s) α_t	0.5	0.5
Density (kg m^{-3}) α_ρ	1	1
Velocity (m s^{-1}) α_U	0.5	0.5
Pressure (Pa) α_p	2	2
Viscosity (m^2 s^{-1}) α_ν	1.5	1.5
Surface tension (N m^{-1}) α_σ	3	3
Scaling ratios		
Length (m) β^{α_x}	8	16
Time (s) β^{α_t}	2.82	4
Density (kg m^{-3}) β^{α_ρ}	8	16
Velocity (m s^{-1}) β^{α_U}	2.82	4
Pressure (Pa) $\beta\alpha_p$	64	256
Viscosity (m^2 s^{-1}) β^{α_ν}	22.62	64
Surface tension (N m^{-1}) β^{α_σ}	512	4096

It is worth noting that NSLs the dimensionless numbers are the same as well as in the PFs that is a particular configuration of the NSLs . For example, W for D1, $D8_{PFs}$ and $D16_{PFs}$ is 2.73×10^3.

Table 4.4: Parameters for the dam break flow in the prototype and the scaled domains.

Parameters	**Prototype D1**	**Domain D8**	**Domain D16**	**Domain $D8_{PFs}$**	**Domain $D16_{PFs}$**	**Domain $D8_{TFs}$**	**Domain $D16_{TFs}$**
h_w (m)	0.55	0.06875	0.034375	0.06875	0.034375	0.06875	0.034375
t_f (s)	6	2.12	1.5	2.12	1.5	2.12	1.5
g (m s^{-2})	9.81	9.81	9.81	9.81	9.81	9.81	9.81
ρ_w (kg m^{-3})	1000	125	62.5	1000	1000	1000	1000
ν_w (m^2 s^{-1})	10^{-6}	4.42×10^{-8}	1.56×10^{-8}	4.42×10^{-8}	1.56×10^{-8}	10^{-6}	10^{-06}
ρ_a (kg m^{-3})	1	0.125	0.0625	1	1	1	1
ν_a (m^2 s^{-1})	1.48×10^{-5}	6.54×10^{-7}	2.31×10^{-7}	6.54×10^{-7}	2.31×10^{-7}	1.48×10^{-5}	1.48×10^{-5}
σ (N m^{-1})	0.07	1.37×10^{-4}	1.70×10^{-5}	1.09×10^{-3}	2.73×10^{-4}	0.07	0.07

Results for the incompressible-air dam break flow

For the purpose of this work it is interesting to analyse the stage of the flow when gravity, inertial, viscous and surface tension effects are all relevant. This happens when the dam break flow impacts the obstacle and creates an elongated water tongue. Figure 4.2 shows this process with snapshots of the prototype and the scaled domains at $x_2' = x_2/h_w = 0$ (Figure 4.1) and dimensionless time $t' = t\sqrt{g/h_w} = 2.7$. The contours in Figure 4.2 represent the dimensionless velocity magnitude $U' = U/\sqrt{gh_w}$, where $U = \sqrt{U_1^2 + U_2^2 + U_3^2}$.

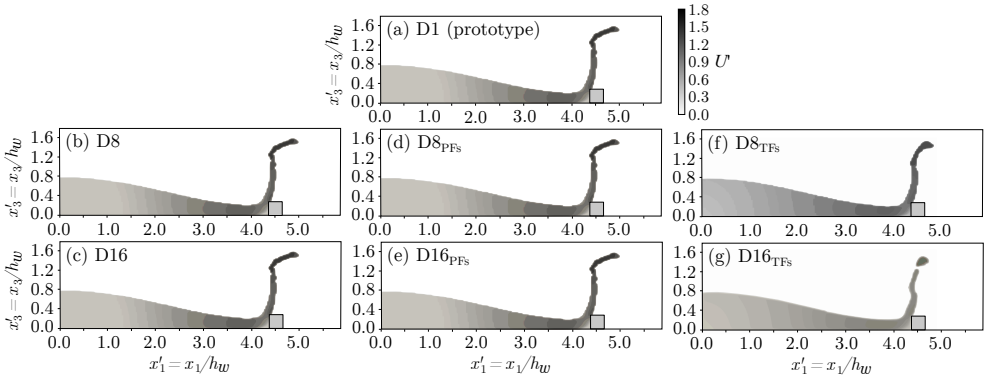


Figure 4.2: Snapshots of the incompressible-air dam break flow at the cross-section $x_2' = 0$ and dimensionless time $t' = 2.7$ of the (a) prototype and scaled with (b,c) the NSLs, (d,e) PFs and (f,g) TFs laws (Catucci et al., 2021).

The prototype shows a large free surface deformation after impacting the

obstacle (Figure 4.2a). The self-similar domains and the domains scaled with PFs all simulate the water tongue of the prototype correctly. Moreover, the dimensionless velocity magnitude in the prototype and in the self-similar domains are the same, despite of the increasing λ (Figure 4.2b,c,d,e). On the other hand, the TFs laws do not model the free surface correctly due to R and W scale effects, i.e. the water tongue becomes less prolonged with increasing λ (Figure 4.2f,g).

The differences between the prototype and the scaled domains are quantified using the Root Mean Square Error along the plane $x_2' = 0$ for U' ($\mathrm{RMSE}_{U'}$)

$$\mathrm{RMSE}_{U'} = \sqrt{\frac{\sum_{\mathrm{b}=1}^{\mathrm{n}} (U'_{\mathrm{b},p} - U'_{\mathrm{b},m})^2}{\mathrm{n}}}, \tag{4.2}$$

where $U'_{\mathrm{b},p}$ are the cell values of U' in the prototype, $U'_{\mathrm{b},m}$ in the scaled domains and $\mathrm{n} = 14283$ is the number of cells in the cross-section $x_2' = 0$. As shown in Table 4.5, the $\mathrm{RMSE}_{U'}$ values for D8 and D16 confirm a nearly perfect self-similarity with respect to the prototype.

Table 4.5: $\mathrm{RMSE}_{U'}$ for the dam break flow for the domains D1 and D8, D16, $\mathrm{D8_{PFs}}$, $\mathrm{D16_{PFs}}$, $\mathrm{D8_{TFs}}$ and $\mathrm{D16_{TFs}}$, for the snapshots in Figure 4.2 (Catucci et al., 2021).

$\mathbf{RMSE}_{U'}$					
D1-D8	**D1-D16**	**D1-D8$_{\mathbf{PFs}}$**	**D1-D16$_{\mathbf{PFs}}$**	**D1-D8$_{\mathbf{TFs}}$**	**D1-D16$_{\mathbf{TFs}}$**
2.98×10^{-4}	2.10×10^{-4}	2.54×10^{-4}	2.29×10^{-4}	0.067	0.119

k is used to assess turbulence because it shows significant scale effects if ν is not scaled. Air entrainment is assessed by using γ, which is expected to deviate from the prototype if the surface tension is over-represented in the scaled domain. Figure 4.3 shows the dimensionless turbulent kinetic energy $k' = k/(gh_w)$ at point RW (Figure 4.1) versus t' and the variation of γ is

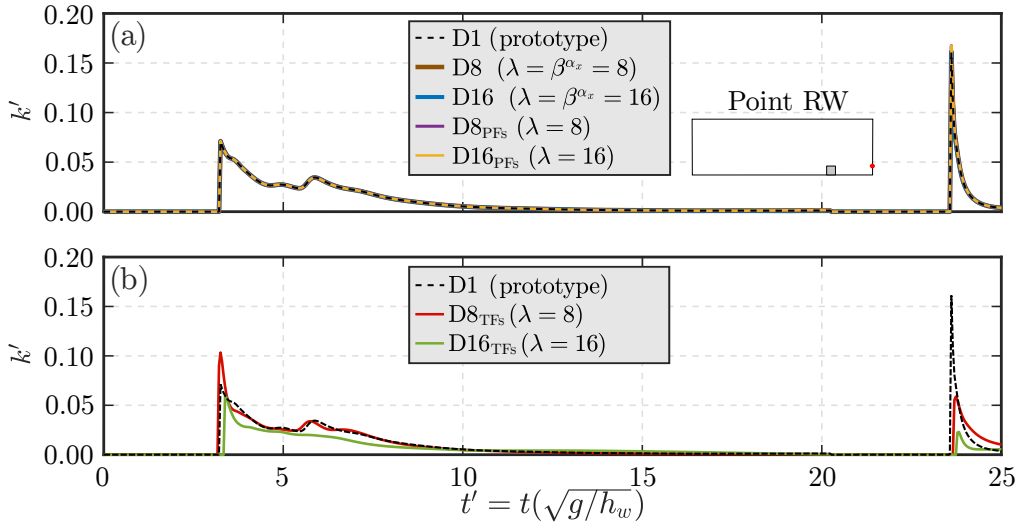


Figure 4.3: k' time histories in the dam break flow at point RW for (a) domains D1, D8, D16, $D8_{PFs}$ and $D16_{PFs}$ and (b) D1, $D8_{TFs}$ and $D16_{TFs}$ (after Catucci et al., 2021).

shown in Figure 4.4. After $t' = 2.7$, the water tongue collapses and creates a complex flow characterised by strong turbulence and air entrainment. The flow reaches the downstream wall where it is reflected at $t' = 3.25$. At a later stage, the dam-break wave is re-reflected at the upstream wall and it reaches point RW again at $t' = 23.6$.

The perfect collapse of the data for D1, D8 and D16 affirms the self-similar behaviour of k' for the NSLs. The self-similar behaviour is also confirmed for $D8_{PFs}$ and $D16_{PFs}$. On the other hand, k' shows scale effects using TFs; the first k' peak is either under- or over-estimated ($D8_{TFs}$ and $D16_{TFs}$, respectively), while the magnitude of the second peak decreases with increasing λ.

As demonstrated in Figure 4.4, where γ is shown as a proxy for surface tension, air entrainment is correctly modelled in the self-similar domains as it controls the air-water interface and the free surface curvature. While the results in the domains D1, D8, D16, $D8_{PFs}$ and $D16_{PFs}$ essentially collapse, the domains scaled with TFs show significant differences in the

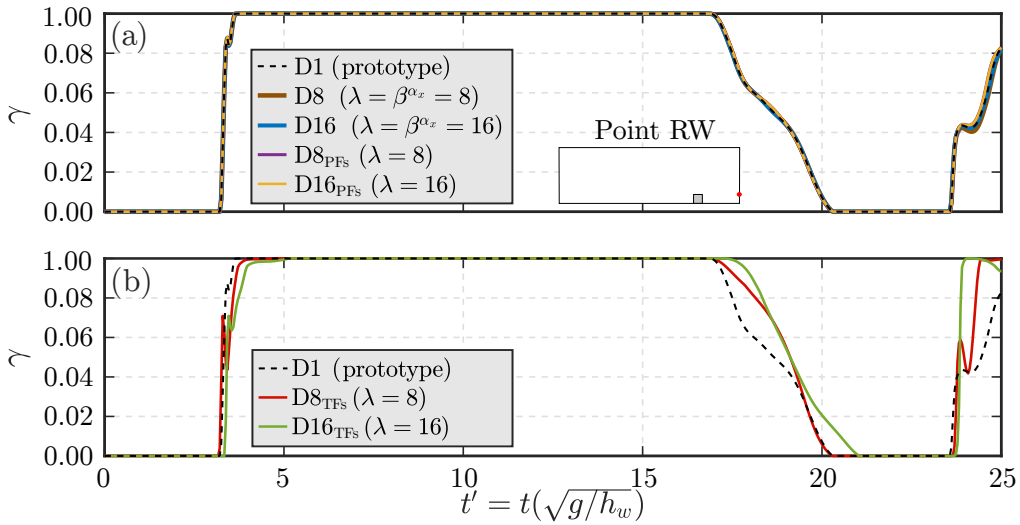


Figure 4.4: γ time histories in the dam break flow at point RW for (a) domains D1, D8, D16, $D8_{PFs}$ and $D16_{PFs}$ and (b) D1, $D8_{TFs}$ and $D16_{TFs}$ (after Catucci et al., 2021).

region where air entrainment is most important. γ starts to increase close to $t' = 4$, meaning that the wave reaches RW consistently at the same time in all domains except for $D8_{TFs}$ and $D16_{TFs}$ (Figure 4.4). Subsequently, γ increases to reach 1 less rapidly than in the prototype when using TFs. These differences become more visible at a later stage of the simulation when the dam break wave is re-reflected at $t' = 23.6$, showing significant scale effects.

Figure 4.5 shows the time history of a $p'_{rel} = (p - p_{atm})/(gh_w\rho_w)$ (where p_{atm} is the atmospheric pressure) at point UO located upstream the obstacle at $x'_3 = 0.145$ (in the prototype $x_3 = 0.08m$, see insert in Figure 4.5). The prototype and D8, D16, $D8_{PFs}$ and $D16_{PFs}$ show the same behaviour. The flow reaches the obstacle and the first pressure peak is shown at $t' = 2$. Around $t' = 5$, a small peak is observed concurrently with the entrapping of an air pocket between the falling water tongue and the obstacle. At this time, an air pocket is entrapped between the falling water tongue and the downstream side of the obstacle, as Figure 4.6 shows. The air pocket is compressed by water, but the air density inside remains the same

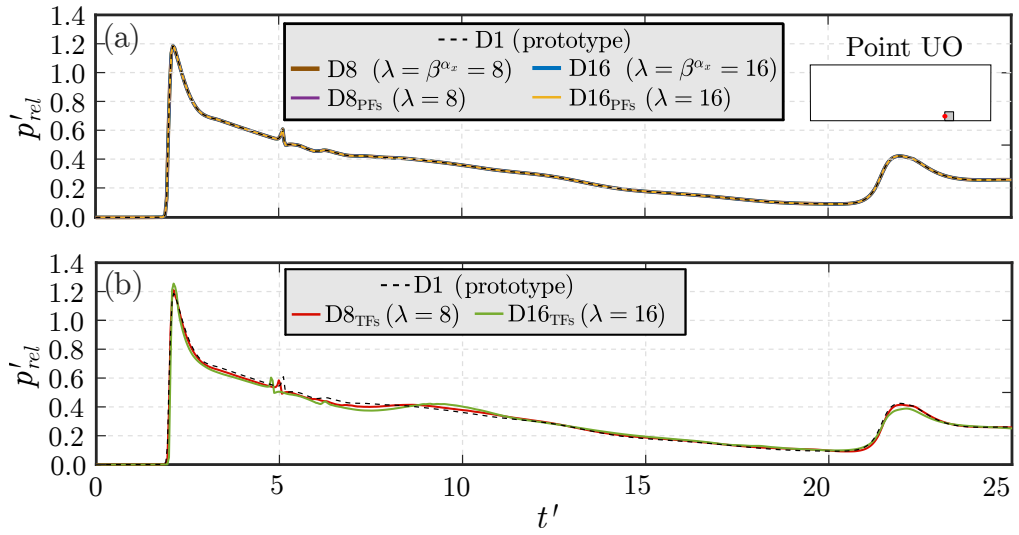


Figure 4.5: p'_{rel} time histories in the dam break flow at point UO for (a) domains D1, D8, D16, D8$_{\mathrm{PFs}}$ and D16$_{\mathrm{PFs}}$ and (b) D1, D8$_{\mathrm{TFs}}$ and D16$_{\mathrm{TFs}}$ (after Catucci et al., 2021).

because the solver does not calculate the air compressibility. When the compressibility of air is considered, the results of p'_{rel} show an oscillation that indicate the variation of the air density inside the pocket (see Section 4.3.1).

The self-similar behaviour of the D8, D16, D8$_{\mathrm{PFs}}$ and D16$_{\mathrm{PFs}}$ are confirmed by the fact that the dynamics of the flow is the same contrary to D8$_{\mathrm{TFs}}$ and D16$_{\mathrm{TFs}}$ that show some differences with respect to the prototype. The results of the TFs show some scale effects, e.g. dimension of the air pocket, even if the general behaviour is well reproduced with respect to the prototype.

4.2.2 Plunging water jet

In this section, the same scaling laws as in Section 4.2.1 are applied to the plunging water jet presented in Chanson et al. (2004). This involves free-surface instabilities, air entrainment and turbulence.

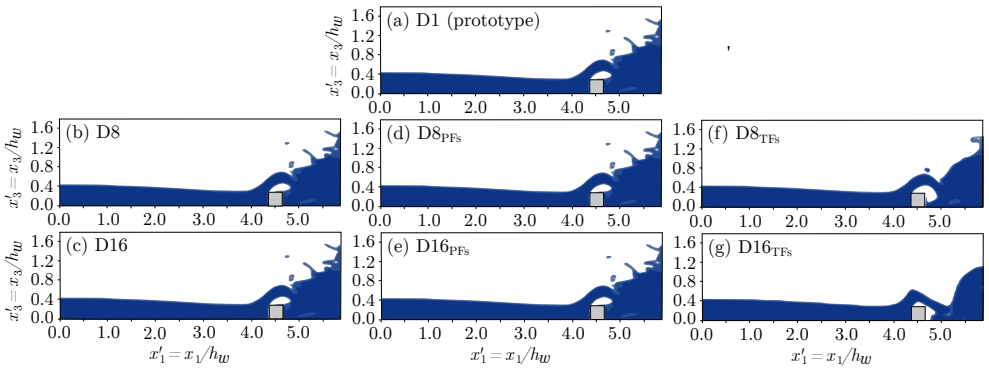


Figure 4.6: Snapshots of the incompressible-air dam break flow at the cross-section $x_2' = 0$ and dimensionless time $t' = 5$ of the (a) prototype and scaled with (b,c) the NSLs, (d,e) PFs and (f,g) TFs.

Numerical setup for the plunging water jet

The setup is based on the experiments of Chanson et al. (2004), consisting of a jet from a circular orifice impinging on a prismatic column of water. However, in this study, the symmetry of the problem with respect to two orthogonal vertical planes was used to simulate only a quarter of the domain, in order to reduce the computational cost. Figure 4.7 shows the numerical domain and the parameters used in the prototype. A plunging water jet was ejected from a nozzle having a radius $r_{in} = 0.0125$ m. Here, the subscript in (inlet) indicates the quantities at the nozzle, i.e. at the inlet of the numerical domain, while the subscript im (impact) indicates values of parameters at the still water level, i.e. $x_1 = 0$. The receiving pool was 0.15 m wide and 1.80 m deep and at the start of the simulation the distance between the water surface and the nozzle is $l_1 = 0.10$ m. The velocity of the jet at $x_1 = 0$ is $U_{im} = 4.10$ m/s. Here, a Cartesian coordinate system with x_1 pointing downwards was used, therefore, $g_\mathrm{i} = (g, 0, 0)$.

The inlet boundary condition, namely the nozzle, was at the top boundary. The velocity at the inlet U_{in} and both k_{in} and ϵ_{in} were prescribed, while the outlet was located at the bottom boundary, having the same flow rate

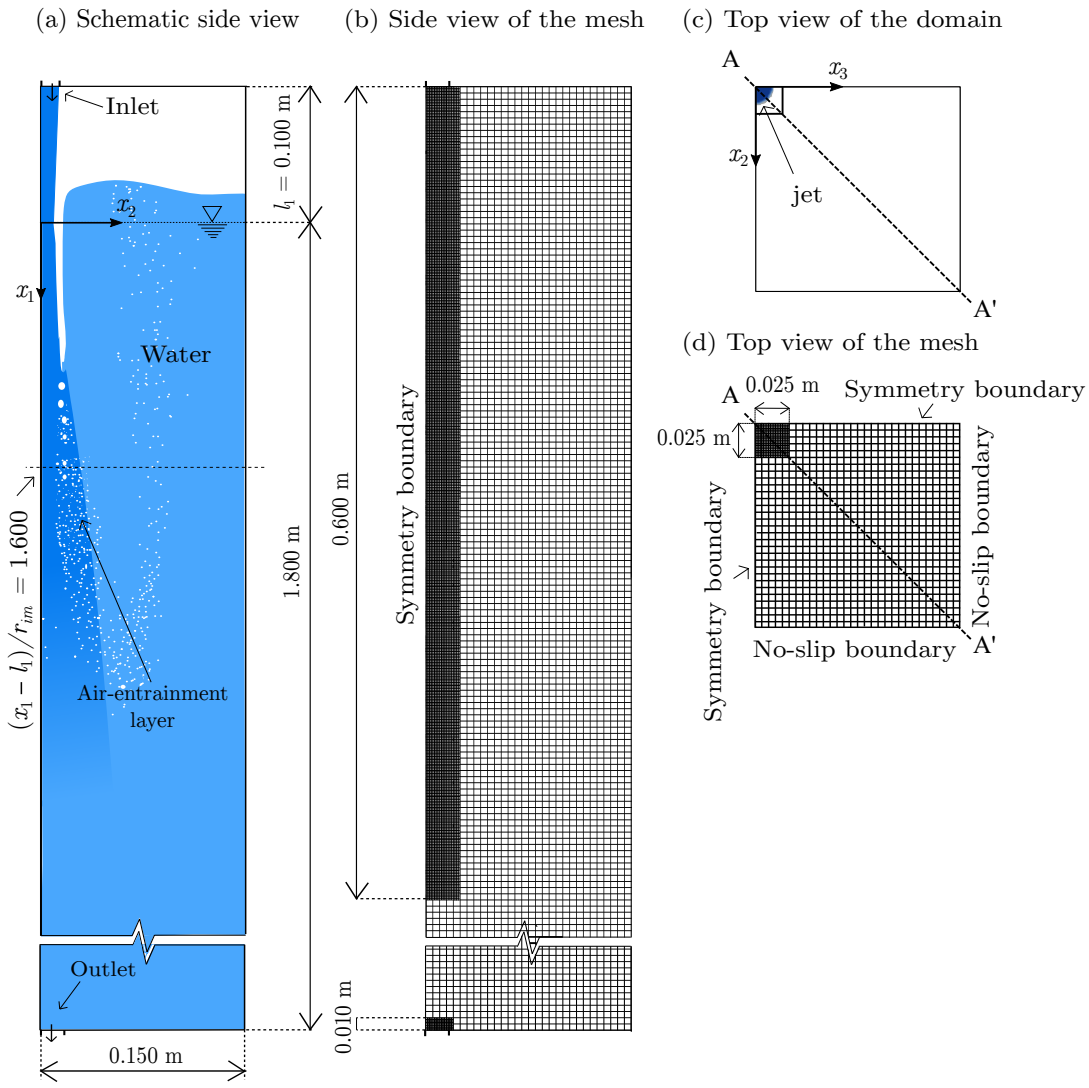


Figure 4.7: Schematic illustration of the computational domain and mesh of the plunging water jet (Catucci et al., 2021).

magnitude as the inlet.

U_{in} was calculated starting from the jet impact velocity using Bernoulli's theorem $U_{in} = \sqrt{U_{im}^2 - 2gl_1} = 3.85$ m s^{-1}. At the outlet (subscript *out*) $U_{out} = U_{in}$ and $r_{out} = r_{in}$. k_{in} and ϵ_{in} were calculated as

$$k_{in} = \frac{3}{2}(U_{in}I)^2 = 0.000471 \text{ m}^2 \text{ s}^{-2}, \tag{4.3}$$

$$\epsilon_{in} = C_\mu \frac{k_{in}^{3/2}}{l_t} = 0.00105 \text{ m}^2 \text{ s}^{-3}, \tag{4.4}$$

where $I = 0.46\%$ is the turbulent intensity following Chanson et al. (2004),

and l_t the turbulent mixing length approximated with $l_t = 0.07 r_{in}$. The part of the top boundary of the domain not occupied by the inlet was modelled as a fully transmissive open boundary at atmospheric pressure. Since only a quarter of the domain was simulated, a symmetry boundary condition was used at the symmetry boundary walls and no-slip conditions were applied at the remaining walls, including the bottom wall outside the outlet cells (Figure 4.7). The used numerical schemes for the plunging water jet are summarised in Table 4.6.

Table 4.6: Numerical schemes for the plunging jet case.

ddtSchemes	Euler
gradSchemes	Gauss linear
	divSchemes
div(rhoPhi,U)	Gauss linearUpwind grad (U)
div(phi,alpha)	Gauss vanLeer
div(phi,p)	Gauss upwind
div(phi,epsilon)	Gauss upwind
laplacianSchemes	Gauss linear corrected

Application of the NSLs for incompressible air-water flows

A structured orthogonal mesh was used with a finer resolution for the area in which the water jet impacted the free surface down to a depth of 0.6 m. The smallest observed bubble size was 1 mm and the minimum cell size 0.625 mm to increase the interface sharpness around the bubbles (Boualouache et al., 2018; Chanson et al., 2004). This mesh resolution is not fine enough to resolve the smallest bubbles present in the flow. However, the main focus of this work is to show the relative differences in the results of the application of different scaling laws for air-water flows, rather than to perfectly resolve the dynamics of individual bubbles.

Table 4.7: Scaling parameters and used exponents to scale the plunging jet prototype values to the corresponding values in the domains P8 and P16 (Catucci et al., 2021).

Parameters	**Prototype**	**Domain P8**	**Domain P16**	**Domain $\mathbf{P8_{PFs}}$**	**Domain $\mathbf{P16_{PFs}}$**	**Domain $\mathbf{P8_{TFs}}$**	**Domain $\mathbf{P16_{TFs}}$**
r_{in} (m)	0.0125	0.0015625	7.81×10^{-4}	0.0015625	7.81×10^{-4}	0.0015625	7.81×10^{-4}
t_f (s)	300	106	75	106	75	106	75
U_{im} (m s^{-1})	4.10	1.45	1.025	1.45	1.025	1.45	1.025
g (m s^{-2})	9.81	9.81	9.81	9.81	9.81	9.81	9.81
ρ_w (kg m^{-3})	1000	125	62.5	1000	1000	1000	1000
ν_w (m^2 s^{-1})	10^{-6}	4.42×10^{-8}	1.56×10^{-8}	4.42×10^{-8}	1.56×10^{-8}	10^{-6}	10^{-6}
ρ_a (kg m^{-3})	1	0.125	0.0625	1	1	1	1
ν_a (m^2 s^{-1})	1.48×10^{-5}	6.54×10^{-7}	2.31×10^{-7}	6.54×10^{-7}	2.31×10^{-7}	1.48×10^{-5}	1.48×10^{-5}
σ (N m^{-1})	0.07	1.37×10^{-4}	1.70×10^{-5}	0.001	2.73×10^{-4}	0.07	0.07
k_{in} (m^2 s^{-2})	4.71×10^{-4}	5.89×10^{-5}	2.94×10^{-5}	5.89×10^{-5}	2.94×10^{-5}	5.89×10^{-5}	2.94×10^{-5}
ϵ_{in} (m^2 s^{-3})	1.05×10^{-3}	3.72×10^{-4}	2.63×10^{-4}	3.72×10^{-4}	2.63×10^{-4}	3.72×10^{-4}	2.63×10^{-4}

Application of the NSLs for the plunging water jet

The two self-similar domains P8 and P16 were simulated with geometrical scale factors of $\lambda = 8$ and 16, respectively. Similarly to the dam break case, the scaling exponent for length is $\alpha_x = 1$ such that $\beta = 8$ (P8) and 16 (P16). The scaling ratios and parameters obtained by applying the conditions in the second column of Table 3.1 are shown in Table 4.7. The domains $\mathrm{P8_{PFs}}$ and $\mathrm{P16_{PFs}}$ refer to the PFs and $\mathrm{P8_{TFs}}$ and $\mathrm{P16_{TFs}}$ to theTFs (Table 4.7).

The simulation time was 300 s, the same duration as used by Chanson et al. (2004) to compute the distribution of the void fraction from the laboratory measurements, and the time step varied with respect to the CFL condition. C_{max} was set equal to 0.3. The number of cells in the computational domain was 1.89×10^6 and the corresponding cores and memory were 10 and 36 GB, respectively. It required 168 h to simulate the real time of $t_f = 300$ s (also for the corresponding times at reduced scales, Catucci et al., 2022a).

Results for the water jet

Figure 4.8 shows the time-averaged γ along the section A-A' for domains P1, P8, $P8_{PFs}$ and $P8_{TFs}$. P1 results show a distribution of the time-averaged void fraction that is consistent with the description of high R plunging jets provided by Hassan et al. (2019). In particular, the flow shows the characteristic conical shape of the air-entrainment layer and the dispersion of bubbles due to the buoyancy effects outside the cone. The consequence of air entrainment in the flow is a rise of the free surface with respect to the initial conditions (Figure 4.8a,b,c). Domains P8 and $P8_{PFs}$ have the identical shape of the air-entrainment layer showing also that the free surface reaches the same level, while $P8_{TFs}$ shows clear differences.

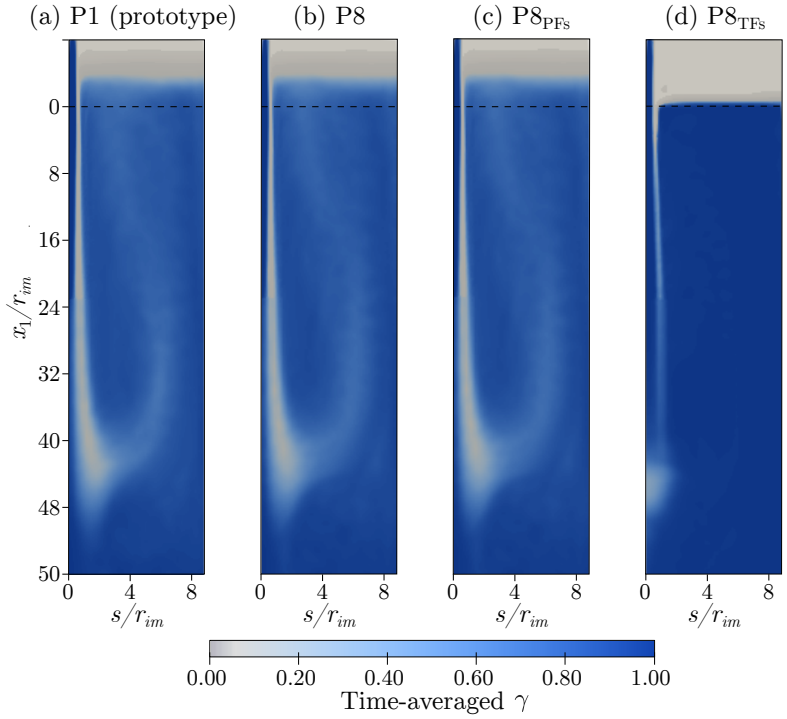


Figure 4.8: Time-averaged γ along the section A-A' for domains (a) P1, (b) P8, (c) $P8_{PFs}$ and (d) $P8_{TFs}$ (Catucci et al., 2021).

The following results are all shown along section A-A' at $\frac{x_1-l_1}{r_{im}} = 1.60$. The distribution of the void fraction is compared with the experimental results of Chanson et al. (2004) in Figure 4.9. The computed distribution and that

measured in Chanson et al. (2004) are shown to have a close agreement. The NSLs and the PFs capture the distribution of the void fraction of the prototype correctly, both in terms of the shape and magnitude. On the other hand, the TFs fail to describe the void fraction distribution.

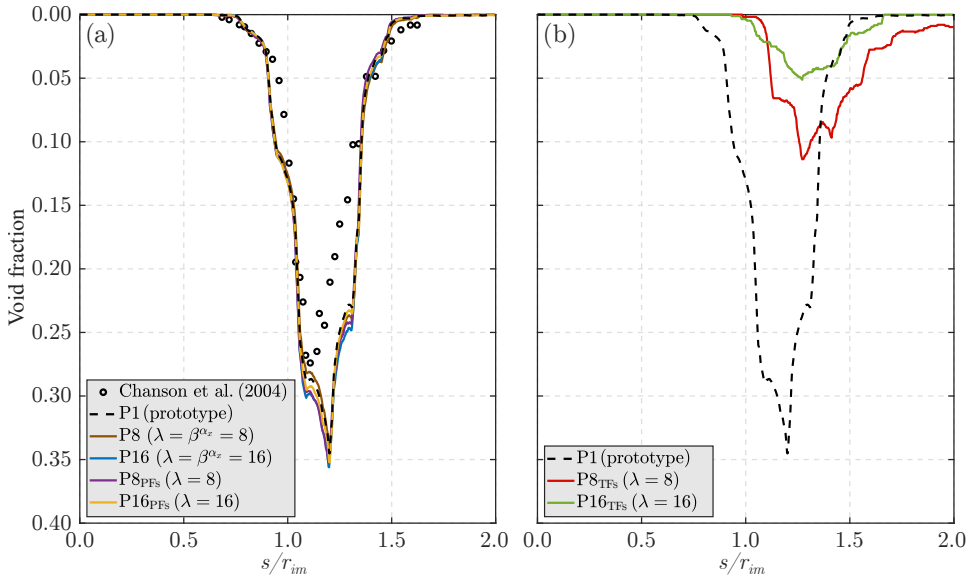


Figure 4.9: Distributions of the void fraction for the plunging jet for domains (a) P1, P8, P16, $P8_{PFs}$ and $P16_{PFs}$ and (b) P1, $P8_{TFs}$ and $P16_{TFs}$ along section A-A' at $\frac{x_1 - l_1}{r_{im}} = 1.60$ (Catucci et al., 2021).

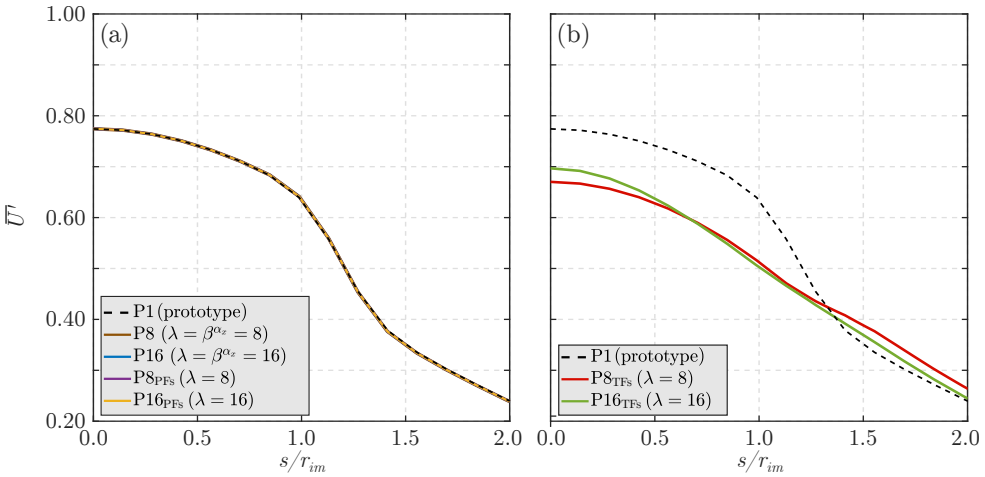


Figure 4.10: Time-averaged U' for the plunging jet for domains (a) P1, P8, P16, $P8_{PFs}$ and $P16_{PFs}$ and (b) P1, $P8_{TFs}$ and $P16_{TFs}$ along section A-A' at $\frac{x_1 - l_1}{r_{im}} = 1.60$ (Catucci et al., 2021).

Figure 4.10 shows the time-averaged dimensionless velocity magnitude $\overline{U'}$ where for this case $U' = U/U_{im}$. In the prototype, the maximum value of

$\overline{U'}$ is at the jet centreline and $\overline{U'}$ follows qualitatively the same velocity distribution as found in McKeogh and Ervine (1981). While the results of the domains P1, P8, P16, $P8_{PFs}$ and $P16_{PFs}$ are identical, $\overline{U'}$ for the domains $P8_{TFs}$ and $P16_{TFs}$ are lower than in the prototype.

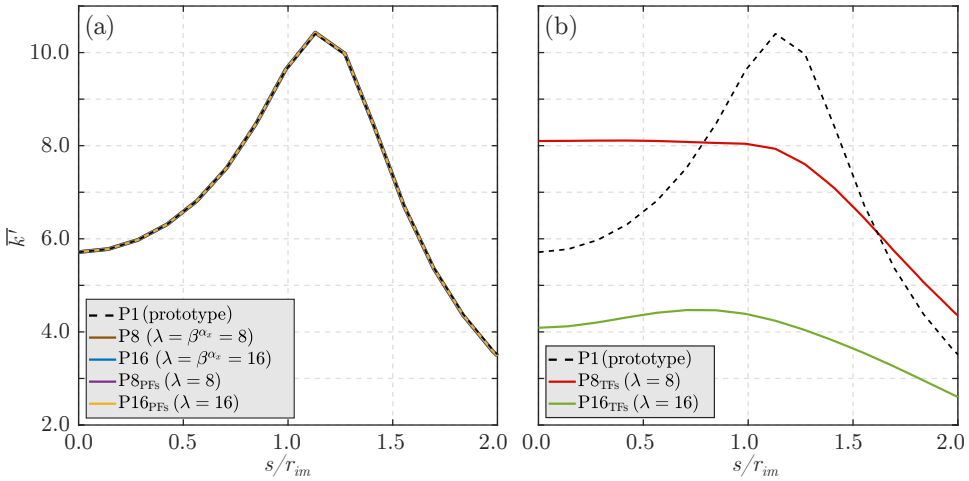


Figure 4.11: Time-averaged k' for the plunging jet for domains (a) P1, P8, P16, $P8_{PFs}$ and $P16_{PFs}$ and (b) P1, $P8_{TFs}$ and $P16_{TFs}$ along section A-A' at $\frac{x_1 - l_1}{r_{im}} = 1.60$ (Catucci et al., 2021).

Figure 4.11 shows the time-averaged dimensionless turbulent kinetic energy $\overline{k'}$, where $k' = k/(gr_{im})$. In the prototype and self-similar domains the maximum value is $\overline{k'} = 10$ at $s/r_{im} = 1.0$ beyond which $\overline{k'}$ decreases to less than 4.0 at $s/r_{im} = 2.0$. On the other hand, the flow behaviour in the domains based on TFs is different. Indeed, $\overline{k'}$ in $P8_{TFs}$ does not show a clear peak and remains almost constant as far as $s/r_{im} = 1.0$ beyond which it decreases. Moreover, the value of $\overline{k'}$ around the jet is higher in $P8_{TFs}$ than in the prototype. However, $P16_{TFs}$ shows a lower $\overline{k'}$ than the prototype with a maximum value of $\overline{k'} \approx 4.5$.

4.3 Compressible air-water flows test cases

Some of the results presenting in this Section 4.3 are contained in Catucci et al. (2022b).

4.3.1 Dam break flow

In this section, the NSLs where the air is considered compressible are validated by using the same set-up of the dam break flows presented in Section 4.2.1. The effects of air compressibility are visible when the air pocket is entrapped downstream the obstacle, and thus compressed. Hence, the variation of air density influences the behaviour of the dam break flows, above all after the flow impacts the obstacle. In Section 5.3 the discussion on the difference between the dam break flows with and without considering the air compressibility is fully covered.

Since the air is considered compressible here the thermophysical properties of fluids and the temperature are added as parameters that need to be scaled. The *compressibleInterIsoFoam* is used as a solver to compute also the equations of heat transfer and the perfect gas.

Numerical set-up for the dam break flows

The setup and the mesh were the same as in Section 4.2.1 with the only difference that air was assumed to be compressible. Hence, the initial density of air was $\rho_{a,0} = 1$ kg m^{-3} and its variation was described by Eq. (3.49). The kinematic and dynamic viscosities of air were $\nu_a = 1.48 \times 10^{-5}$ m^2 s^{-1} and $\mu_a = 1.48 \times 10^{-5}$ kg m^{-1} s^{-1}, respectively. The water density

was $\rho_w = 1000$ kg m^{-3} and was considered constant, $\sigma = 0.07$ N m^{-1}, $\nu_w = 1 \times 10^{-6}$ m^2 s^{-1} and $\mu_a = 1 \times 10^{-3}$ kg m^{-1} s^{-1}. T_0 of the entire domain was set at 293 K, $c_{v,w} = 4195$ J kg^{-1} K^{-1} and $c_{v,a} = 1007$ J kg^{-1} K^{-1}.

At the start of the simulations, $\Delta t = 0.001$ s and it was varied following the CFL conditions (Eq. 4.1). It required almost 4 h to simulate the actual time of $t_f = 6$ s.

The schemes used for each variables are summarised in Table 4.8 and they are invariant trough the scales.

Table 4.8: Numerical schemes for the dam break simulations.

ddtSchemes	Euler
gradSchemes	Gauss linear
divSchemes	
div(rhoPhi,U)	Gauss upwind
div(phi,p)	Gauss upwind
div(phi,alpha)	Gauss vanLeer
div(phi, k)	Gauss upwind
div(phi, epsilon)	Gauss upwind
div(rhoPhi,T)	Gauss upwind
laplacianSchemes	Gauss linear corrected

Application of the NSLs for compressible air-water

Two self-similar domains, namely CD8 and CD16, are designed by applying the scaling conditions in terms of α_x, $\alpha_R = \alpha_T = \alpha_{Mm} = 0$ and $\alpha_n = 3\alpha_x$ (fourth and fifth columns of Table 3.2). CD8 and CD16 were created with scaling factors of $\lambda = \beta^{\alpha_x} = 8$ and 16, respectively. To achieve this, it was assumed that $\alpha_x = 1$ such that $\beta = 8$ (CD8) and 16 (CD16), respectively. Their specific values for the prototype and the scaled models, obtained by applying the conditions in Table 4.9, are presented in Table 4.10. The prototype is also scaled by using TFs using the same λ as in the self-similar domains (therefore obtaining the domains CD8_{TFs} and CD16_{TFs}).

Table 4.9: Scaling parameters and exponents used to scale the dam break flow prototype values to the corresponding values in the domains CD8 and CD16 using the NSLs.

	Domain CD8	**Domain CD16**
Scaling parameter β	8	16
Scaling exponents		
x_i (m) α_x	1	1
t (s) α_t	1	1
ρ (kg m^{-3}) α_ρ	0	0
U_i (m s^{-1}) α_U	0	0
g (m s^{-2}) α_g	-1	-1
p (Pa) α_p	0	0
ν (m^2 s) α_ν	1	1
μ (kg m^{-1} s^{-1}) α_μ	1	1
σ (N m^{-1}) α_σ	1	1
c_v (J kg^{-1} K^{-1}) α_{c_v}	0	0
Scaling ratios		
x_i (m) β^{α_x}	8.00	16.00
t (s) β^{α_t}	8.00	16.00
ρ (kg m^{-3}) β^{α_ρ}	1.00	1.00
U_i (m s^{-1}) β^{α_U}	1.00	1.00
g (m s^{-2}) β^{α_g}	0.1250	0.0625
p (Pa) β^{α_p}	1.00	1.00
ν (m^2 s) β^{α_ν}	8.00	16.00
μ (kg m^{-1} s^{-1}) β^{α_μ}	8.00	16.00
σ (N m^{-1}) β^{α_σ}	8.00	16.00
c_v (J kg^{-1} K^{-1}) $\beta^{\alpha_{c_v}}$	1.00	1.00

Table 4.10: Parameters for the dam break flow in the prototype and the scaled domains.

Parameters	**Prototype CD1**	**Domain CD8**	**Domain CD16**	**Domain CD8$_{\mathrm{TFs}}$**	**Domain CD16$_{\mathrm{TFs}}$**
h_w (m)	0.55	0.06875	0.034375	0.06875	0.034375
t_f (s)	6	2.12	1.5	2.16	1.5
g (m s^{-2})	9.81	78.48	156.96	9.81	9.81
ρ_w (kg m^{-3})	1000	1000	1000	1000	1000
ν_w (m^2 s^{-1})	10^{-6}	1.25×10^{-7}	6.25×10^{-8}	10^{-6}	10^{-6}
μ_w (kg m^{-1} s^{-1})	10^{-3}	1.25×10^{-4}	6.25×10^{-5}	10^{-3}	10^{-3}
$\rho_{a,0}$ (kg m^{-3})	1	1	1	1	1
ν_a (m^2 s^{-1})	1.48×10^{-5}	1.85×10^{-6}	9.25×10^{-7}	1.48×10^{-5}	1.48×10^{-5}
μ_a (kg m^{-1} s^{-1})	1.48×10^{-5}	1.85×10^{-6}	9.25×10^{-7}	1×10^{-3}	1×10^{-3}
σ (N m^{-1})	0.07	0.00875	0.004375	0.07	0.07
$c_{v,w}$ (J kg^{-1} K^{-1})	4195	4195	4195	4195	4195
$c_{v,a}$ (J kg^{-1} K^{-1})	1007	1007	1007	1007	1007
T_0 (K)	293	293	293	293	293

Results for the dam break flow considering air compressible

Figure 4.12 shows snapshots of the prototype and the scaled domains at $x_2' = 0$ and $t' = 2.7$ (Figure 4.1). The prototype shows a large free surface deformation after impacting the obstacle even if it is less severe than in the incompressible case (Figures 4.12a). The self-similar domains reproduce the water tongue of the prototype, showing also a detachment of water at

the tip. The values of $\text{RMSE}_{U'}$ computed for CD8 and CD16 with respect to CD1 confirm the same velocity field between the prototype and the self-similar domains (Table 4.11). On the other hand, TFs do not reproduce the behaviour of the prototype correctly. Indeed, CD8_{TFs} and CD16_{TFs} do not show fluid detachment from the tongue (Figure 4.12d,e). The values of the $\text{RMSE}_{U'}$ confirm the divergence between CD1 and the models designed by using the TFs (Table 4.11).

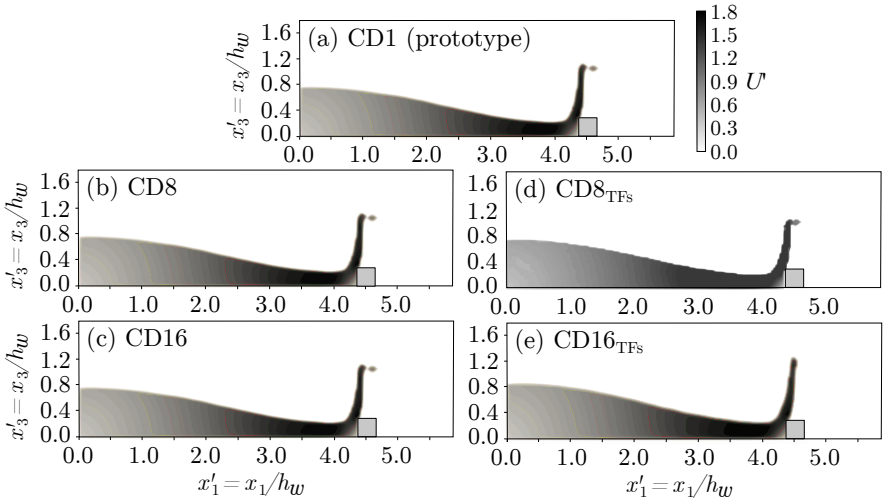


Figure 4.12: Snapshots of the dam break flow at the cross-section $x_2' = 0$ and dimensionless time $t' = 2.7$ of the (a) prototype and scaled with (b,c) the NSLs and (d,e) TFs.

Table 4.11: $\text{RMSE}_{U'}$ computed for domains CD8, CD16, CD8_{TFs} and CD16_{TFs} with respect to CD1, for the snapshots in Figure 4.12.

$\textbf{RMSE}_{U'}$			
CD1-CD8	**CD1-CD16**	**CD1-CD8$_{\text{TFs}}$**	**CD1-CD16$_{\text{TFs}}$**
1.13×10^{-4}	1.11×10^{-4}	0.025	0.055

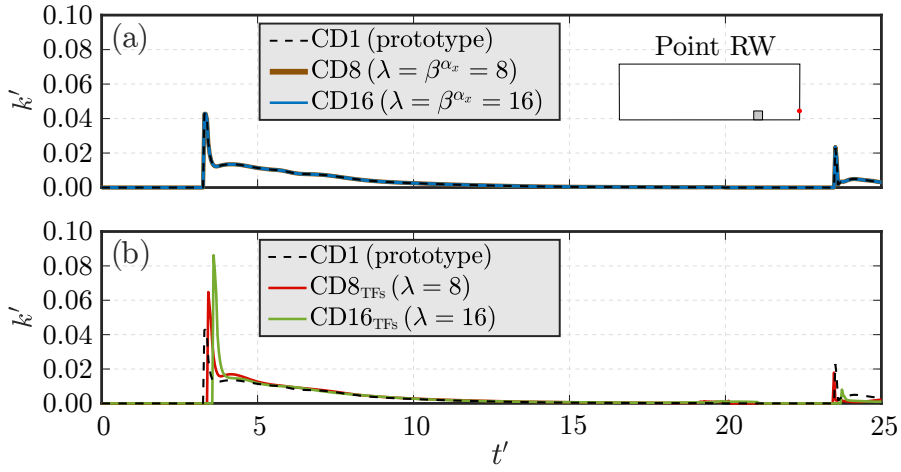


Figure 4.13: k' time histories in the dam break flow at point RW for (a) domains CD1, CD8, CD16 and (b) CD1, CD8$_{\text{TFs}}$ and CD16$_{\text{TFs}}$.

Figures 4.13 and 4.14 show the time histories of k' and γ, respectively, at point RW. The first peak of k' occurs at $t' = 3.33$ and the second one when the wave is re-reflected at $t' = 23.52$. The perfect collapse of the data for CD1, CD8 and CD16 affirms the self-similar behaviour of k' and γ for the NSLs. On the other hand, k' and γ show scale effects using the TFs. Indeed, both peaks of k' decrease with increasing λ. γ starts to increase at $t' = 3.42$, meaning that the wave reaches point RW consistently at the same time in all domains except for CD8$_{\text{TFs}}$ and CD16$_{\text{TFs}}$ (Figure 4.14). These differences become more visible at a later stage of the simulation when the dam break wave is reflected and the value of γ decreases. Indeed, domain CD16$_{\text{TFs}}$ shows a strong difference with respect to CD1.

A more direct influence of the air compressibility can be seen on the time history of the dimensionless pressure p'_{rel} (Figure 4.15). This shows a strong oscillation at $t' = 5$. At this time, an air pocket is entrapped by the falling water tongue (Figure 4.16) and it undergoes expansion and contraction alternately, leading to a strong oscillation of p'_{rel}. Domains CD8 and CD16 reproduce this behavior perfectly, since the results overlap. The domains scaled with TFs behave qualitatively as CD1 but the effects of air com-

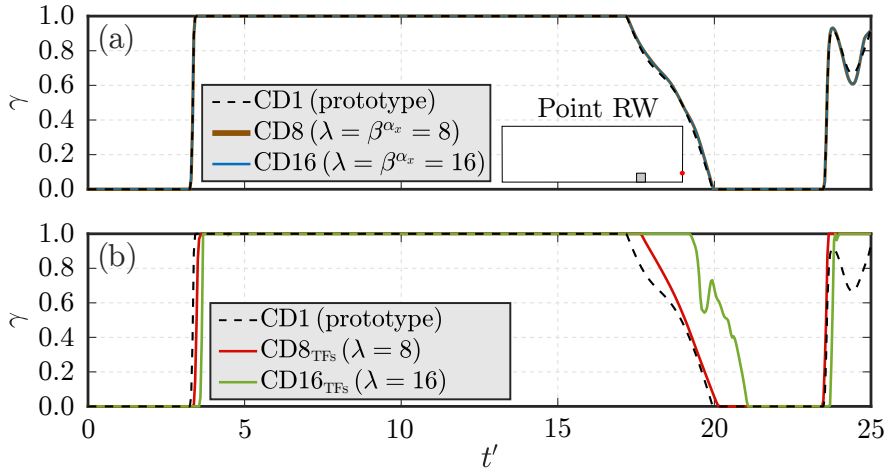


Figure 4.14: γ time histories in the dam break flow at point RW for (a) domains CD1, CD8 and CD16 and (b) CD1, CD8$_{\text{TFs}}$ and CD16$_{\text{TFs}}$.

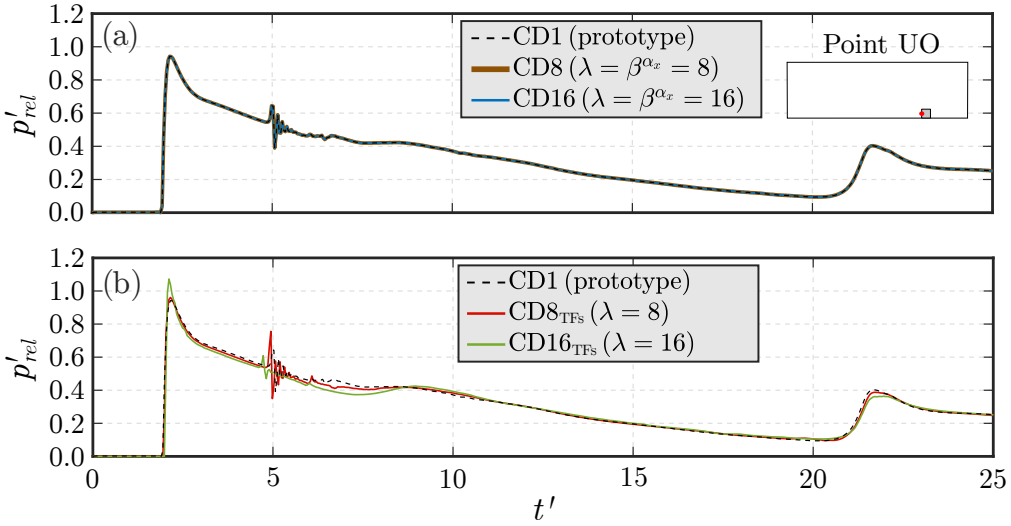


Figure 4.15: p'_{rel} time histories in the dam break flow at point P2 for (a) domains CD1, CD8 and CD16 and (b) CD1, CD8$_{\text{TFs}}$ and CD16$_{\text{TFs}}$.

pressibility are not well reproduced. Indeed, the oscillation at $t' = 5$ (see Figure 4.15 is bigger in CD8$_{\text{TFs}}$ with respect to CD1, while it is reduced in CD16$_{\text{TFs}}$. Hence, the compressibility effects are not well scaled.

Figure 4.16 shows the dam break water flows at the cross-section $x'_2 = 0$ and $t' = 5$. In CD1, CD8 and CD16 the free surface shapes are identical and the entrapped air pocket surrounds the obstacle even on the top. In CD8$_{\text{TFs}}$, the air pocket between the water tongue and the obstacle is similar to the one in CD1 but the air compressibility effects are over-represented,

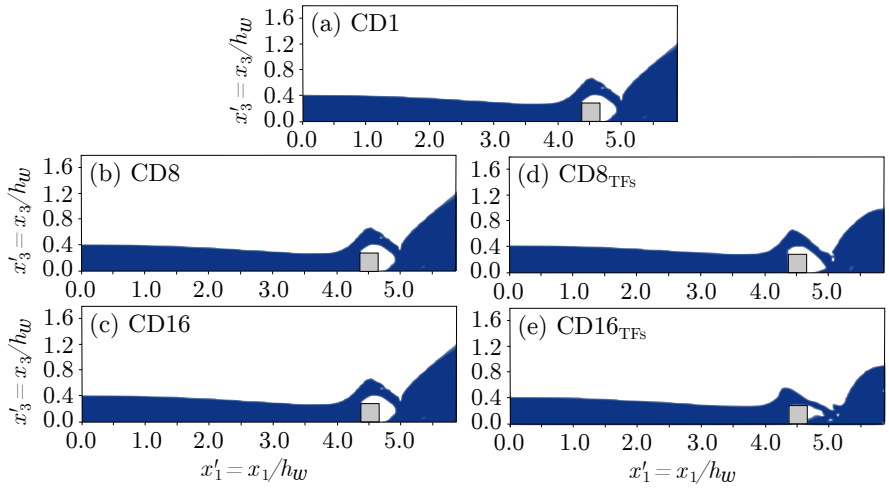


Figure 4.16: Snapshots of the dam break flow at the cross-section $x_2' = 0$ and dimensionless time $t' = 5$ of the (a) prototype and scaled with (b,c) the NSLs and (d,e) the TFs.

as well as the oscillation of the dimensionless pressure. In domain CD16_{TFs}, the air pocket is smaller and confined upstream of the obstacle, explaining the reduction of the pressure oscillation shown in Figure 4.15.

4.3.2 Taylor bubble

A Taylor bubble is a slug-shaped bubble of gas, raising in a vertical pipe filled with a liquid. Its behaviour depends on the gravitational acceleration, viscosity, density, surface tension and also the compressibility of the fluids (Davies and Taylor, 1950; Llewellin et al., 2012). It is usually divided in four parts: (1) a hemispherical tip called the nose, (2) a body surrounded by a film of fluid, (3) a tail region and (4) a wake, which can be laminar or turbulent. In this section, the NSLs were applied to the Taylor bubble presented in the experiments of Pringle et al. (2015) and in the numerical study of Ambrose et al. (2016). The fluid inside the bubble is compressible air surrounded by incompressible water.

Numerical set-up for the Taylor bubble

The numerical domain consisted of a vertical cylinder of height 9.50 m with an internal diameter $d = 0.29$ m. Initially, the pipe was filled with water to a depth of 5.00 m. A bubble of air was introduced close to the bottom of the pipe by setting $\gamma = 0$ in the bubble region. The initial shape of the bubble used in the numerical simulations was a hemisphere with a radius of 0.14 m on the top of a cylinder with the same radius and a height of 0.50 m, resulting in a total height of $h_b = 0.64$ m. The nose of the bubble was located at $x_3 = 1.64$ m from the bottom of the pipe (Figure 4.17). The initial pressure inside the bubble p_0 was set at a constant value matching the hydrostatic water pressure at the nose. The water had a constant density $\rho_w = 1000$ kg m^{-3}, $\sigma = 0.07$ N m^{-1} and the kinematic and dynamic viscosities were $\nu_w = 1 \times 10^{-6}$ m^2 s^{-1} and $\mu_w = 1 \times 10^{-3}$ kg m^{-1}s^{-1}, respectively. The initial density of air was $\rho_{a,0} = 1$ kg m^{-3}, $\nu_a = 1.48 \times 10^{-5}$ m^2 s^{-1} and $\mu_a = 1.48 \times 10^{-5}$ kg m^{-1}s^{-1}. T_0 of the entire domain was set at 293 K, $c_{v,w} = 4195$ m^2 K^{-1} s^{-2} and $c_{v,a} = 1007$ m^2 K^{-1} s^{-2}.

The top boundary of the domain was modelled as a fully transmissive open boundary condition at atmospheric pressure. The no-slip boundary condition was applied at the lateral and bottom walls. Note that, because of the orientation of the reference frame, $g_{\mathrm{i}} = (0, 0, -g)$ in Eq. (3.47).

A structured O-grid mesh was created with a spacing of 0.0025 m at the wall increasing to 0.0075 m at the centre (Figure 4.17c) while the cells were 0.008 m tall. The mesh was refined near the wall to resolve the film around the Taylor bubble. The time step Δt was set to 0.0005 s at the start of the simulation and it was subsequently varied to respect the CFL condition in Eq. (4.1). The number of cells in the computational domain

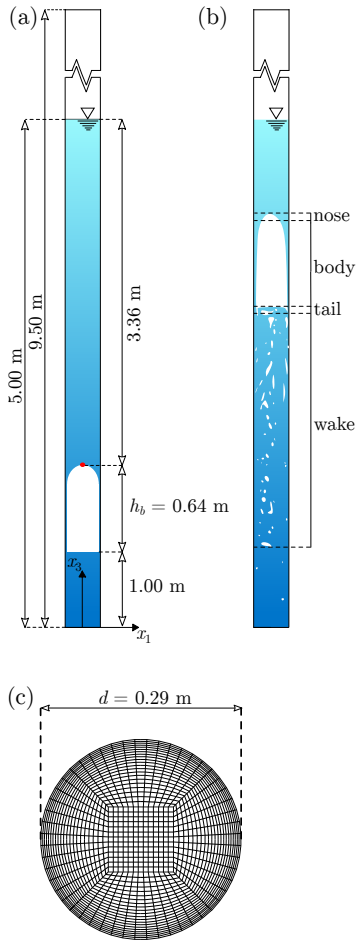


Figure 4.17: Schematic illustration of the computational domain at prototype scale: (a) the longitudinal section of the domain, (b) the Taylor bubble region and (c) a cross-section of the mesh (Catucci et al., 2022b)

was 1513200 and it required 8 h to simulate the actual time of $t_f = 3.4$ s by using 16 cores and 15 GB of memory (also for the corresponding times at reduced scales). All the dimensional parameters, including the mesh sizes and time steps, were scaled to the smaller domains according to the selected scaling laws. The schemes used for each variables are the same used for the dam break considering air compressible (Table 4.8) and they are invariant trough the scales.

Application of the NSLs to the Taylor bubble

Three self-similar domains, namely T4, T8 and T16, were created with geometrical scale factors of $\lambda = \beta^{\alpha_x} = 4$, 8 and 16, to obtain T4, T8 and T16, respectively. All variables and parameters were transformed with the scaling exponents in the sixth and seventh columns of Table 3.1 (with scaling conditions in terms of α_x, $\alpha_R = \alpha_T = \alpha_{Mm} = 0$ and $\alpha_n = 3\alpha_x$). Their specific values for the prototype and the scaled models, obtained by applying the conditions in Table 4.9, are presented in Table 4.12. The prototype was also scaled by using the TFs ($T4_{TFs}$, $T8_{TFs}$ and $T16_{TFs}$) using the same λ as in the self-similar domains and by keeping the fluids properties and the temperature invariant as summarised in Table 4.12.

Table 4.12: Parameters for the Taylor bubble in the prototype and the scaled domains (Catucci et al., 2022b).

Domain	T1	T4	T8	T16	$T4_{TFs}$	$T8_{TFs}$	$T16_{TFs}$
d (m)	0.290000	0.072500	0.036250	0.018125	0.072500	0.036250	0.018125
h_b (m)	0.640	0.160	0.080	0.040	0.160	0.080	0.040
t_f (s)	3.50000	0.87500	0.43750	0.21875	1.75000	1.23700	0.87500
g (m s^{-2})	9.81	39.24	78.48	156.96	9.81	9.81	9.81
p_0 (MPa)	0.134286	0.134286	0.134286	0.134286	0.033571	0.016785	0.008393
ρ_w (kg m^{-3})	1000	1000	1000	1000	1000	1000	1000
$\rho_{a,0}$ (kg m^{-3})	1	1	1	1	1	1	1
ν_w (m^2 s^{-1})	1×10^{-6}	2.50×10^{-7}	1.25×10^{-7}	6.25×10^{-8}	1×10^{-6}	1×10^{-6}	1×10^{-6}
μ_w (kg m^{-1} s^{-1})	1×10^{-3}	2.50×10^{-4}	1.25×10^{-4}	6.25×10^{-5}	1×10^{-3}	1×10^{-3}	1×10^{-3}
σ (N m^{-1})	0.07	1.75×10^{-2}	8.75×10^{-3}	4.38×10^{-3}	0.07	0.07	0.07
$c_{v,w}$ (J kg^{-1} K^{-1})	4195	4195	4195	4195	4195	4195	4195
$c_{v,a}$ (J kg^{-1} K^{-1})	1007	1007	1007	1007	1007	1007	1007
T_0 (K)	293	293	293	293	293	293	293

Results of the Taylor bubble

The numerical simulation of the prototype overestimates the rise velocity of the Taylor bubble presented in Pringle et al. (2015) by approximately 40% with a dimensionless velocity $U_b' = U_b/\sqrt{gd} = 0.486$, where U_b is the velocity magnitude of the bubble nose. This difference is due to the errors introduced in the numerical simulations and similar in nature to

that observed in Ambrose et al. (2016). It is worth mentioning that the differences with the experimental results do not affect the test of the NSLs as the test is based on comparing the results of T1 with the ones from the scaled domains.

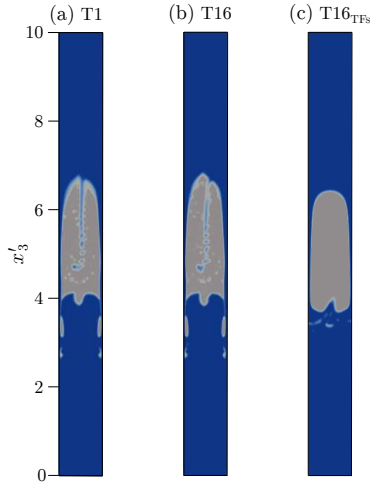


Figure 4.18: Snapshot of the Taylor bubble at the cross-section $x_2' = 0$ and dimensionless time $t' = 2.90$ of the (a) prototype, (b) T16 and (c) $\mathrm{T16_{TFs}}$ (Catucci et al., 2022b).

Nevertheless, the general behaviour of the Taylor bubble agrees qualitatively with the experimental findings of Pringle et al. (2015). The bubble transits to its stable shape between dimensionless time $t' = t\sqrt{g/d} = 0$ and 6 in the prototype. After $t' = 6$, the slug shaped bubble fully forms, rising with a constant U_b'.

The initial stage of bubble formation is illustrated in Figure 4.18, showing the cross-section $x_2' = x_2/d = 0$ at $t' = 2.90$ of T1, T16 and $\mathrm{T16_{TFs}}$. Both T1 and T16 show the bubble divided by the water. Note that the details of the air bubbles differ between T1 and T16, however, the dynamics of the transition of the bubble to the final shape is the same. In $\mathrm{T16_{TFs}}$, a slug-shape bubble is formed with a very limited wake and smaller bubbles.

In the domain scaled with the TFs the behaviour of the bubble is signif-

icantly different. Indeed, the nose is rounder with respect to T1 when it reaches $x_3' = 10$. Moreover, the wake contains less air along the x_3' axis.

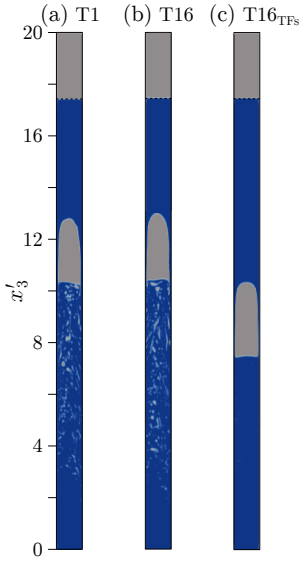


Figure 4.19: Snapshot of the Taylor bubble at the cross-section $x_2' = 0$ and dimensionless time $t' = 14.54$ of the (a) prototype, (b) T16 and (c) T16_{TFs} (Catucci et al., 2022b).

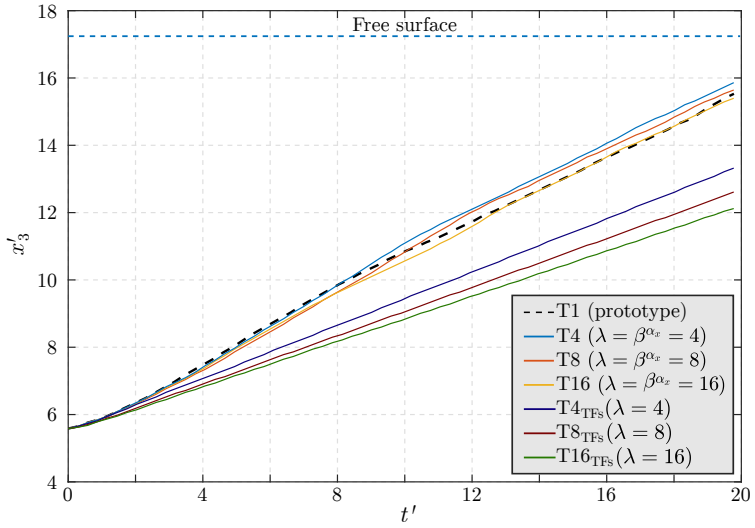


Figure 4.20: Time history of the bubble nose location on the x_3' coordinate for the prototype and all the scaled domains.

Figure 4.19 shows the cross-sections $x_2' = 0$ of the domains at $t' = 14.54$ for T1, T16 and T16_{TFs}. The prototype and T16 show the typical slug shape with the nose situated almost at $x_3' = x_3/d = 13$. Further, the shedding of

smaller bubbles can be seen in the wake of the main one.

Table 4.13: U_b' for the prototype and all scaled domains (Catucci et al., 2022b).

	T1	T4	T8	T16	$T4_{TFs}$	$T8_{TFs}$	$T16_{TFs}$
U_b'	0.486	0.476	0.495	0.482	0.398	0.363	0.337
$E_{U_b'}$ (%)	-	2.06	1.85	0.82	18.11	25.31	30.66

Figure 4.20 shows the time history of the x_3' position of the nose. The slopes of the curves represent U_b'. U_b' is computed after $t' = 6$, i.e. after the initial stage in which the bubble shape is unstable. As shown in Table 4.13, U_b' for T4, T8 and T16 are nearly self-similar with respect to the prototype. Table 4.13 shows also the relative differences of U_b' computed as

$$E_{U_b'} = 100\frac{|U_{b,p}' - U_{b,m}'|}{U_{b,p}'}, \tag{4.5}$$

where $U_{b,p}'$ is the value of U_b' in the prototype and $U_{b,m}'$ in the scaled domains. The small differences between the prototype and the models scaled with the NSLs are also confirmed in Figure 4.20, where the respective curves do not overlap. Nevertheless, the differences are not directly proportional to λ, as also shown by $E_{U_b'}$, which is even smaller for T16 than for T4 and T8 (Table 4.13). On the other hand, by using the TFs, $E_{U_b'}$ increases with increasing λ, reaching 30.66% in $T16_{TFs}$.

It is relevant to analyse whether the NSLs guarantee self-similarity with respect to Eq. (3.51). Figure 4.21 shows the time histories of the averages of the dimensionless densities $\overline{\rho'} = \overline{\rho}/\rho_{a,0}$, temperatures $\overline{T'} = \overline{T}/T_0$ and pressures $\overline{p'} = \overline{p}/p_0$ inside the bubbles as well as the variation of the corresponding dimensionless volumes $V' = V/d^3$, for the self-similar domains. The prototype T1, T4, T8 and T16 show a sudden increase in $\overline{\rho'}$ and, from $t' = 6$, $\overline{\rho'}$ decrease almost linearly. This is due to the sudden compression at the initial, transitory, stage of motion (Figure 4.18a). In the prototype,

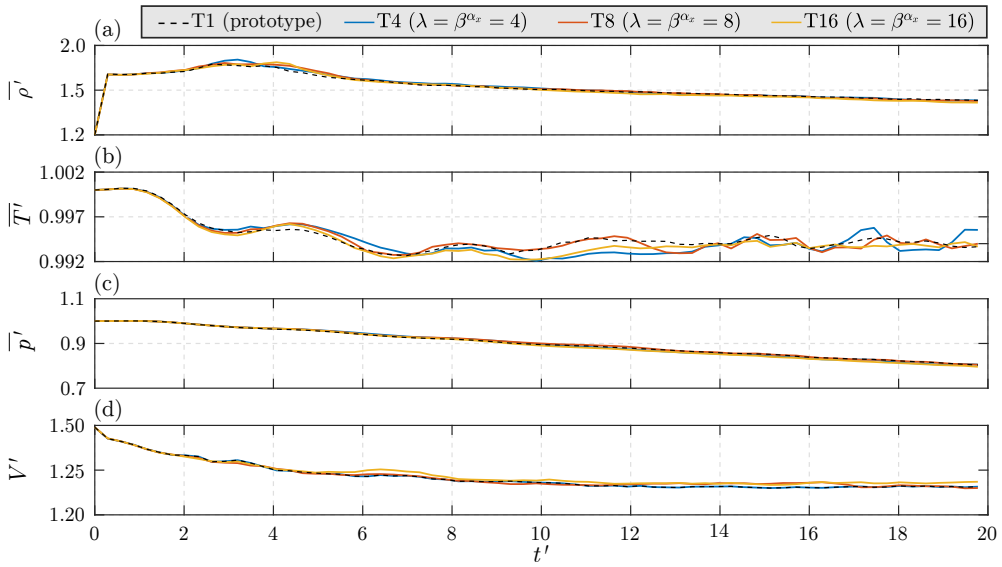


Figure 4.21: Time histories of the averages of the (a) $\overline{\rho'}$, (b) $\overline{T'}$ and (c) $\overline{p'}$ inside each modelled Taylor bubble and (d) V' for T1, T4, T8 and T16 (Catucci et al., 2022b).

$\overline{T'}$ consistently decreases with some fluctuations. This behaviour is also replicated in T4, T8 and T16, even if the curves do not perfectly overlap. The differences in T' between the prototype and the scaled domains are less than ± 0.005 such that they do not indicate significant scale effects. $\overline{p'}$ matches between the prototype and the self-similar domains, decreasing linearly with the ascent of the bubble. Furthermore, the volume of the bubble V' confirms self-similarity between T1, T4, T8 and T16.

The time histories of $\overline{\rho'}$, $\overline{T'}$, $\overline{p'}$ and V' for the domains scaled with the TFs are presented in Figure 4.22. In contrast to the NSLs, T4_{TFs}, T8_{TFs} and T16_{TFs} fail to reproduce the behaviour of the prototype and the time series of the aforementioned parameters are completely different from those of the prototype and those obtained with the NSLs. Indeed, $\overline{\rho'}$ decreases and remains constant from $t' = 0.5$ until the end of the simulation.

Figure 4.23 shows the time history of the void fraction in the wake, namely the volume of air in the wake divided by the volume of the entire domain

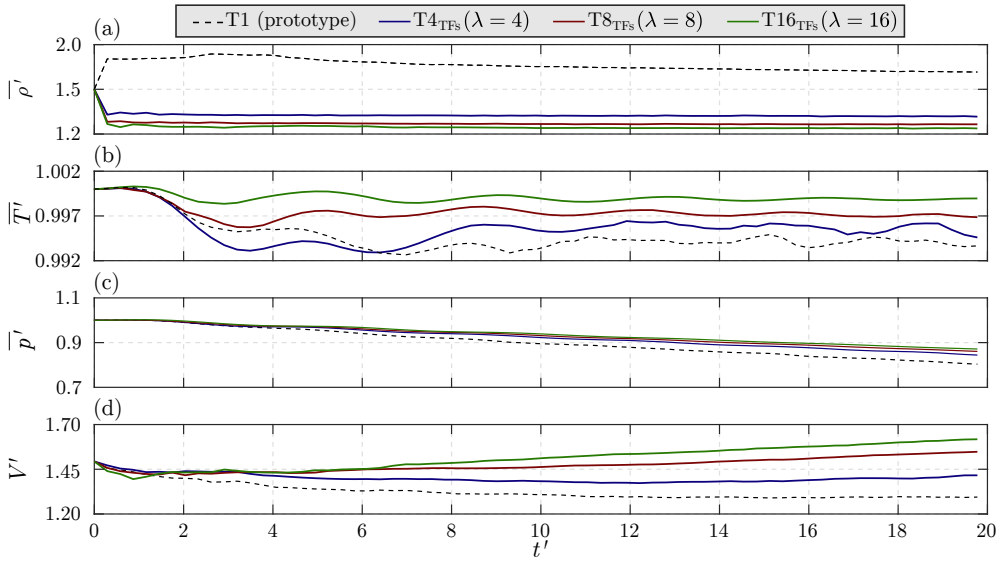


Figure 4.22: Time histories of the averages of the (a) dimensionless density $\overline{\rho'}$, (b) dimensionless temperature $\overline{T'}$ and (c) dimensionless pressure $\overline{p'}$ inside the bubbles and (d) the dimensionless volume V' for T1, $\mathrm{T4_{TFs}}$, $\mathrm{T8_{TFs}}$ and $\mathrm{T16_{TFs}}$ (Catucci et al., 2022b).

between the bottom and the free surface. The general behaviour in the domains T1, T4, T8 and T16 is the same, having a void fraction around 0.035 at the end of the simulation. In contrast, the differences observed in domains $\mathrm{T4_{TFs}}$, $\mathrm{T8_{TFs}}$ increase with λ.

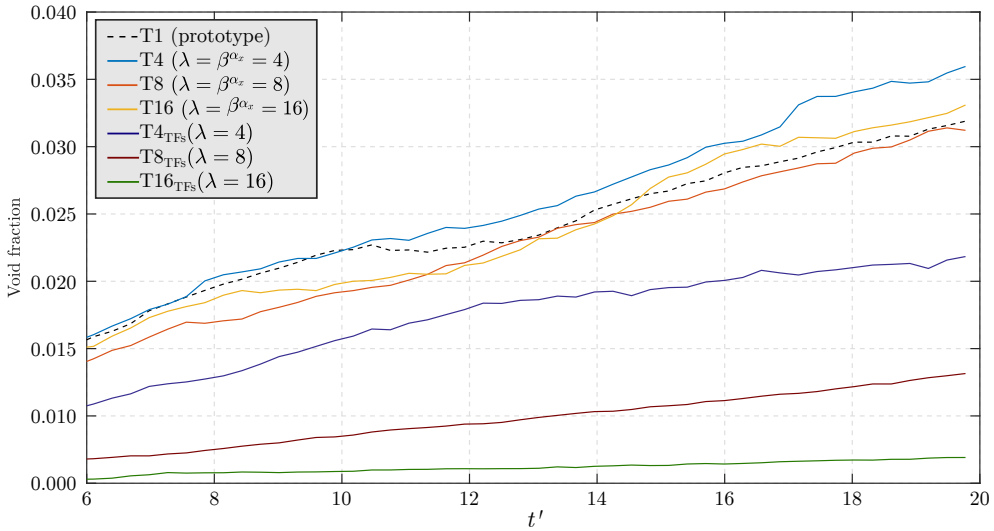


Figure 4.23: Time history of the void fraction lost in the wake of the bubble for the prototype and the scaled domains.

4.4 Summary

The derived NSLs were applied to different test cases by using *interFoam* when air was considered incompressible and *compressibleInterIsoFoam* when air compressibility was considered. Both solvers are available in the OpenFOAM v.1706 CFD package and are based on volume of fluid method.

The NSLs for air-water flows were tested with the simulations of phenomena: (i) a dam break flow interacting with an obstacle and (ii) a plunging water jet. The NSLs where air is considered compressible are applied to (i) the same set-up of the dam break flow for compressible case and (ii) a Taylor bubble.

The results for NSLs were compared with the scaled models designed by using the TFs. In addition, the incompressible test cases were also scaled by using the PFs. The results confirm that the NSLs can guarantee the self-similarity of incompressible and compressible air-water flows. On the other hand, all the test cases clearly show the presence of scale effects when the TFs are applied.

Some differences, above all on the dimensionless pressure p'_{rel}, are shown between the dam break flow simulated with *interFoam* and *compressibleInterIsoFoam* because in the second case the equations of heat transfer and perfect gas are also solved.

Chapter 5

Discussion of results

5.1 Introduction

NSLs were obtained for incompressible and compressible air-water flows and numerically validated with a range of air-water flow phenomena in OpenFOAM. In this chapter, theoretical aspects of the NSLs and their test are discussed. Finally, the implications of the NSLs in the laboratory are discussed and an easy to use MATLAB app to obtain suitable configurations is presented.

5.2 Discussion on the NSLs

The NSLs for incompressible air-water flows are consistent with those reported in Ercan and Kavvas (2017) (compare Tables 1 and 2 of Ercan and Kavvas, 2017 with Table 3.1 in the present thesis, Catucci et al. 2021) with the addition of the surface tension and the curvature of the free surface (second and third columns of Table 3.1). When air compressibility

is taken into account, the equations of heat transfer and perfect gas are included in the governing equations. The resulting scaling laws are consistent with those of incompressible air-water flows with the addition of the thermophysical parameters such as T, n, R, M_m and c_v (second and third columns of Table 3.2). The main differences between the incompressible and compressible scaling laws are the selected configurations. In the former, it was chosen to keep g invariant between the models and the prototype, leading to $\alpha_t = \alpha_x^{0.5}$ (sixth and seventh columns of Table 3.1). In the latter, the main restrictions introduced for physical consistency are the invariance of R and T and thus $\alpha_t = \alpha_x$ (sixth and seventh columns of Table 3.2). It is worth noting that any configuration of the NSLs guarantees self-similarity as long as it follows the relationships among the scaling exponents resulting from the application of the Lie group scaling method (second and third columns of Tables 3.1 and 3.2).

This flexibility in allowing different configurations is one of the main advantages of the NSLs with respect to the traditional scaling approach (Carr et al., 2015; Polsinelli and Kavvas, 2016). Moreover, it is shown that the precise Froude scaling laws (PFs) are a special configuration of the NSLs written in terms of α_x, $\alpha_\rho = \alpha_g = 0$. This is because the NSLs are derived from the governing equations and they take into account all the involved effects (Kline, 1965).

5.3 Discussion of numerical test cases

In this work, CFD simulations were used to validate the NSLs. This approach provides freedom in changing the parameters, such as the properties of the fluids and g (as done for the compressible cases). The NSLs were

tested up to $\lambda = 16$. Although the use of $\lambda > 16$ is common, it was excluded to avoid an extreme change of turbulence regime by using TFs. Indeed, all the prototypes are in the fully turbulent flow regime and the TFs at $\lambda = 16$ lead to approaching laminar flow conditions such that the k-ϵ model may no longer be adequate and numerical model effects are therefore introduced next to scale effects.

The plunging jet was used to test NSLs for the incompressible case. This phenomenon is characterised by a strong air layer, therefore, surface tension plays a central role. Figures 4.10a and 4.11a demonstrate that the NSLs result in self-similarity for $\overline{U'}$ and $\overline{k'}$, i.e. these results collapse for P1, P8, P16, $\mathrm{P8_{PFs}}$ and $\mathrm{P16_{PFs}}$, while this is not the case for $\mathrm{P8_{TFs}}$ and $\mathrm{P16_{TFs}}$. The self-similarity of the distribution of the void fraction depends on the density, inertia, gravity, viscosity and surface tension. The simulation of the prototype captures the mechanism of air entrainment by a plunging jet (Figure 4.7), including the formation of an air cavity between the impinging jet and the surrounding fluid, which collapses and reforms intermittently, entraining air bubbles. At this stage, these are advected into a turbulent shear flow and they are broken into smaller bubbles creating a conical air-entrainment layer. Subsequently, buoyancy determines the re-surfacing of bubbles outside the air layer (Biń, 1993; Kiger and Duncan, 2012; Blenkinsopp and Chaplin, 2007). This is also true for the void fraction in Figure 4.9, which is a consequence of the mechanism described above. On the other hand, Figure 4.9b demonstrates that the TFs fail to reproduce the void fraction distribution. This gradually reduces with increasing λ, because surface tension and viscosity are over-represented. The results of $\mathrm{P16_{TFs}}$ in Figures 4.10b and 4.11b are affected by model effects because $\mathsf{R} = 800$ while in the prototype $\mathsf{R} = 50840$ (Hughes, 1993; Hassan et al., 2019).

The Taylor bubble is a good benchmark for testing the NSLs considering air compressibility. Indeed, the Taylor bubble is compressed by the surrounding water and the behaviour depends on the viscosity, surface tension and compressibility effects. The results of the Taylor bubble confirm a self-similar behaviour between the prototype and its scaled domains although the results do not perfectly overlap. Indeed, the models designed by using the NSLs replicate the general behaviour of the prototype T1 correctly. However, from the early stage, T16 shows a little difference with respect to T1 (Figure 4.18), although the dynamics of the transition of the bubble to the final shape is the same. This means that self-similarity at the scale of individual bubbles, with dimensions much smaller than the Taylor bubble, can not be guaranteed.

Nevertheless, there is no evidence that the small differences between T1, T4, T8 and T16 are due to scale effects. This is because the differences are not directly proportional to λ, as it is suggested by the value of $E_{U_b'}$ in Table 4.13. In contrast, the domains scaled with the TFs show a mismatch from the prototype increasing with λ (see Figure 4.20 and Table 4.13). Indeed, the viscosity and surface tension are overestimated and the compressibility of air and the related heat exchange are neglected.

The thermophysical behaviour of the Taylor bubble is represented in Figures 4.21 and 4.22. Domains T4, T8 and T16 reproduce the general behaviour of the prototype, in contrast to domains $\mathrm{T4_{TFs}}$, $\mathrm{T8_{TFs}}$ and $\mathrm{T16_{TFs}}$. Since the TFs overestimate the viscosity and the surface tension and do not account for air compressibility, the bubble is not compressed at the beginning of the simulations, and the initial variation of V' is smaller than the results with the NSLs (Figure 4.22c). Consequently, $\overline{\rho'}$ decreases suddenly in contrast to the prototype. The overestimation of the pressure effects is demonstrated in Figure 4.22c, which shows the variation in the slope of $\overline{p'}$

with increasing λ. Both the absolute and relative fluctuations of $\overline{T'}$ reduce with increasing λ, even if they are very small. In $T4_{TFs}$, $T8_{TFs}$ and $T16_{TFs}$, V' increases in time and its maximum value increases also with λ. Hence, the TFs introduce scale effects, which increase with λ. When the bubble rises, the pressure decreases such that the bubble expands while also releasing air into the wake, and V' decreases. This occurs in the prototype and the self-similar domains. Hence, domains T1, T4, T8 and T16 have more air in the wake with respect to the domains scaled with the TFs (Figure 4.19). This behaviour is shown in Figure 4.23 where the time history of the void fraction in the wake is reported. This behaviour on the viscosity, surface tension and compressibility of the bubble, which is related to the heat exchange between water and air. Hence, the same amount of void fraction behind the bubble shows that all these effects are scaled correctly. The differences between the self-similar domains are likely due to the small differences in describing individual bubbles at scales much smaller than the Taylor one, as shown in the initial stages of the motion in Figure 4.18.

The same setup of a dam break flow was used to validate both the scaling laws for incompressible and compressible air-water flows, showing that self-similarity is guaranteed. In the incompressible case, the dam break flow shows a significant deformation of the free surface after the impact with the obstacle, with a characteristic water tongue projected downstream of the obstacle. After $t' = 2.7$, the water tongue collapses and the flow is reflected at the downstream wall. This behaviour is captured in all the domains scaled with the NSLs as shown in Figure 4.2. Figure 4.3 shows also that k' is the same by using the NSLs and k is thus self-similar. The phase fraction γ is also self-similar. This is a strong indication that the surface tension effects are self-similar as well (Figure 4.4), which is also true for the domains $D8_{PFs}$ and $D16_{PFs}$ since the PFs are a special case of

the NSLs.

On the other hand, the commonly applied TFs, relying on the same fluids as in the prototype, fail to reproduce the behaviour of the prototype. Indeed, Figures 4.2d and 4.6e show that the water tongue is not well predicted. Scale effects are observed in k' and γ at point RW. Furthermore, the flow reaches point RW later than in the prototype with increasing λ. Scale effects are also observed after the flow is re-reflected by the downstream wall, particularly at the second peak of k'.

In the dam break test case where the air is considered compressible, the behaviour of the prototype CD1 is also well captured by the domains scaled by using the NSLs. This is confirmed by the snapshots in Figure 4.12 and by the fact that the time histories of k' and γ at point RW of CD1, CD8 and CD16 overlap (Figures 4.13 and 4.14). This is an indication that surface tension and the compressibility effects are well scaled, similarly to the incompressible case.

The comparison between the compressible and incompressible cases allows to discuss the role of air compressibility in dam break flows interacting with obstacles. A direct influence of air compressibility can be seen in the time history of p'_{rel} showing a strong oscillation with a range of 0.40-0.65 at $t' = 5$ (Figures 5.1 and 4.15). After the air pocket forms between the falling water tongue and the upstream side of the obstacle, it starts to shrink and subsequently expands due to the lateral air leakage. This results in a pressure oscillation, which cannot be fully captured by assuming air as incompressible (Figure 5.1). The oscillation of p'_{rel} is clearer in Figure 5.2, that shows the time histories of p'_{rel} for D1 and CD1 at point DO located downstream of the obstacle (see insert in Figure 5.2) where the air pocket is entrapped (see Figures 4.6 and 4.16). It is worth noting that

this behaviour is also shown in laboratory experiments, indicating that the air-compressibility plays a central role (see Figure 11 in Ma et al., 2016).

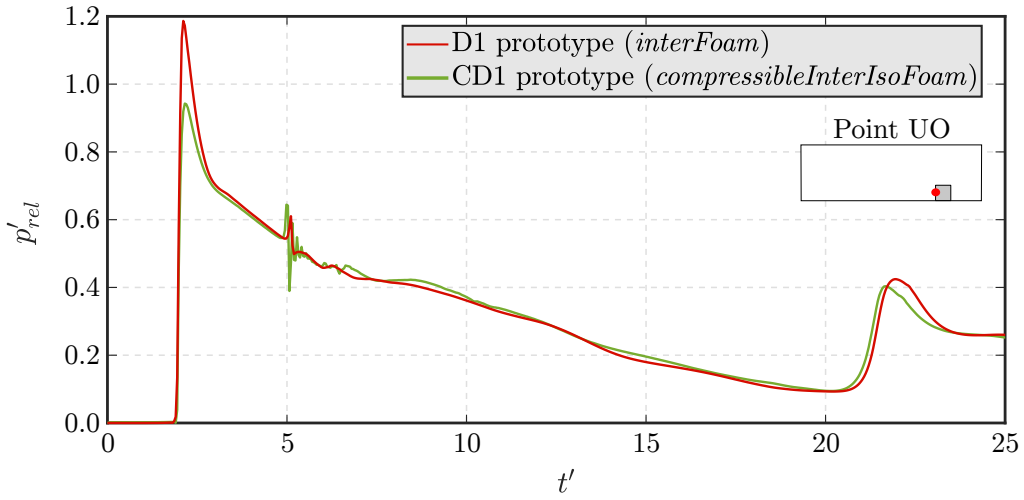


Figure 5.1: p'_{rel} time histories in the dam break flow at point UO for domains D1 and CD1.

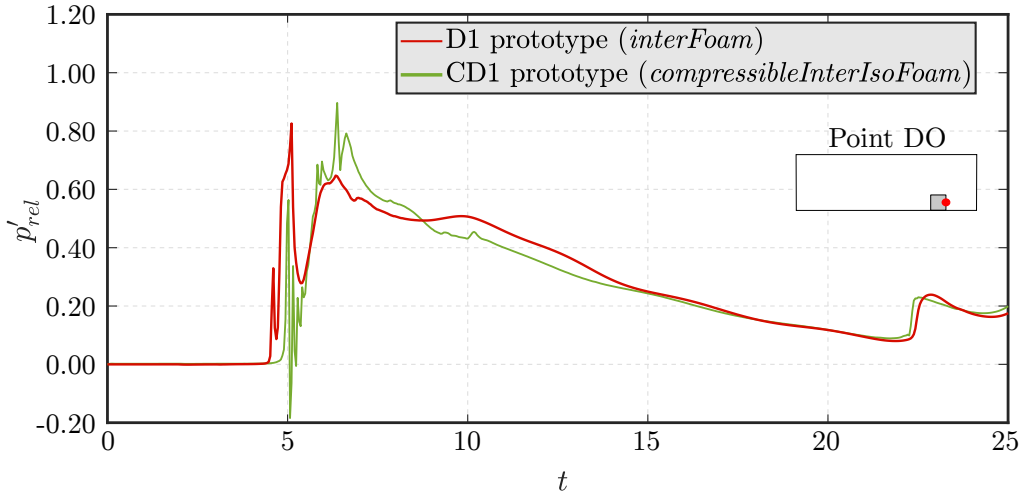


Figure 5.2: p'_{rel} time histories in the dam break flow at point DO for domains D1 and CD1.

The oscillation of p'_{rel} is perfectly replicated by CD8 and CD16 (Figure 4.15), indicating that the compressibility effects are scaled correctly by using the NSLs for compressible air-water flows. This is not true for the domains scaled with the TFs. Indeed, the oscillation of p'_{rel} is over-estimated in CD8_{TFs} with respect to the prototype and it is under-estimated in CD16_{TFs}. This may be due to the entrapped air pocket in CD16_{TFs} being smaller since the viscosity effects are over-estimated (Figure 4.16).

5.4 Implications for laboratory experiments

The use of the NSLs for scaling fluid properties requires the modification or replacement of ordinary water in laboratory experiments, e.g. for values of λ comparable with the largest used herein, i.e. $\lambda = 16$, $\rho_w = 62.5$ kg/m^3, $\nu_w = 1.56\times10^{-8}$ m^2/s and $\sigma = 1.70\times10^{-5}$ N/m are required (Tables 4.4 and 4.7). There are options to alter the relevant fluid properties; they can be changed by adding ethanol into water (Stagonas et al., 2011; Khattab et al., 2012). Another option is to increase the water temperature in the model leading to a decrease of ρ, ν and σ. A more recent approach to change the water properties is based on nano-fluids, i.e. nano-particles are added to water (Lu et al., 2014; Xu et al., 2013). The effects on the fluid properties depend on the type on nano-particles. Hydrophobic nano-particles, such as titanium dioxide, tend to stay on the free surface and they behave like a surfactant to reduce the surface tension. By adding 1% of nano-particles (15 nm diameter) of titanium dioxide (TiO_2) in water, the surface tension is 0.069 N m^{-1} (Radiom et al., 2010). On the other hand, hydrophilic nano-particles, such as aluminium trioxide, are immersed and impose strong attractive forces on the water molecules at the free surface which increases the surface tension of the nano-fluid. For example, the surface tension of water with 0.1 g l^{-1} of aluminum trioxide (Al_2O_3) increases by about 3.4% (Zhu et al., 2010).

The NSLs for compressible air-water flows require also the modification of g in the scaled models. The scaling configuration used in Section 4.3 is written in terms of α_x, $\alpha_R = \alpha_T = \alpha_{Mm} = 0$ and $\alpha_n = 3\alpha_x$ leading to $\alpha_g = -\alpha_x$ and g should therefore be increased in the model (see Table 4.9). This can be obtained, for example, by conducting experiments in a centrifuge. Although not common, centrifuges are sometimes used in

hydraulics, e.g. Zhang et al. (2009) conducted a series of centrifuge model tests to examine the responses of a caisson breakwater on sand subject to breaking-wave impacts reaching a gravitational acceleration of $100g$.

An advantage of the NSLs is their flexibility, meaning that different configurations of the NSLs can be found in order to match the laboratory conditions. For this purpose, a MATLAB app to derive different configurations of the NSLs for air-water flows has been developed (http://doi.org/10.17639/nott.7244). This app allows for the generation of different configurations by setting assumptions for air compressibility, the scaling parameter β and the values in the scaled model of the three fixed parameters, i.e. those for which the values in the model are known. Hence, by setting the water properties in the prototype and those of a hypothetical fluid in the model, a self-similar configuration is found (a user guide of the MATLAB app is presented in Appendix B). For example, by increasing the water temperature and neglecting the air compressibility, the scaling configuration for incompressible air-water flows can be found. The water at 293.00 K has $\rho = 998.7$ k m^{-3}, $\nu = 1.00 \times 10^{-6}$ m^2 s^{-1} and $\sigma = 0.073$ N m^{-1}, i.e. the values of the prototype. Water at 338.15 K has $\rho = 980.6$ k m^{-3}, $\nu = 4.42 \times 10^{-7}$ m^2 s^{-1} and $\sigma = 0.06536$ N m^{-1}, i.e. in the model. These values can be added in the MATLAB app in the corresponding boxes of the prototype and model, meaning that ρ, ν and σ are fixed (Figure 5.3).

By choosing a value of β (for example, $\beta = 8$), the new configuration can be generated by clicking on "Generate scaling laws" (Figure 5.4). This configuration is written in term of $\alpha_\rho = 0.0088$, $\alpha_\nu = 0.39$ and $\alpha_\sigma = 0.053$ and thus $\alpha_x = 0.74$, $\alpha_t = 1.09$ and $\alpha_g = -1.44$. Hence, the prototype would be at room temperature with still water and $g = 9.81$ m s^{-1} while the scaled model would be 4.71 times smaller ($\lambda = \beta^{\alpha_x} = 4.71$) with the fluid properties corresponding to those of the water at 338.15 K and $g = 195.84$

m s^{-2}, which can be reached by using a centrifuge. Although $\lambda = 4.71$ could be regarded as small, in some cases the use of the TFs at $\lambda = 3.6$ shows a decrease of the maximum value of void fraction between 10% and 30% (Chanson et al., 2004). Further, λ can be increased by finding a new configuration with a higher temperature in the model.

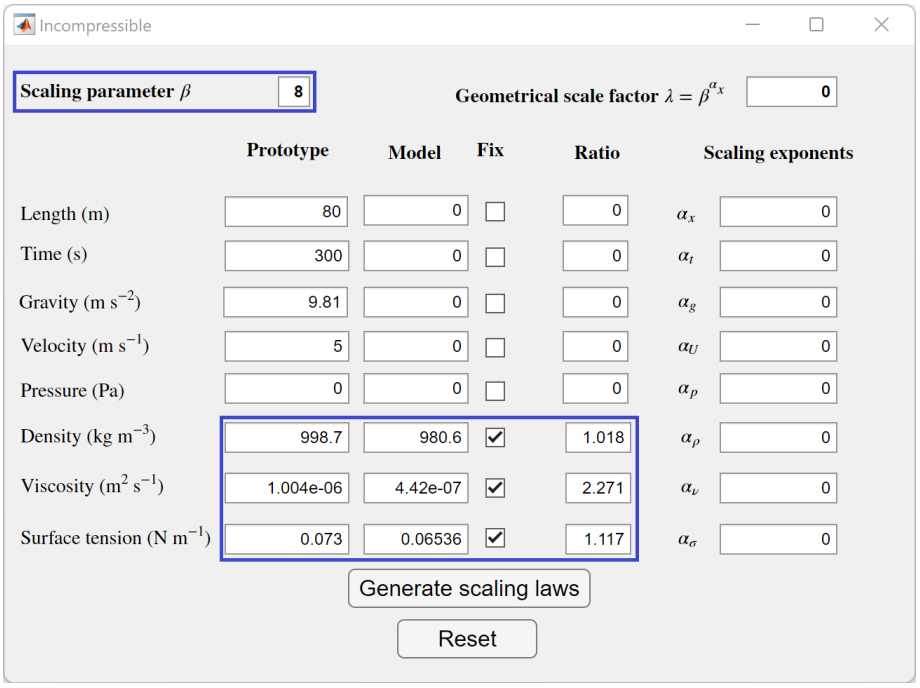


Figure 5.3: GUI of the MATLAB app. The inputs to obtain the scaling configuration based on the properties of the water at 338.15 K are highlighted.

It is worth noting that, in this example, the change of T between the model and its prototype involves changing the fluid properties and the compressibility of air is not considered. Indeed, the fixed parameters for incompressible air-water flows are three, while five parameters have to be fixed to find configurations including air compressibility. The implementation in the laboratory environment needs further research but the NSLs and the MATLAB app permit the exploration of different options.

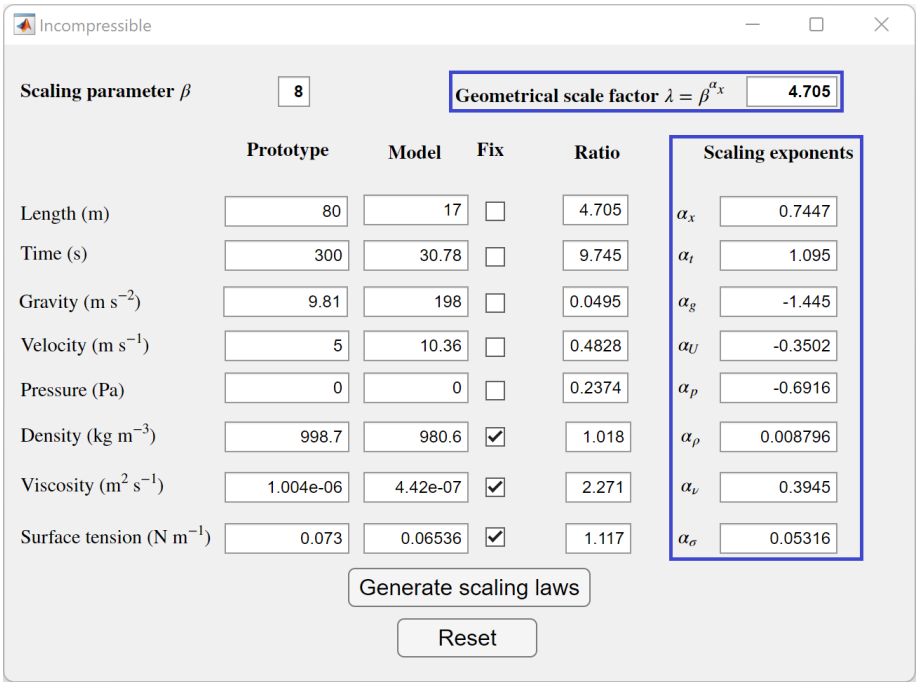


Figure 5.4: GUI of the MATLAB app. The scaling exponents of the configuration based on the properties of water at 338.15 K are highlighted.

5.5 Summary

This chapter addressed theoretical aspects of the NSLs, a discussion on the results of the test cases and the implication of laboratory models. It has been shown that the NSLs for compressible air-water flows are the same as for incompressible ones with the addition of the equations of heat transfer and the perfect gas. The differences between the two NSLs arise when restrictions are applied. Further, the TFs are a specific configuration of the NSLs which are derived from the governing equations.

The numerical simulations demonstrated that the simulated phenomena are correctly scaled by also considering the compressibility of air. Indeed, the results from the dam break flow overlap in dimensionless form for both the incompressible and compressible cases, meaning that the models are self-similar with respect to the prototype. The dimensionless relative pressure

shows an oscillation when the compressibility of air is taken into account. This behaviour is due to an air pocket downstream the obstacle. This air pocket is compressed by the water and then expands due to the lateral air leakage, creating strong oscillations of p'_{rel} (Figures 5.1 and 5.2).

The modelling of the plunging jet designed with the NSLs confirm the self-similarity of the incompressible NSLs and the Taylor bubble results confirm the self-similarity of the compressible scaling laws. The small differences observed between the scaled models and the prototype for this case are not due to scale effects, but rather due to the differences in describing the motion of individual bubbles that have dimensions much smaller than the Taylor one. In contrast, the simulations based on the TFs introduce scale effects proportional to the geometrical scale factor, showing a distinct behaviour with respect to the prototype and those obtained with the NSLs.

The main advantage of the NSLs is the flexibility, meaning that different configurations can be achieved to adapt them to the laboratory conditions and vice versa. Therefore, fluids with different properties can be used in the laboratory to match the conditions of the NSLs. This implies that fluids of different density, viscosity and surface tension than water, e.g. water at different temperatures, now also qualify as potential candidates for laboratory experiments.

A MATLAB app has been developed to find different configurations of the incompressible and compressible NSLs. The laboratory conditions can be added as input to this app that returns the scaling exponents of the scaling configuration that guarantee self-similarity under the selected conditions. By illustrating how the MATLAB app works, it is also shows how to find a configuration of the NSLs by knowing the laboratory conditions.

Chapter 6

Conclusions and future work

6.1 Conclusions

The Froude scaling laws have been applied to model free surface water flows at reduced size for almost a century. They ensure that the square root of the ratio between the inertial and gravity force, namely the Froude number F, is the same in the model and in nature, i.e. the prototype. A significant disadvantage of the Froude scaling laws is the potential for scale effects, especially for flows involving air entrainment, e.g. air bubble entrainment into water flows (air-water flows). For these, density, viscosity and surface tension between water and air play a role such that F, the Reynolds number R (inertial force to viscous force) and the Weber number W (inertial force to surface tension force) are all important. Furthermore, the Froude scaling laws do not account for the effects of air compressibility and heat transfer and additional scale effects are therefore potentially introduced.

This research was aimed at deriving and testing the novel scaling laws (NSLs) for incompressible and compressible air-water flows based on self-

similarity of the governing equations, such that scale effects are avoided. The principle followed is that the scaling of an object following suitable laws results in a self-similar scaled copy of itself and a self-similar process is scale-invariant. The NSLs were analytically derived by using the one-parameter Lie group of point scaling transformations (Lie group transformations). These are mathematical transformations composed of a scaling parameter β and a list of scaling exponents for each parameter of the governing equation. Lie group transformations were originally used to reduce the number of independent variables of an initial boundary value problem. Subsequently, the Lie group transformations were used to derive the conditions under which various hydrological processes are self-similar through the change in size.

This study aim was achieved by applying the Lie group scaling method to the Reynolds-averaged Navier–Stokes (RANS) equations including the surface tension and air compressibility. First, the Lie group transformations were applied to the RANS equations where the surface tension was added as a source term, considering both the fluids incompressible. Then, the air was considered compressible and the Lie group transformations were applied also to the equations of heat transfer and perfect gas.

Hence, some parameters can be fixed following the values that are available in the laboratory, i.e. in the model. In this study, for the incompressible air-water case, the gravitational acceleration was kept constant between the model and its prototype. This means that the scaling exponents for the gravitational acceleration was fixed, i.e. $\alpha_g = 0$ and the rest of the scaling exponents are written in terms of the scaling exponent for the length α_x, the scaling exponent for the density α_ρ and $\alpha_g = 0$. Further, the Froude scaling laws where the properties of fluids are strictly scaled (precise Froude scaling laws, PFs) were proved to be a particular configuration of the NSLs

where the density and the gravitational acceleration are kept constant, i.e. α_x, $\alpha_\rho = 0$ and $\alpha_g = 0$.

When air is considered compressible, some restrictions on the scaling exponents were taken into account because the temperature cannot be reduced below the freezing point and the molar mass, as well as the molar density, needed to be the same in the prototype and the scaled model. Hence, the used scaling configuration was expressed as a function of the scaling exponents of the length α_x, the specific gas constant $\alpha_R = 0$, the temperature $\alpha_T = 0$, the molar mass $\alpha_{M_m} = 0$ and the number of moles $\alpha_n = 3\alpha_x$.

The derived NSLs were validated with computational fluid dynamics (CFD) simulations of air–water flows phenomena: (i) a dam break flow interacting with an obstacle modelled both with the incompressible and compressible-air, (ii) a plunging water jet with both fluids modelled as incompressible and (iii) a Taylor bubble with the air modelled compressible. The simulations were carried out by using *interFoam* for the incompressible case and *compressibleInterIsoFoam* for the air-compressible one, i.e. two-phase solvers based on the volume of fluid method available in the OpenFOAM v.1706 CFD package.

The results of the plunging water jet show that the NSLs for incompressible air-water flows guarantee self-similarity. Indeed, they show perfect agreement at different scales for air entrainment and kinematic properties. The results of the PFs demonstrate that this is a particular configuration of the NSLs. In contrast, the simulations based on Froude scaling using ordinary water and air (traditional Froude scaling laws, TFs), as it is common in laboratory studies, show significant scale effects, as expected.

The results from the Taylor bubble simulation show that the general behaviour of the phenomenon involving compressible air is correctly scaled.

Small differences observed between the models and the prototype are not due to scale effects, rather due to the divergences in describing the motion of individual bubbles that have dimensions much smaller than the Taylor one. On the other hand, the TFs introduce scale effects proportional to the geometrical scale factor, showing a distinct behaviour with respect to the prototype and that obtained with the NSLs.

By applying the NSLs to the dam break flow, perfect self-similarity of the results is confirmed for both the incompressible and compressible air cases. Further, by comparing the dam break simulated using the two assumptions for air, the effects of air compressibility can be seen. In the latter case, the history of the dimensionless pressure shows oscillations caused by air pocket between the falling water tongue and the obstacle.

The NSLs proved to be more universal and flexible than the Froude scaling laws because different scaling configurations can be obtained to adapt them to laboratory conditions. Indeed, this flexibility can be exploited to find the use in the models of fluid having different properties than water. To this end, a MATLAB app was developed aimed at finding different scaling configurations by adding the laboratory conditions (i.e. the properties of fluids or the gravitational acceleration) as input.

6.2 Outlook

The application of the NSLs to design a scaled laboratory model of air-water flows may be addressed in future work. Indeed, the flexibility of the NSLs can be used to adapt them to the laboratory conditions. Hence, suitable fluids satisfying the NSLs should be identified. This can be done, e.g. by increasing the temperature of water in the scaled model or by

adding ethanol into water. Moreover, the use of nano-particles could open several options because the behaviour of nano-fluids can be totally different depending on the size and type of nano-particles.

Some proposed scaling configurations imply that the gravitational acceleration g needs to be changed in the model. This can be achieved by using a centrifuge to increase g. On the other hand, vertical accelerator can be used to decrease g. Hence, a combination of changing the properties of the fluids and g can lead to the design of self-similar scaled models of air-water flows.

Alternatively, future work could focus on finding other scaling configurations, e.g. the application of the Lie group scaling method to compressible air-water flows under adiabatic conditions. The Lie group scaling method can be applied to any phenomena where the governing equations are known. Indeed, if a set of governing equations can describe correctly a phenomenon, the application of the Lie group scaling method can capture all the aspects of the phenomenon under investigation and self-similarity is therefore guaranteed.

Appendix A

Influence of the numerical scheme on the test of the NSLs

In order to model incompressible air-water flows, *interFoam* computes the RANS equations and the k-ϵ turbulence model. When air is considered compressible, also the equations of heat transfer and perfect gas need to be solved and *compressibleInterIsoFoam* is therefore used. Both the solvers used in this work are based on the volume of fluid (VOF) method in which the resolution of the free surface depends on the size of the cells (see Section 3.4). Therefore, a numerical scheme is needed to keep the interface sharp. In *interFoam*, the implemented scheme is MULES (Multidimensional Universal Limiter with Explicit Solution, Deshpande et al., 2012). More recent, interface schemes are found to be more efficient than MULES for flows with larger curvatures (Roenby et al., 2016), such as *isoAdvector* based on iso-surfaces, which is the one used in *compressibleInterIsoFoam* for compressible air-water flows.

In this Appendix A, the question of whether the test of the NSLs is influenced by the interface scheme is addressed (Catucci et al., 2022a). For this

purpose, the test is carried out by simulating the dam-break flow investigated in Section 4.2.1, using *interIsoFoam*, i.e. an incompressible two-phase solver using *isoAdvector* as interface scheme to be compared to the MULES results. The NSLs for incompressible air are applied in Section 4.2.1. If the dimensionless results between the prototype and the scaled models overlap, self-similarity is guaranteed regardless of the interface numerical scheme, as expected.

The setup of the prototype $D1_{iso}$ is presented in Section 4.2.1. The scaled domains $D8_{iso}$ ($\lambda = \beta^{\alpha_x} = 8$) and $D16_{iso}$ ($\lambda = \beta^{\alpha_x} = 16$) were designed by using the scaling configuration in terms of α_x, α_ρ and $\alpha_g = 0$ (fourth and fifth columns of Table 3.2). The specific values of the parameters for the prototype and the scaled models, obtained by applying the conditions in Table 4.3, are presented in Table 4.4.

Figure A.1 shows the snapshots of the prototype and the scaled domains at $x_2' = 0$ and dimensionless time $t' = 2.7$. The water tongue in the prototype creates some drops in contrast to D1 (Figure 4.2). These differences exist because MULES, in contrast to *isoAdvector*, uses an artificial compression velocity to keep the interface sharp, therefore introducing a spurious velocity at the interface (Roenby et al., 2016).

The self-similarity between $D1_{iso}$, $D8_{iso}$ and $D16_{iso}$ is preserved since the shape of the water tongue is the same by increasing λ and the $RMSE'_U$ values for $D8_{iso}$ and $D16_{iso}$ are 6.85×10^{-3} and 6.63×10^{-3}, respectively. Figure A.2(a) shows the variation of k' and Figure A.2(b) of γ at point RW. The self-similarity is affirmed by the fact that the curves perfectly overlap.

This shows that the test of the NSLs holds also for a different interface scheme. Indeed, the dimensionless results between the prototype and scaled models are identical within the tests using interFoam (MULES) or *interIso-*

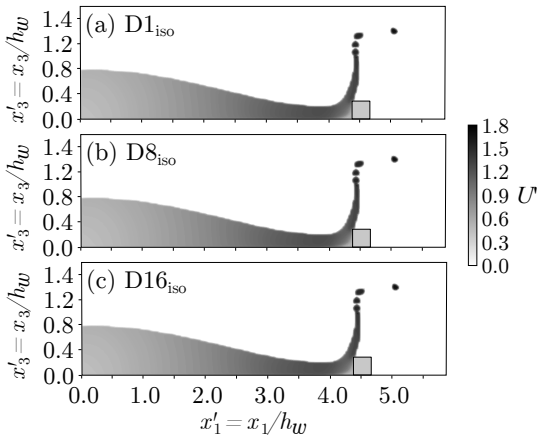


Figure A.1: Snapshots of the dam break flow simulated by using *interIsoFoam* at the cross-section $x_2' = 0$ and dimensionless time $t' = 2.7$ of the (a) domain $D1_{iso}$ and scaled with the NSLs at the domains (b) $D8_{iso}$ and (c) $D16_{iso}$, respectively (Catucci et al., 2022a)

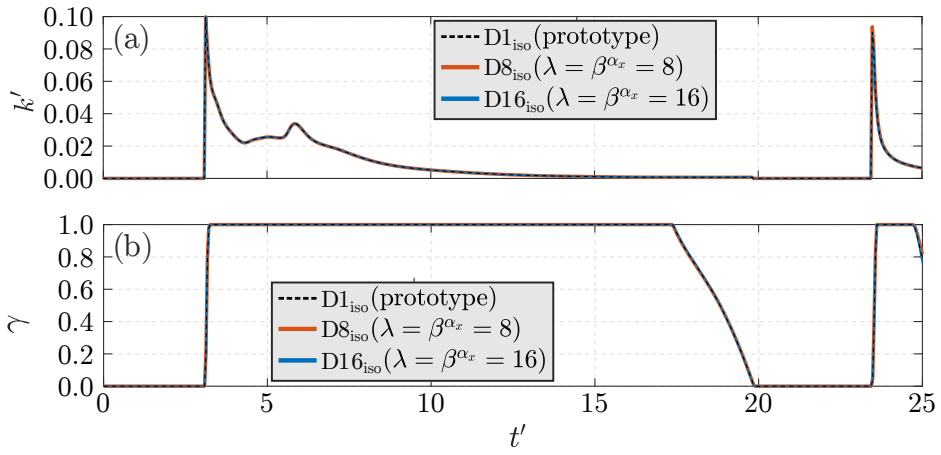


Figure A.2: Time histories of (a) k' and (b) γ in the dam break flow at point RW for domains $D1_{iso}$, $D8_{iso}$ and $D16_{iso}$ (Catucci et al., 2022a).

Foam (*isoAdvector*). This is because the NSLs are based on the governing equations and the numerical schemes do not introduce any additional variables or parameters. This means that the numerical test shown in Section 4 is robust in relation to the selected numerical scheme to keep the interface sharp.

Appendix B

MATLAB app user guide

The MATLAB app presented in Section 5.4 allows to find different scaling configurations of the NSLs for incompressible and compressible air-water flows. In this Appendix B a short user guide is presented.

In order to lunch the MATLAB app in Windows machine, **NSL_app_Installer.exe** needs to be installed from the path myPath/scalingGenerators/ (myPath is the personal directory where the downloaded folder is located). Once the installation is complete, the scaling generator app can be lunched from the path myPath/scalingGenerators/.

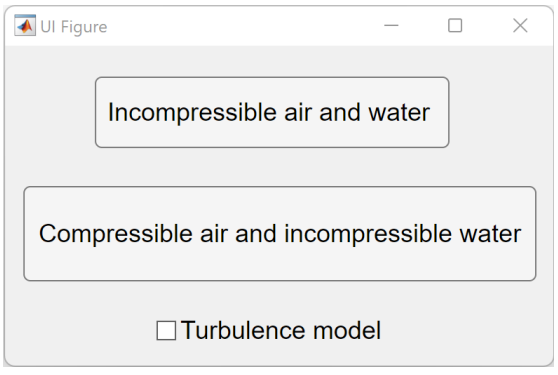


Figure B.1: Home window of the MATLAB app.

On the home window (Figure B.1), select **Turbulence model** to include

the computation of the scaling exponents for the k-ϵ turbulence model. Then click on **Incompressible air and water** to open the window for the incompressible scaling laws including the k-ϵ turbulence model (Figure B.2). Three parameters have to be fixed, otherwise an error occurs. To find the scaling configuration used in Section 4.2, enter the following data:

- Scaling parameter β: 16
- Length: prototype 0.55 m and model 0.03438 m (the height of the water column)
- Gravity: prototype 9.81 m s^{-2} and model 9.81 m s^{-2}
- Density: prototype 1000 kg m^{-3} and model 62.5 kg m^{-3}

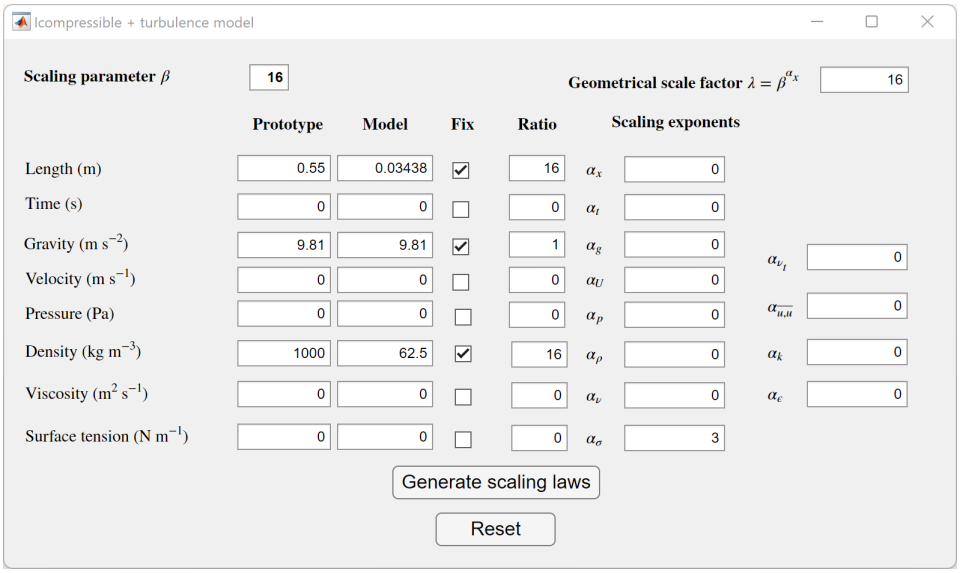


Figure B.2: Window for the scaling laws for incompressible air with the input to obtain the scaling configuration written in terms of α_x, $\alpha_g = 0$ and α_ρ.

The length, gravity and density can be fixed by clicking on the related checkbox labeled **Fix** and the scale factors (**Ratio**) will be calculated. In this case, the scale factors for the length $\beta^{\alpha_x} = \lambda$ and ρ are 16 while g is kept constant between the model and the prototype and its scaling exponent $\alpha_g = 0$.

Click on **Generate scaling laws** to calculate the values of the scaling exponents for all parameters (Figure B.3). The resulting configuration is the one written in terms of α_x, $\alpha_g = 0$, α_ρ and $\lambda = 16$ (Table 3.1).

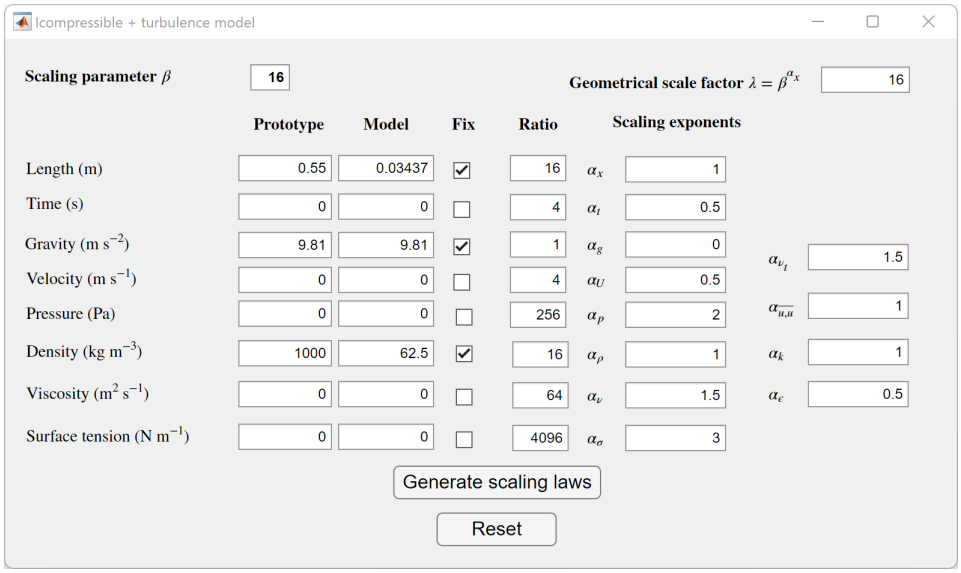


Figure B.3: GUI for the NSLs for incompressible air with the resulting scaling configuration written in terms of α_x, $\alpha_g = 0$ and α_ρ.

To open the window for the compressible air case, **Compressible air and incompressible water** need to be selected in the home window (Figure B.4). To generate a scaling configuration, five parameters have to be fixed. For example, to generate the scaling configuration used in Section **??** enter the data as listed below:

- Scaling parameter β: 16
- Length: prototype 0.55 m and model 0.03438 m (the height of the water column)
- Density: prototype 1000 kg m^{-3} and model 1000 kg m^{-3}
- Temperature: prototype 293 K and model 293 K
- Molar mass: prototype 0.289 kg mol^{-1} and model 0.289 kg mol^{-1}

- Specific gas constant: prototype 287 J kg^{-1} K^{-1} and model 287 J kg^{-1} K^{-1}

The same ρ and M_m between the prototype and the water results in the same conditions of $\alpha_n = 3\alpha_x$, see Eq. (3.78).

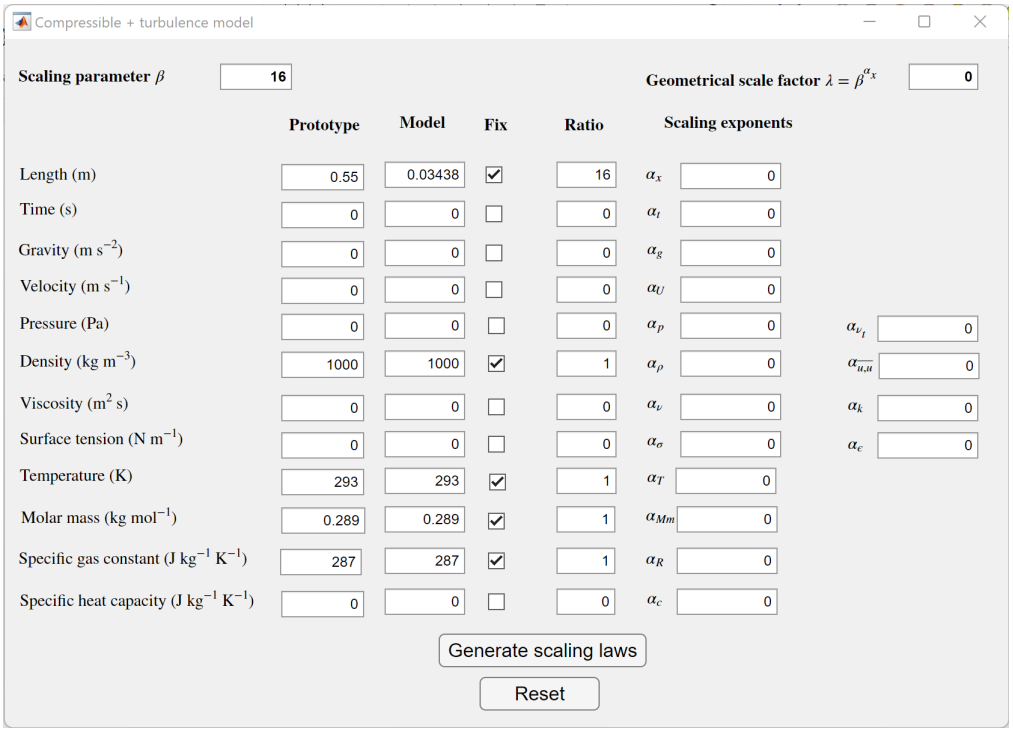


Figure B.4: GUI for the NSLs for compressible air with the input to obtain the scaling configuration written in terms of α_x, $\alpha_T = \alpha_{Mm} = \alpha_R = 0$ and $\alpha_n = 3\alpha_x$ ($\alpha_\rho = 0$).

Click on the checkbox labelled **Fix** for the length, density, temperature, molar mass and the specific gas constant. This means that the five parameters are fixed, therefore, the resulting configuration is written in terms of α_x, $\alpha_T = \alpha_{Mm} = \alpha_R = 0$ and $\alpha_n = 3\alpha_x$ ($\alpha_\rho = 0$) and the scaling exponents can be calculated by clicking on **Generate scaling laws** (Figure B.5).

Note that when two conditions that cannot be both satisfied simultaneously are fixed, an error occurs and a error message appears. For example, by keeping invariant the temperature and the specific gas constant $\alpha_t = \alpha_x$ and by keeping invariant the gravity $\alpha_t = 0.5\alpha_x$. These two conditions are

therefore in conflict, meaning that the relationships of the scaling exponents resulting from the application of the Lie group scaling method are not satisfied (see Section 3.3.2). Hence, the resulting configuration is not self-similar and the dialogue box in Figure B.6 will appear.

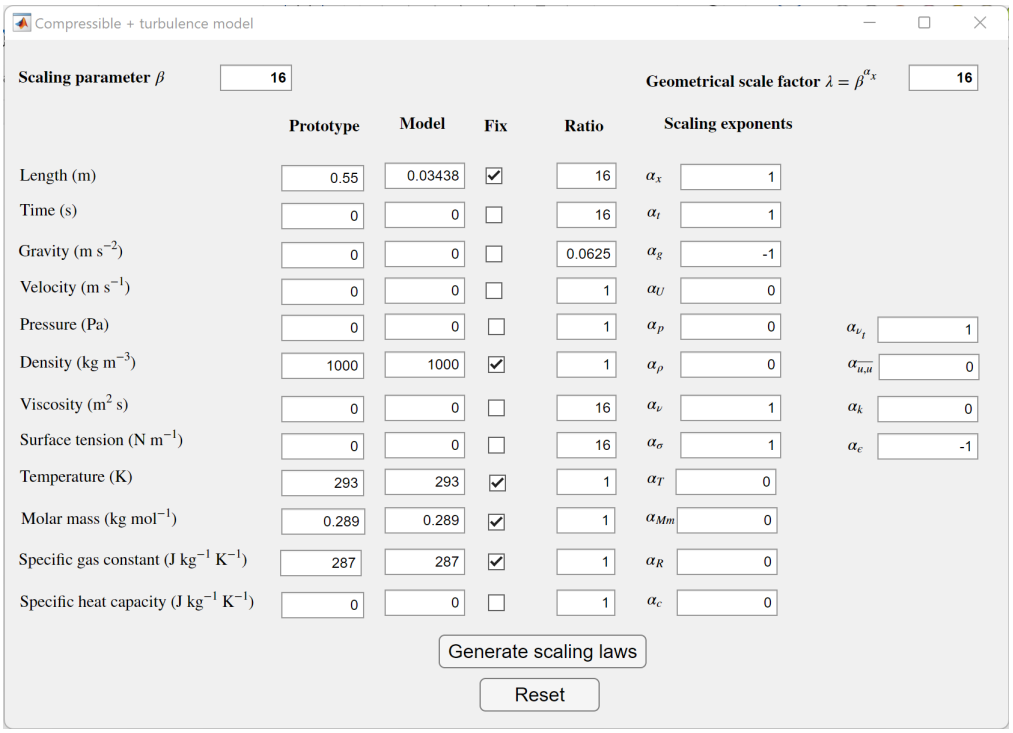


Figure B.5: Window for the scaling laws for compressible air with the resulting scaling configuration written in terms of α_x, $\alpha_T = \alpha_{Mm} = \alpha_R = 0$ and $\alpha_n = 3\alpha_x$ ($\alpha_\rho = 0$).

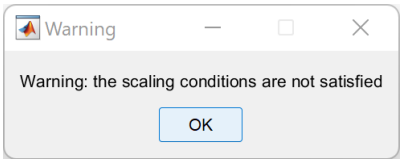


Figure B.6: Error message due to the selection of two or more conditions that cannot both be satisfied simultaneously.

References

Ali, S. Z. and Dey, S. (2017). Origin of the scaling laws of sediment transport. *Proceedings of the Royal Society A: Mathematical, Physical and Engineering Sciences*, 473(2197):20160785.

Ambrose, S., Hargreaves, D. and Lowndes, I. (2016). Numerical modeling of oscillating Taylor bubbles. *Engineering Applications of Computational Fluid Mechanics*, 10(1):578–598.

AMCAN86, A. M. C. (2019). Revision of the international system of units (background paper). *Royal Society of Chemistry*, 11(12):1577–1579.

Ashgriz, N. and Mostaghimi, J. (2002). An introduction to computational fluid dynamics. *Fluid flow handbook*, 1:1–49.

Bagnold, R. (1939). Interim report on wave-pressure research (includes plates and photographs). *Journal of the Institution of Civil Engineers*, 12(7):202–226.

Barenblatt, G. I. (1996). *Scaling, self-similarity, and intermediate asymptotics: dimensional analysis and intermediate asymptotics*. Cambridge, UK: Cambridge University Press.

Barenblatt, G. I. (2003). *Scaling (Vol. 34)*. Cambridge, UK: Cambridge University Press.

Biń, A. K. (1993). Gas entrainment by plunging liquid jets. *Chemical Engineering Science*, 48(21)(21):3585–3630.

Blenkinsopp, C. and Chaplin, J. (2007). Void fraction measurements in breaking waves. *Proceedings of the Royal Society A: Mathematical, Physical and Engineering Sciences*, 463(2088):3151–3170.

Boualouache, A., Zidouni, F. and Mataoui, A. (2018). Numerical visualization of plunging water jet using volume of fluid model. *Journal of Applied Fluid Mechanics*, 11(1):95–105.

Brackbill, J. U., Kothe, D. B. and Zemach, C. (1992). A continuum method for modeling surface tension. *Journal of Computational Physics*, 100(2):335–354.

Bredmose, H., Bullock, G. and Hogg, A. (2015). Violent breaking wave impacts. Part 3. Effects of scale and aeration. *Journal of Fluid Mechanics*, 765:82–113.

Bullock, G., Crawford, A., Hewson, P., Walkden, M. and Bird, P. (2001). The influence of air and scale on wave impact pressures. *Coastal Engineering*, 42(4):291–312.

Carosi, G. and Chanson, H. (2006). Air-water time and length scales in skimming flows on a stepped spillway: Application to the spray characterisation. *Report No. CH59/06. Division of Civil Engineering, The University of Queensland, Brisbane, Australia.*

Carr, K., Ercan, A. and Kavvas, M. (2015). Scaling and self-similarity of one-dimensional unsteady suspended sediment transport with emphasis on unscaled sediment material properties. *Journal of Hydraulic Engineering*, 141(5):04015003.

Catucci, D., Briganti, R. and Heller, V. (2021). Numerical validation of novel scaling laws for air entrainment in water. *Proceedings of the Royal Society A*, 477(2255):20210339.

Catucci, D., Briganti, R. and Heller, V. (2022a). Analytical and numerical study of novel scaling laws for air-water flows. *39th IAHR World Congress*, 4551–4560.

Catucci, D., Briganti, R. and Heller, V. (2022b). Numerical validation of novel scaling laws for air-water flows including compressibility and heat transfer. *Journal of Hydraulic Research*, Conditionally accepted.

Chanson, H. (2004a). Air-water flows in water engineering and hydraulic structures. Basic processes and metrology. In *Proceedings of international conference on hydraulics of dams and river structures*, Tehran, Iran. Springer.

Chanson, H. (2004b). *Environmental hydraulics for open channel flows*. Oxford, UK: Elsevier Butterworth-Heinemann.

Chanson, H. (2009a). Current knowledge in hydraulic jumps and related phenomena. A survey of experimental results. *European Journal of Mechanics-B/Fluids*, 28(2):191–210.

Chanson, H. (2009b). Turbulent air–water flows in hydraulic structures: dynamic similarity and scale effects. *Environmental fluid mechanics*, 9(2)(2):125–142.

Chanson, H., Aoki, S. and Hoque, A. (2004). Physical modelling and similitude of air bubble entrainment at vertical circular plunging jets. *Chemical Engineering Science*, 59(4):747–758.

Chanson, H., Aoki, S. and Maruyama, M. (2002). Unsteady air bubble entrainment and detrainment at a plunging breaker: dominant time

scales and similarity of water level variations. *Coastal Engineering*, 46(2):139–157.

Chanson, H. and Chachereau, Y. (2013). Scale effects affecting two-phase flow properties in hydraulic jump with small inflow Froude number. *Experimental Thermal and Fluid Science*, 45:234–242.

Chanson, H. and Felder, S. (2007). Dynamic similarity and scale effects in turbulent free-surface flows above triangular cavities. In *Proceedings of the 16th Australasian Fluid Mechanics Conference, 16AFMC*, pages 691–698. School of Engineering, The University of Queensland.

Chung, T. J. (2002). *Computational fluid dynamics*. Cambridge University Press.

Courant, R., Friedrichs, K. and Lewy, H. (1967). On the partial difference equations of mathematical physics. *IBM Journal of Research and Development*, 11(2):215–234.

Cummings, P. D. and Chanson, H. (1997). Air entrainment in the developing flow region of plunging jets—part 1: Theoretical development. *Journal of Fluids Engineering*, 119(3):597–602.

Cuomo, G., Allsop, W. and Takahashi, S. (2010). Scaling wave impact pressures on vertical walls. *Coastal Engineering*, 57(6):604–609.

Davies, R. M. and Taylor, G. I. (1950). The mechanics of large bubbles rising through extended liquids and through liquids in tubes. *Proceedings of the Royal Society of London. Series A. Mathematical and Physical Sciences*, 200(1062):375–390.

Deshpande, S. S., Anumolu, L. and Trujillo, M. F. (2012). Evaluating the performance of the two-phase flow solver interFoam. *Computational Science & Discovery*, 5(1):014016.

Duncan, J., Philomin, V., Behres, M. and Kimmel, J. (1994). The formation of spilling breaking water waves. *Physics of Fluids*, 6(8)(8):2558–2560.

Ercan, A. and Kavvas, M. L. (2015a). Scaling and self-similarity in two-dimensional hydrodynamics. *Chaos: An Interdisciplinary Journal of Nonlinear Science*, 25(7):075404.

Ercan, A. and Kavvas, M. L. (2015b). Self-similarity in incompressible Navier-Stokes equations. *Chaos: An Interdisciplinary Journal of Nonlinear Science*, 25(12):123126.

Ercan, A. and Kavvas, M. L. (2017). Scaling relations and self-similarity of 3-dimensional Reynolds-averaged Navier-Stokes equations. *Scientific Reports*, 7(1):6416.

Ercan, A., Kavvas, M. L. and Haltas, I. (2014). Scaling and self-similarity in one-dimensional unsteady open channel flow. *Hydrological Processes*, 28(5):2721–2737.

Ettema, R. (2000). Hydraulic modeling: Concepts and practice. American Society of Civil Engineers.

Ettema, R. and Muste, M. (2004). Scale effects in flume experiments on flow around a spur dike in flatbed channel. *Journal of Hydraulic Engineering*, 130(7):635–646.

Falcão, A. F. and Henriques, J. C. (2014). Model-prototype similarity of oscillating-water-column wave energy converters. *International Journal of Marine Energy*, 6:18–34.

Falcão, A. F. and Henriques, J. C. (2019). The spring-like air compressibility effect in oscillating-water-column wave energy converters: Review

and analyses. *Renewable and Sustainable Energy Reviews*, 112:483–498.

Felder, S. and Chanson, H. (2009). Turbulence, dynamic similarity and scale effects in high-velocity free-surface flows above a stepped chute. *Experiments in Fluids*, 47(1):1–18.

Frisch, U. (1995). *Turbulence: the legacy of AN Kolmogorov*. Cambridge, UK: Cambridge University Press.

Hager, W. H. and Castro-Orgaz, O. (2017). William Froude and the Froude number. *Journal of Hydraulic Engineering*, 143(4):02516005.

Hager, W. H., Schleiss, A. J., Boes, R. M. and Pfister, M. (2020). *Hydraulic engineering of dams*. London, UK: CRC Press.

Haltas, I. and Kavvas, M. (2011). Scale invariance and self-similarity in hydrologic processes in space and time. *Journal of Hydrologic Engineering*, 16(1):51–63.

Harada, S. and Li, S. S. (2018). Modelling hydraulic jump using the bubbly two-phase flow method. *Environmental Fluid Mechanics*, 18(2):335–356.

Hassan, S. H., Guo, T. and Vlachos, P. P. (2019). Flow field evolution and entrainment in a free surface plunging jet. *Physical Review Fluids*, 4(10):104603.

Hattori, M., Arami, A. and Yui, T. (1994). Wave impact pressure on vertical walls under breaking waves of various types. *Coastal Engineering*, 22(1-2):79–114.

Heller, V. (2011). Scale effects in physical hydraulic engineering models. *Journal of Hydraulic Research*, 49(3):293–306.

Heller, V. (2017). Self-similarity and Reynolds number invariance in Froude modelling. *Journal of Hydraulic Research*, 55(3):293–309.

Heller, V., Hager, W. H. and Minor, H.-E. (2008). Scale effects in subaerial landslide generated impulse waves. *Experiments in Fluids*, 44(5):691–703.

Henriksen, R. N. (2015). *Scale invariance: self-similarity of the physical world*. Weinheim, Germany: John Wiley & Sons.

Hohermuth, B., Kramer, M., Felder, S. and Valero, D. (2021). Velocity bias in intrusive gas-liquid flow measurements. *Nature Communications*, 12(1):1–9.

Hubbard, D., Griffin, O. and Peltzer, R. (1987). Foam generation and air entrainment near a free surface. Technical report, Naval research lab Washington DC.

Hughes, S. A. (1993). *Physical models and laboratory techniques in coastal engineering*, volume 7. Singapore: World Scientific.

Issakhov, A., Zhandaulet, Y. and Nogaeva, A. (2018). Numerical simulation of dam break flow for various forms of the obstacle by VOF method. *International Journal of Multiphase Flow*, 109:191–206.

Khan, A. and Hoque, A. (2010). A study on dimensional analysis for air-water flow system. *GANIT: Journal of Bangladesh Mathematical Society*, 30:11–18.

Khattab, I. S., Bandarkar, F., Fakhree, M. A. A. and Jouyban, A. (2012). Density, viscosity, and surface tension of water+ ethanol mixtures from 293 to 323 K. *Korean Journal of Chemical Engineering*, 29(6):812–817.

Kieffer, M., Fuller, M. P. and Jellings, A. J. (1998). Explaining curd and spear geometry in broccoli, cauliflower andromanesco': quantitative variation in activity of primary meristems. *Planta*, 206(1):34–43.

Kiger, K. T. and Duncan, J. H. (2012). Air-entrainment mechanisms in plunging jets and breaking waves. *Annual Review of Fluid Mechanics*, 44:563–596.

Kleefsman, K., Fekken, G., Veldman, A., Iwanowski, B. and Buchner, B. (2005). A volume-of-fluid based simulation method for wave impact problems. *Journal of Computational Physics*, 206(1):363–393.

Kline, S. J. (1965). *Similitude and approximation theory*. London, UK: McGraw-Hill.

Kobus, H. and Koschitzky, H. P. (1991). Local surface aeration at hydraulic structures. In *Air Entrainment in Free-surface Flow*, pages 29–53. Routledge.

Kolmogorov, A. N. (1991). The local structure of turbulence in incompressible viscous fluid for very large Reynolds numbers. *Proceedings of the Royal Society of London. Series A: Mathematical and Physical Sciences*, 434(1890):9–13.

Launder, B. and Spalding, D. (1974). The numerical computation of turbulent flows. *Computer Methods in Applied Mechanics and Engineering*, 3(2):269–289.

Leandro, J., Bung, D. and Carvalho, R. (2014). Measuring void fraction and velocity fields of a stepped spillway for skimming flow using non-intrusive methods. *Experiments in Fluids*, 55(5):1–17.

Lie, S. (1880). Theorie der Transformationsgruppen i. *Mathematische Annalen*, 16(4):441–528.

Lin, P., Xiong, Y., Zuo, C. and Shi, J.-K. (2021). Verification of similarity of scaling laws in tunnel fires with natural ventilation. *Fire Technology*, 57(4):1611–1635.

Liu, X. and Duncan, J. H. (2003). The effects of surfactants on spilling breaking waves. *Nature*, 421(6922):520.

Llewellin, E., Del Bello, E., Taddeucci, J., Scarlato, P. and Lane, S. (2012). The thickness of the falling film of liquid around a Taylor bubble. *Proceedings of the Royal Society A: Mathematical, Physical and Engineering Sciences*, 468(2140):1041–1064.

Lu, G., Duan, Y. and Wang, X.-D. (2014). Surface tension, viscosity, and rheology of water-based nanofluids: a microscopic interpretation on the molecular level. *Journal of Nanoparticle Research*, 16(9):2564.

Lugni, C., Miozzi, M., Brocchini, M. and Faltinsen, O. (2010). Evolution of the air cavity during a depressurized wave impact. i. the kinematic flow field. *Physics of Fluids*, 22(5):056101.

Ma, Z., Causon, D., Qian, L., Mingham, C. and Ferrer, P. M. (2016). Numerical investigation of air enclosed wave impacts in a depressurised tank. *Ocean Engineering*, 123:15–27.

Mandelbrot, B. (1967). How long is the coast of Britain? Statistical self-similarity and fractional dimension. *Science*, 156(3775):636–638.

Mandelbrot, B. B. and Mandelbrot, B. B. (1982). *The fractal geometry of nature*, volume 1. New York City, New York: W.H. Freeman.

McKeogh, E. and Ervine, D. (1981). Air entrainment rate and diffusion pattern of plunging liquid jets. *Chemical Engineering Science*, 36(7):1161–1172.

Mitsuyasu, H. (1967). Shock pressure of breaking wave. *Coastal Engineering Proceedings*, pages 268–283.

Müller, G. (2019). Energy dissipation through entrained air compression in plunging jets. *Journal of Hydraulic Research*.

Nina, Y. A., Shi, R., Wüthrich, D. and Chanson, H. (2022). Intrusive and non-intrusive two-phase air-water measurements on stepped spillways: A physical study. *Experimental Thermal and Fluid Science*, 131:110545.

Novak, P., Guinot, V., Jeffrey, A. and Reeve, D. E. (2010). Hydraulic modelling–an introduction. *Spon Press, London*.

Peregrine, D. and Thais, L. (1996). The effect of entrained air in violent water wave impacts. *Journal of Fluid Mechanics*, 325:377–397.

Pfister, M. and Chanson, H. (2014). Two-phase air-water flows: Scale effects in physical modeling. *Journal of Hydrodynamics, Ser. B*, 26(2):291–298.

Pfister, M. and Hager, W. H. (2010). Chute aerators. i: Air transport characteristics. *Journal of Hydraulic Engineering*, 136(6):352–359.

Polsinelli, J. and Kavvas, M. L. (2016). A comparison of the modern Lie scaling method to classical scaling techniques. *Hydrology and Earth System Sciences*, 20(7):2669–2678.

Polyanin, A. D. and Manzhirov, A. V. (2008). *Handbook of integral equations*. London, UK: Chapman and Hall.

Pope, S. B. (2000). *Turbulent Flows*. Cambridge, UK: Cambridge University Press.

Pringle, C. C., Ambrose, S., Azzopardi, B. J. and Rust, A. C. (2015). The existence and behaviour of large diameter Taylor bubbles. *International Journal of Multiphase Flow*, 72:318–323.

Radiom, M., Yang, C. and Chan, W. K. (2010). Characterization of surface tension and contact angle of nanofluids. In *Fourth International Conference on Experimental Mechanics*, volume 7522, pages 395–403. SPIE.

Richardson, L. F. (1922). *Weather prediction by numerical process*. Cambridge, UK: Cambridge University Press.

Roenby, J., Bredmose, H. and Jasak, H. (2016). A computational method for sharp interface advection. *Royal Society Open Science*, 3(11):160405.

Ruff, J. F. and Frizell, K. H. (1994). Air concentration measurements in highly-turbulent flow on a steeply-sloping chute. In *Hydraulic Engineering*, pages 999–1003. ASCE.

Stagonas, D., Warbrick, D., Müller, G. and Magagna, D. (2011). Surface tension effects on energy dissipation by small scale, experimental breaking waves. *Coastal Engineering*, 58(9):826–836.

Van Wylen, G. J. and Sonntag, R. E. (1985). *Fundamentals of classical thermodynamics*, volume 3. New York City, New York: John Wiley & Son.

Vereide, K., Lia, L. and Nielsen, T. K. (2015). Hydraulic scale modelling and thermodynamics of mass oscillations in closed surge tanks. *Journal of Hydraulic Research*, 53(4):519–524.

Viviano, A., Naty, S. and Foti, E. (2018). Scale effects in physical modelling of a generalized OWC. *Ocean Engineering*, 162:248–258.

Wang, H. and Chanson, H. (2015). Air entrainment and turbulent fluctuations in hydraulic jumps. *Urban Water Journal*, 12(6):502–518.

Wang, H. and Chanson, H. (2016). Self-similarity and scale effects in physical modelling of hydraulic jump roller dynamics, air entrainment and turbulent scales. *Environmental Fluid Mechanics*, 16(6):1087–1110.

Wu, W. (2008). *Computational river dynamics*. London, UK: Taylor & Francis Group.

Xu, M., Liu, H., Zhao, H. and Li, W. (2013). How to decrease the viscosity of suspension with the second fluid and nanoparticles? *Scientific Reports*, 3:3137.

Zhainakov, A. Z. and Kurbanaliev, A. (2013). Verification of the open package OpenFOAM on dam break problems. *Thermophysics and Aeromechanics*, 20(4):451–461.

Zhang, X., Leung, C. and Lee, F. (2009). Centrifuge modelling of caisson breakwater subject to wave-breaking impacts. *Ocean Engineering*, 36(12-13):914–929.

Zhou, L., Liu, D. and Karney, B. (2013). Investigation of hydraulic transients of two entrapped air pockets in a water pipeline. *Journal of Hydraulic Engineering*, 139(9):949–959.

Zhu, D., Wu, S. and Wang, N. (2010). Thermal physics and critical heat flux characteristics of Al_2O_3–H_2O nanofluids. *Heat Transfer Engineering*, 31(14):1213–1219.

Zohuri, B. (2015). *Dimensional analysis and self-similarity methods for engineers and scientists*. Cham, Switzerland: Springer.